

Copyright Undertaking

This thesis is protected by copyright, with all rights reserved.

By reading and using the thesis, the reader understands and agrees to the following terms:

1. The reader will abide by the rules and legal ordinances governing copyright regarding the use of the thesis.
2. The reader will use the thesis for the purpose of research or private study only and not for distribution or further reproduction or any other purpose.
3. The reader agrees to indemnify and hold the University harmless from and against any loss, damage, cost, liability or expenses arising from copyright infringement or unauthorized usage.

If you have reasons to believe that any materials in this thesis are deemed not suitable to be distributed in this form, or a copyright owner having difficulty with the material being included in our database, please contact lbsys@polyu.edu.hk providing details. The Library will look into your claim and consider taking remedial action upon receipt of the written requests.

**SEMICONDUCTING PROPERTIES OF
OXIDE THIN FILMS PREPARED BY
PULSED LASER DEPOSITION**

**SUBMITTED BY
LAM CHING YEE**

***A THESIS SUBMITTED IN PARTIAL FULFILLMENT OF THE
REQUIREMENTS FOR THE DEGREE OF
MASTER OF PHILOSOPHY IN PHYSICS***

AT

**THE DEPARTMENT OF APPLIED PHYSICS
THE HONG KONG POLYTECHNIC UNIVERSITY**

August, 2004



**Pao Yue-kong Library
PolyU · Hong Kong**

CERTIFICATE OF ORIGINALITY

I hereby declare that this thesis is my own work and that, to the best of my knowledge and belief, it reproduces no material previously published or written nor material which has been accepted for the award of any other degree or diploma, except where due acknowledgement has been made in the text.

_____ (Signed)

_____ **LAM CHING YEE** (Name of student)



Abstract

All oxide p-n junctions have been successfully grown by pulsed laser deposition method. Three different p-n junctions, namely $\text{La}_x\text{Sr}_{1-x}\text{MnO}_3/\text{SrTiO}_3/\text{La}_{1-y}\text{Sr}_y\text{TiO}_3$, $\text{La}_{0.7}\text{Sr}_{0.3}\text{MnO}_3/\text{Nb-1wt\% doped SrTiO}_3$ and $\text{Li}_{0.15}\text{Ni}_{0.85}\text{O}/\text{La}_{0.05}\text{Sr}_{0.95}\text{TiO}_3$ have been fabricated. Structural characterization by x-ray diffraction reveals excellent heteroepitaxial relation in all these junctions. The diffusion potential of $\text{La}_{1-x}\text{Sr}_x\text{MnO}_3/\text{SrTiO}_3/\text{La}_{1-y}\text{Sr}_y\text{TiO}_3$, $\text{La}_{0.7}\text{Sr}_{0.3}\text{MnO}_3/\text{Nb-1wt\% doped SrTiO}_3$ and $\text{Li}_{0.15}\text{Ni}_{0.85}\text{O}/\text{La}_{0.05}\text{Sr}_{0.95}\text{TiO}_3$ junctions are 1eV, 0.2eV, and 0.3eV respectively. All of the fabricated p-n junctions yield typical I-V characteristics and display good rectifying property under room temperature.

According to the high thermal stability property of oxides, all-oxide p-n junction could operate at temperature up to 500K. Throughout the research, it is observed that even a highly conducting and metallic-like oxide film could form good p-n junction. However the narrow depletion layer causes a large leakage current under the reverse biased condition. The insertion of insulating layer (SrTiO_3) helps in “broadening” the depletion layer and hence prevents the occurrence of large leakage current. Unfortunately the turn-on voltage increases as well. So a compromise between the reduction of leakage current and the increases of turn-on voltage should be made. It is consideration that ultimately determines the optimum insulating layer thickness. The high temperature operation ($\sim 500\text{K}$) has been confirmed in all junctions. In general, the change in leakage current and turn-on voltage of all-oxide p-n junctions follow the same pattern as those seen in conventional semi-conductor counterparts.



$\text{La}_{0.7}\text{Sr}_{0.3}\text{MnO}_3$ is a well known magnetoresistance material. It exhibits a large positively MR. We have studied influence of the magnetic field on the $\text{La}_{0.7}\text{Sr}_{0.3}\text{MnO}_3/\text{Nb-1wt\% doped SrTiO}_3$ junction transport properties at room temperature. The $\text{La}_{0.7}\text{Sr}_{0.3}\text{MnO}_3$ film, which is grown at 100mTorr, has the phase transition at 290K. It has been shown that the junction works stably upon a 1T magnetic field application. No apparent spin dependent junction transport properties have been observed.

Photo-response has been investigated for the all-transparent oxide $\text{Li}_{0.15}\text{Ni}_{0.85}\text{O}/\text{La}_{0.05}\text{Sr}_{0.95}\text{TiO}_3$ junction as well. This junction potentially can act as a UV photo-detector. The highest photo-response occurs at 340nm. The junction provides a photovoltage of 377mV under 1.28 mW UV illumination.



List of Publications

1. C.Y. Lam and K. H. Wong, Fabrication and characterization of all-perovskite oxide p-n junctions based on $\text{La}_{1-x}\text{Sr}_x\text{MnO}_3$ and Nb-1 wt% doped SrTiO_3 , Journal of European Ceramic Society, in press.



Acknowledgements

I would like to acknowledge Dr. K. H. Wong for his supervision. I specially thank Mr. K. S. So and Dr. W. B. Wu, gives me enlightening suggestions and helps in many experiments. I would also like to thank my research companions. I wish to thank Miss Yoyo Yeung for helping me in some electrical measurement. Special thanks should be given to Mr. C. S. Lo for his assistance in SEM characterization.

This work was partially supported by the Research Grant Council of the Hong Kong Special Administrative Region (PolyU 5294/02P). I am grateful for the award of a research studentship by The Hong Kong Polytechnic University.



Table of Contents

<i>Abstract</i>	<i>I</i>
<i>List of Publications</i>	<i>III</i>
<i>Acknowledgements</i>	<i>IV</i>
<i>Chapter 1</i>	<i>1</i>
<i>Introduction</i>	<i>1</i>
1.1 Introduction	1
1.2 Working principle of all-oxide p-n junction	3
1.2.1 Mechanism of p-n junction	3
1.2.2 Conduction mechanism in oxides	7
1.3 Literature reviews on all-oxide p-n junction	8
1.4 Outline of thesis	10
<i>Chapter 2</i>	<i>12</i>
<i>Pulsed laser deposition</i>	<i>12</i>
2.1 History of pulsed laser deposition	12
2.2 Mechanism of pulsed laser deposition	13
2.2.1 The three stages of pulsed laser deposition process	13
2.2.1.1 Laser-target interaction	13
2.2.1.2 Target to substrate gas phase transportation	14
2.2.1.3 Nucleation and film growth	14
2.3 Advantage and disadvantage of pulsed laser deposition	15
2.3.1 Advantage of pulsed laser deposition	15
2.3.2 Disadvantage of pulsed laser deposition	16
<i>Chapter 3</i>	<i>18</i>
<i>Experiments and set-up</i>	<i>18</i>
3.1 Introduction	18
3.2 Equipment	19
3.2.1 Excimer laser	19
3.2.2 Optics	21
3.2.3 Vacuum system	22
3.3 Testing instrument	24



3.3.1 X-ray diffraction	24
3.3.2 Scanning electron microscope.....	26
3.4 Experimental procedures	27
3.4.1 Target fabrication	27
3.4.2 Substrate preparation.....	27
3.4.3 Deposition process	28
3.5 Structural analysis of thin films	29
3.5.1 Thickness measurement	29
3.5.2 In-plane and out-of-plane structure measurement.....	30
3.5.3 Surface morphology measurement.....	32
3.6 Electrical properties of thin films	32
3.6.1 Resistivity against temperature relation	32
3.6.2 Current-voltage measurement	33
3.6.3 Magnetoresistance (MR) effect.....	34
3.7 Optical properties of thin films	35
3.7.1 Transmission measurement	35
3.7.2 UV Exposure measurement.....	36
Chapter 4.....	37
<i>Fabrication and characterization of $\text{La}_{1-x}\text{Sr}_x\text{MnO}_3/\text{SrTiO}_3/\text{La}_{1-y}\text{Sr}_y\text{TiO}_3$</i>	
<i>junction.....</i>	37
4.1 Introduction	37
4.2 Structural characteristics of $\text{La}_{1-x}\text{Sr}_x\text{MnO}_3$, and $\text{La}_{1-y}\text{Sr}_y\text{TiO}_3$ targets	39
4.2.1 Fabrication of $\text{La}_{1-x}\text{Sr}_x\text{MnO}_3$, and $\text{La}_{1-y}\text{Sr}_y\text{TiO}_3$ targets.....	39
4.2.2 Structural characteristics of $\text{La}_{1-x}\text{Sr}_x\text{MnO}_3$ and $\text{La}_{1-y}\text{Sr}_y\text{TiO}_3$ targets.....	40
4.3 Structural characteristics of $\text{La}_{1-x}\text{Sr}_x\text{MnO}_3$, and $\text{La}_{1-y}\text{Sr}_y\text{TiO}_3$ thin films and	
p-$\text{La}_{1-x}\text{Sr}_x\text{MnO}_3$/i-$\text{SrTiO}_3$/n-$\text{La}_{1-y}\text{Sr}_y\text{TiO}_3$ tri-layer structure	43
4.3.1 Fabrication of LSMO, LSTO and STO thin films.....	43
4.3.2 Structural characterization of $\text{La}_{1-x}\text{Sr}_x\text{MnO}_3$ thin films.....	47
4.3.3 Structural characterization of $\text{La}_{1-y}\text{Sr}_y\text{TiO}_3$ thin films.....	51
4.3.4 Structural characterization of p- $\text{La}_{1-x}\text{Sr}_x\text{MnO}_3$ /i- SrTiO_3 n- $\text{La}_{1-y}\text{Sr}_y\text{TiO}_3$ tri-layer structure.	54
4.4 Electrical properties of the p-$\text{La}_{1-x}\text{Sr}_x\text{MnO}_3$/i-$\text{SrTiO}_3$ n-$\text{La}_{1-y}\text{Sr}_y\text{TiO}_3$ tri-layer junctions	63
4.4.1 Electrical properties of $\text{La}_{1-x}\text{Sr}_x\text{MnO}_3$ thin films.....	63
4.4.2 Electrical properties of $\text{La}_{1-y}\text{Sr}_y\text{TiO}_3$ thin films.....	66



4.4.3 I-V characteristics of p-La _{1-x} Sr _x MnO ₃ /i-SrTiO ₃ / n-La _{1-y} Sr _y TiO ₃ junctions at room temperature	68
4.4.4 The influence of temperature on the properties of the La _{1-x} Sr _x MnO ₃ /SrTiO ₃ /La _{1-y} Sr _y TiO ₃ junction	80
Chapter 5	90
<i>Fabrication and characterization of La_{0.7}Sr_{0.3}MnO₃/Nb-1wt% doped SrTiO₃..</i>	90
5.1 Introduction	90
5.2 Structural characterization of La_{0.7}Sr_{0.3}MnO₃/NSTO junction	91
5.2.1 Fabrication of La _{0.7} Sr _{0.3} MnO ₃ /NSTO junction.....	91
5.2.2 Structural characterization of La _{0.7} Sr _{0.3} MnO ₃ /NSTO junction	93
5.3 Electrical characterization of La_{0.7}Sr_{0.3}MnO₃/NSTO junction	96
5.3.1 The influence of deposition pressure on La _{0.7} Sr _{0.3} MnO ₃ film	96
5.3.2 I-V characteristics La _{0.7} Sr _{0.3} MnO ₃ /NSTO junction	98
5.3.3 The influence of magnetic field on the manganite based La _{0.7} Sr _{0.3} MnO ₃ /NSTO junction	107
Chapter 6	110
<i>Fabrication and characterization of Li_{0.15}Ni_{0.85}O/ La_{0.05}Sr_{0.95}TiO₃ junction ..</i>	110
6.1 Introduction	110
6.2 Fabrication and characterization of the fabricated target and thin films ____	113
6.2.1 Fabrication and structural analysis of LNO target	113
6.2.2 Surface morphology of the single layer LNO film.....	115
6.2.3 Fabrication and structural analysis of LNO/LSTO junction	118
6.2.4 Structural characterization of LNO/LSTO junction	120
6.3 Electrical characterization of the single layer films and junction	124
6.3.1 R-T relation of single layer LNO and LSTO films	124
6.3.2 I-V characterization of the LNO/LSTO junction	126
6.3.2.1 I-V relations between the electrode layer and the oxide films	126
6.3.2.2 Comparison between LNO/LSTO/LAO and LSTO/LNO/LAO junctions.....	127
6.3.2.3 The temperature dependence of LNO/LSTO/LAO and LSTO/LNO/LAO junctions	129
6.3.2.4 SrTiO ₃ thickness dependence of LNO/STO/LSTO/LAO junction	136
6.4 Optical characterization of LNO/LSTO junction	138
6.4.1 Transmission spectral of LSTO, LNO and the bi-layer LNO/LSTO junction	138
6.4.2 Photocurrent in single layer LSTO film.....	140



6.4.3 UV photo-response on LSTO/LNO/LAO junction	143
6.4.3.1 Variation of I-V characteristics under the UV light illumination	143
6.4.3.2 Real time response of the junction under pulsed laser illumination.....	144
6.4.3.3 Spectral dependence on the photovoltage generation	147
6.4.4 UV response of the LNO/LSTO/LAO junction	148
6.4.4.1 Spectral dependence of the photovoltage generation	148
Chapter 7.....	153
Conclusion and future work	153
References	158



Chapter 1

Introduction

1.1 Introduction

With the increase in demand on electronics devices for diversified applications, researchers are progressively appreciated and looking into the feasibilities of utilizing materials of multitudinous functionalities. Oxides have many excellent properties such as ferroelectricity, high permittivity, superconductivity, magnetism and photoelectricity. Many oxides are known for their excellent insulating properties with very small leakage current [Ohmi et. al. 2004, Youm et. al. 2003, Lu et. al. 2003]. Indeed some of them have been extensively used as gate dielectrics in CMOS technology by today's microelectronic industry. However, with proper doping or variation in their composition contents, many oxides can become semiconductors or even good conductors [Schmehl et. al. 2003, Windisch et. al. 2001, Wu et. al. 2000, 2001]. Such oxide semiconductors can possess either p-type or n-type conduction [Suzuki et. al. 2003, Hiramatsu et. al. 2003]. By putting a p-type and a n-type oxide semiconductors of similar structure together, a current rectifying p-n junction diode is expected. This is a close analogue to those of conventional semiconductors. However, the rich choice of oxides and their dopants provides a wealth of potentially useful electrical properties. The relatively large bandgap of these oxide semiconductors allows a stable and high temperature diode operation, or formation of a UV detector. Therefore an all-oxide p-n junction diode will be



of great interest to microelectronic industry.

The use of conventional semiconducting materials always encounters the limitation imposed by the maximum operation temperature. The normal maximum operation temperature for commercial p-n diode is only 350K. High temperature operation ($>400\text{K}$) of the electronic devices is difficult to achieve. Thermal budget also leads to the package problems. With the rapid progress in modern technology, complex and condensed packaging is one of the ultimate goals for the electronic devices. Low temperature operation is incompatible to condensed packaging, for a heat sink requires large radiating/conducting area. Application of oxide semiconductor is one of the potential solutions for the thermal issues. It is well known that oxides possess good thermal stability at high temperature. This distinct property of oxides thus gives rise to high temperature operation possibilities in the electronic world.

The basic component of electronic device is a p-n junction. As such, all-oxide p-n junctions have been fabricated. All junction properties have been examined at various operation temperatures, so that the concept of high temperature operation of all-oxide p-n junction could be verified. In this study, all the p-n junctions were fabricated by pulsed laser deposition technique. Lattice matched single crystal substrates and optimized film growth conditions were used to warrant high structural quality. Film thickness was kept at 400-500nm. Junction area was normally arranged to within 0.25mm^2 to avoid pinholes and particulates in the films.



1.2 Working principle of all-oxide p-n junction

1.2.1 Mechanism of p-n junction

The working principle of an all-oxide p-n junction is similar to that of a conventional semiconductor junction. Band model is utilized to explain the electrical behavior of a p-n junction here [Sze 1981, 1985, Sparkes 1994]. The band structures of p-type semiconductor and n-type semiconductor are shown in Fig. 1.1. The two materials possess different Fermi levels. When the two materials are brought together, electrons immediately diffuse from the n-region, where their concentration is relatively high, into the p-region; similarly holes tend to diffuse from the p-region into the n-region. The process continues until the Fermi levels line up. Therefore the diffusion electrons and holes recombine in the transition region. As a result, the n-region acquires a net positive charge and the p-region acquires a net negative charge in the transition region, and hence a potential gradient is created. This transition region is a space-charged region, far fewer mobile carriers exist in this region.

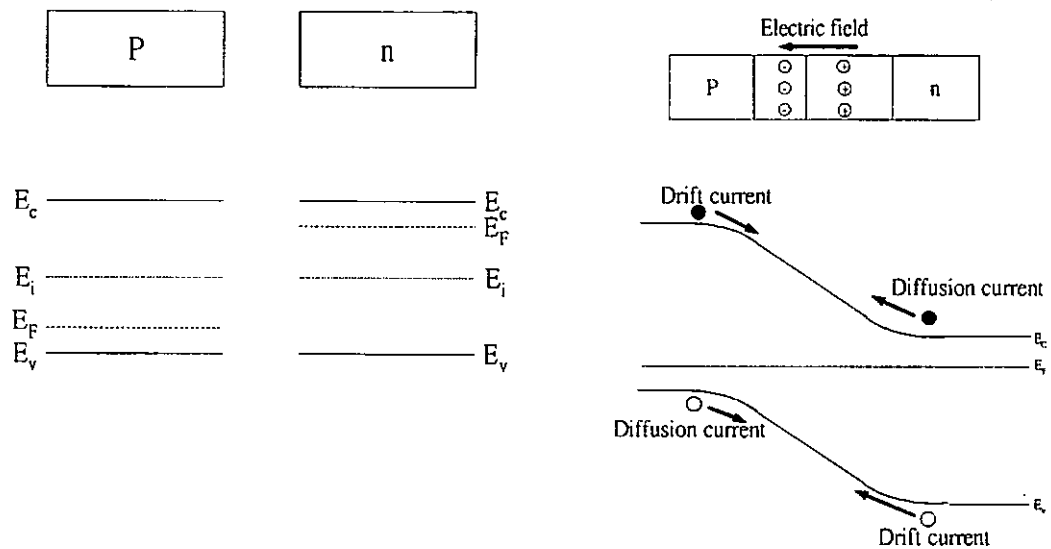


Fig. 1.1 Band structures of p-type semiconductor and n-type semiconductor

Two currents flow through the junction under the equilibrium condition could be obtained. The drift current is one. Few minority carriers in each region are drawn through the transition region by the electric field within it and this current is flowing from the n-region to the p-region and labels as I_0 . Another, named diffusion current is the flowing of majority carriers in opposite of I_0 . This current consists of electrons in the conduction band, or holes in the valence band, which have acquired sufficient energy from random thermal vibrations to surmount the potential hill formed in the junction and indicated by the slopes of the energy bands. These two currents totally compensate each other under the equilibrium condition.

With a forward biased voltage, the barrier height is reduced by the amount of the forward bias. The majority carriers diffused through the transition region



increases exponentially with the applied voltage. However the minority carrier current is still flowing in the opposite direction and hence the overall current

is $I = I_0 \left[\exp\left(\frac{qV_D}{kT}\right) - 1 \right]$. Therefore, under a reverse biased condition, the

potential barrier is enlarged. The proportion of diffusion current is largely reduced and can be neglected, thus the total current is the same as $-I_0$. And this

is called the saturation current. The schematic diagrams of the band structure under equilibrium, forward biased and reverse biased are illustrated in Fig. 1.2

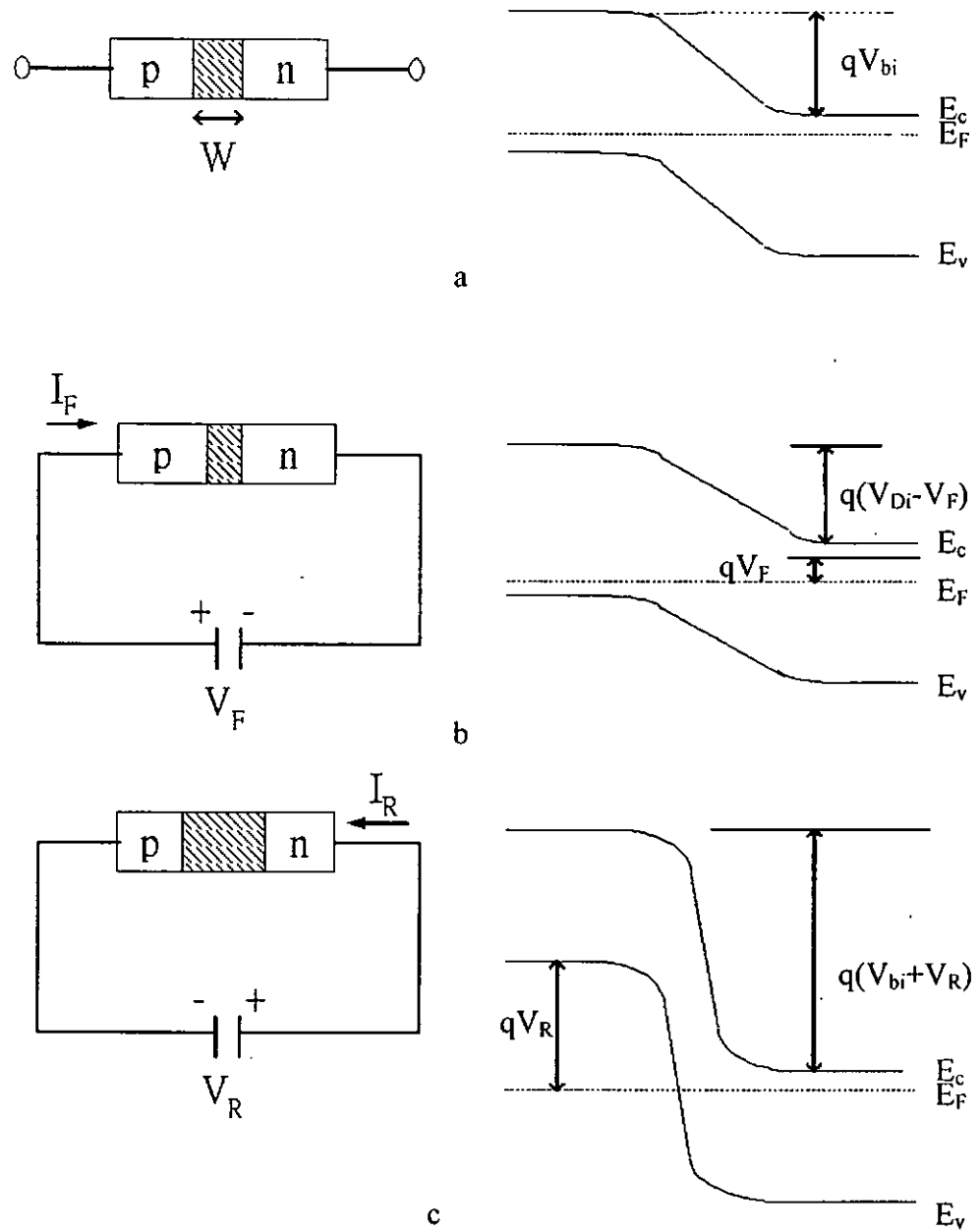


Fig. 1.2 Band diagrams of the p-n junction at (a) equilibrium, (b) forward biased, and (c) reverse biased



1.2.2 Conduction mechanism in oxides

In contrast to charge transportation mechanism in conventional semiconductor or metal, conduction in oxides is not only induced by electronic carrier (electron and hole) but often achieved by ionic carrier as well. Although the mobility of ion is always several orders of magnitude lower than that of electron, ionic conduction nevertheless helps to create the n- or p-type conduction in oxides. The n-type conduction oxides are obtained by slight reduction, substitutional doping of higher oxidation state element to replace the lower oxidation state component in the oxide and insertion of electronegative element etc. In all cases negative carrier are introduced into the oxides. Similarly, p-type conduction oxides are achieved by electron removal via oxidation or introduction of positive carriers via doping of lower oxidation state element to replace the higher oxidation state component in the oxide. The mixed-valency has, in fact, rendered some complex transitional metal oxides to possess both n- and p-type conducting properties according to their composition ratio. For example, $\text{Co}_{3-x}\text{Fe}_x\text{O}_3$ is one of the well known transition metal oxide. With $x \geq 2$ it is a n-type conductor and when $x < 2$ it has p-type conduction [Cox 1992].



1.3 Literature reviews on all-oxide p-n junction

The first all-oxide p-i-n heterojunction was fabricated in 1999 [Sugiura et. al. 1999]. Sugiura and his co-worker have succeeded in fabricating p-i-n diodes with good rectifying properties by growing p- $\text{La}_{0.85}\text{Sr}_{0.15}\text{MnO}_3$ /i- SrTiO_3 /n- $\text{La}_{0.05}\text{Sr}_{0.95}\text{TiO}_3$ heterostructure on (100) SrTiO_3 substrate using the ArF excimer laser ablation and an eclipse method. They observed a relatively low breakdown voltage occurring in samples without the i-layer. It is because of $\text{La}_{0.85}\text{Sr}_{0.15}\text{MnO}_3$ and $\text{La}_{0.05}\text{Sr}_{0.95}\text{TiO}_3$ are degenerated semiconductors. The transition region of the p-n junction is very narrow incurring large tunneling current. They also showed the pronounced effect of space-charge-limited-current property that may arise from the residual traps inside the i- SrTiO_3 layer, leading to the current degradation under low operation temperature [Sugiura et. al. 2001]. Thereafter Nakasaka and co-worker have also successfully fabricated a p-i-n junction with the combination of $\text{La}_{0.95}\text{Sr}_{0.05}\text{MnO}_3$ / BaTiO_3 / $\text{La}_{0.01}\text{Sr}_{0.99}\text{TiO}_3$ [Nakasaka et. al. 2001].

In 2002, all-perovskite oxide p-n junction consisting of $\text{La}_{0.9}\text{Ba}_{0.1}\text{MnO}_3$ (LBMO) and $\text{Sr}_{0.99}\text{La}_{0.01}\text{TiO}_3$ (SLTO) was fabricated [Zhang et. al. 2002]. The bi-layer junction maintained a good rectifying behavior at both room temperature and low temperature without inserting an insulating layer. In 2003, good rectifying behavior bi-layer junction was fabricated with the use of $\text{La}_{0.7}\text{Sr}_{0.3}\text{MnO}_3$, in which ZnO was selected as the n-layer [Tiwari et. al. 2003]. Later on, a nearly temperature independent rectifying characteristic was revealed in a p-n junction consisting of oxygen deficient $\text{La}_{0.67}\text{Ca}_{0.33}\text{MnO}_{3-\phi}$ and Nb-doped



SrTiO_3 [Hu et. al. 2003]. This junction showed good rectifying characteristic in a wide temperature range from 5 to 350K.

In later research, some distinct properties that affect the junction performance have been determined. The colossal magnetoresistance (MR) effect on the junction performance was investigated by Tanaka [Tanaka et. al. 2002] and Sun [Sun et. al. 2004]. Tanaka and co-worker produced their junction based on Ba-doped manganites and the commercial Nb-doped SrTiO_3 . They showed a metal-insulator transition in manganite and the associated temperature dependence of the junction resistance. However no observation of magnetically modulating effect on the junction characteristic has been identified. It was attributed to the low MR of the $\text{La}_{0.67}\text{Ca}_{0.33}\text{MnO}_{3-\delta}$ (LBMO) film. The work on manganite-based junction was continued by Sun et. al.. A $\text{La}_{0.29}\text{Pr}_{0.38}\text{Ca}_{0.33}\text{MnO}_3$ (LPCM) / SrTiO_3 -Nb junction was fabricated in 2004. They showed that the band gap of LPCM ($e_g \uparrow - e_g \downarrow$) varied with the magnetic state. The spin deviation of Mn^{4+} ions from fully ferromagnetic alignment cause a reduction of energy gap between e_g and hence the diffusion potential. Indeed the distinct properties of the oxide layer added to the junction performance can lead to devices of multitudinous functions. So the successful growth all-oxide p-n junction may offer superior performance over that from conventional semiconductor p-n junctions.

In the most recent research, the photovoltaic effects on an all-oxide junction were studied [Sun et. al., 2004]. They investigated the oxygen dependence of photovoltage of the $\text{La}_{0.7}\text{Ce}_{0.3}\text{MnO}_{3-\delta}$ (LCE)/ SrTiO_3 -Nb (STON) junction. A



maximum photovoltage of 54.1mV under the illumination of 460nm wavelength was obtained. They also claimed that the oxygen release from the LCE film would depress the photovoltage effect. It is attributed to the presence of oxygen vacancies. The work of all-oxide p-n junction is still at its infancy. Several p-n junctions or p-i-n junctions will be investigated in this study.

1.4 Outline of thesis

Background theory and literature review on all-oxide p-n junction are described in the last few sections in this chapter. A brief introduction of pulsed laser deposition method is presented in Chapter 2. The working mechanism of the pulsed laser deposition as well as the advantages and disadvantages of utilizing pulsed laser deposition to prepare complex oxide thin films are discussed.

Chapter 3 provides the experimental setup of the pulsed laser deposition system. Each of the equipment used in the system are sequentially introduced. Chapter 3 also introduces the various measurement techniques such as XRD, SEM, and I-V characteristic measurement. The whole deposition process is discussed in detail and epitaxial film grown conditions are emphasized.

In Chapter 4, we focus on the fabrication and characterization of the “p-LSMO/i-STO/n-LSTO” p-i-n junction. Several samples have been fabricated using different chemical composition of LSMO and LSTO targets. The composition and temperature dependences of these junctions have been examined, and results of which are presented.



Magnetoresistive manganite used in fabricating the p-n junction is described in Chapter 5. LSMO exhibits prominent magnetoresistance effect. It is p-type conducting and forms a p-n junction with NSTO. The characteristics and performance of such junction have been investigated, and the results of which are furnished in chapters.

Fabrication of UV detector is one of the objectives of studying all-oxide p-n junction. So in this research we try to produce an all-transparent oxide p-n junction which could withstands the high temperature operation. $\text{La}_{0.05}\text{Sr}_{0.95}\text{TiO}_3$ and $\text{Li}_{0.15}\text{Ni}_{0.85}\text{O}$ are n-type and p-type conductors respectively. Both are wide band gap materials with the ability to detect wavelength in the UV region. In Chapter 6, the fabrication of the p-n junction of $\text{Li}_{0.15}\text{Ni}_{0.85}\text{O}/\text{La}_{0.05}\text{Sr}_{0.95}\text{TiO}_3$ is illustrated. Apart from the normal current rectifying I-V characteristic, the photovoltaic effect of these junctions is scrutinized.

The present experimental results and important findings are emphasized and concluded in the last chapter of this thesis. Suggestion for future investigation and development are suggested. The values of this research are objectively and fairly evaluated.



Chapter 2

Pulsed laser deposition

2.1 History of pulsed laser deposition

In the mid of 1960s, the first breakthrough of pulsed laser deposition (PLD) occurred. The reliable electronic Q-switch laser was developed; a very short optical pulse with peak power density exceeding 10^8W/cm^2 could be generated. Therefore, the use of short laser pulse for photo-ablation is more likely to achieve congruent evaporation. This allows the PLD process to preserve stoichiometry during mass transfer from the target to the thin film. With the continuously progress of laser technology, high efficiency second harmonic generator was developed, delivering shorter wavelength radiation. Accordingly, the absorption depth is shallow and the splashing of molten materials from the target is reduced. During this period, several publications had been announced for the successful film growing by PLD [Tang et. al. 1976]. With the affordability and improved quality of commercial lasers, many research groups joined the PLD field in 1980s. For the first time, epitaxial semiconductor films, heterostructures, and superlattices grown by PLD showed qualities comparable to those grown by MBE [Cheung et. al. 1983].



2.2 Mechanism of pulsed laser deposition

Pulsed laser deposition method is the use of a high power laser as an external energy source to vaporize materials and to deposit thin films. In simply rastering the laser spot over the target surface, the laser radiation will be converted from electromagnetic energy to electronic excitation and then to thermal, chemical, and even mechanical energy to cause evaporation, ablation, excitation, plasma formation, and exfoliation. Evaporants form a “plume” consisting of a mixture of energetic species including atoms, molecules, electrons, ions, clusters, micro-sized solid particulates, and molten globules. The “plume” is highly directional and rapidly expands into the vacuum from the target surface to form a nozzle jet with hydrodynamic flow characteristics. Then the energetic species undergo thermal and non-thermal interaction with the substrate and ultimately lead to film formation and grain growth [Chrissey et. al. 1994].

2.2.1 The three stages of pulsed laser deposition process

2.2.1.1 Laser-target interaction

The bombardment of laser pulses with condensed phases would lead to sputtering action on the condensed material. This sputtering would lead to particle emission with different mechanistic possibilities, namely, thermal, electronic, exfoliational and hydrodynamic etc. Thermal sputtering is the vaporization from a transiently heated target. Electronic sputtering is not a



unique process, but rather a group of processes having the common feature involving some form of excitation or ionization such as production of electron-hole pair and/or exciton, lattice localized relaxation, transition to an anti-bonding potential energy on surface and desorption from surface. Exfoliation is the flakes detachment from a target owing to repeated thermal shocks. And finally hydrodynamic refers to processes in which droplets of material are formed and expelled from a target as a consequence of the transient melting. [Chrisey et. al. 1994].

2.2.1.2 Target to substrate gas phase transportation

The plasma plume behaves like a forward jet of uniform translational energy with small spread. The thermal induced particle will spread out as $\cos\theta$ while the non-thermal induced particle will follow a sharp and narrow profile $\cos^n\theta$, where $n \gg 1$. The plasma also carries high ion/neutral ratio and many multiply ionized species. It is also noted for its high average translational energy of about 10-100eV.

2.2.1.3 Nucleation and film growth

Three conventional modes for film nucleation and growth apply in PLD technique. It is convenient to separate the discussion into the three conventional modes of films nucleation and growth: (i) three-dimensional island growth (Volmer-Weber), (ii) two-dimensional full-mono-layer growth (Frank-van der Merwe), and (iii) two-dimensional growth of full monolayers followed by



nucleation and growth of three-dimensional islands (Stransk-Kastinov). The selection of one of these growth modes by a substrate-film system depends (a) on the thermodynamics relating the surface energies, and (b) the film-substrate interface energy [Chrissey et. al. 1994].

2.3 Advantage and disadvantage of pulsed laser deposition

2.3.1 Advantage of pulsed laser deposition

With the use of PLD, the fabricated film normally retains the same stoichiometry as the multicomponent target. Since the focused laser beam has a very high energy density which can evaporate all the components simultaneously, irrespective of their difference in melting point. Besides, the as-deposited energetic species can have high enough kinetic energy to migrate to their favorable site. In deed, PLD of crystalline films requires a substrate temperature that is relatively low in comparison with other deposition method such as thermal evaporation, electron-beam or ion-beam evaporation, d.c. or r.f. magnetron sputtering, chemical vapor deposition (CVD), and molecular beam epitaxy (MBE). In addition, the PLD method allows the in-situ growth of different materials. For example, using a rotating multi-target holder, the laser beam can be rastered different targets by setting a suitable alignment. In this way in-situ growth of heterostructures is enabled. Furthermore, the thin film made by PLD can be deposited in any ambient gas. Finally, PLD also have the low start-up cost when comparing with, say, molecular beam epitaxy (MBE).



2.3.2 Disadvantage of pulsed laser deposition

There are three main disadvantages of using PLD. Due to the limited angular spread of the plume, the deposition area is very small. At a typical PLD geometry a deposited film of no more than 1 cm^2 can be obtained. The thickness of the film is the highest at the center of the plasma plume and decreases rapidly with the distance away from the center point [Chrisey et. al. 1994]. So for large area film the uniformity is not good. The uniformity can be improved somewhat by tilting and rotating the substrate. The second disadvantage is the target surface modification. Laser irradiation of the compound material target modifies the surface layer's chemical composition. Pitting of the surface due to laser beam "hot spot" and differential absorption of the target materials may also occur. The net effect of these changes is that, at some point during film deposition, the irradiated target surface bears very little resemblance to that which was load locked into the vacuum chamber before film deposition began. The third one is the generation of particulates. The formation mechanism of particulates is multifarious [Chrisey et. al. 1994]. The size of particulates can be as large as $\sim \mu\text{m}$, which is bigger than the thickness dimension of the deposited film. Therefore the presence of large particulates in/on the film is sufficient to degrade the usefulness of the film. This problem is more severe in multi-layer systems. The number of the particulates, however, can be greatly reduced by placing a blocking mask in between the substrate and the target holder, and it is called "eclipse" method [Kinoshita et. al. 1993]. There are also different kinds of mechanical approaches, though less frequently used, to reduce the number of particulates, such as velocity filter,



electromagnetic shutter etc.



Chapter 3

Experiments and set-up

3.1 Introduction

All the heterostructural p-n junctions were growth by PLD. The basic equipment used in PLD consists of three main units: a laser system, optics elements and a vacuum deposition chamber. The deposition was carried out either in vacuum or under ambient oxygen of 100 – 200 mTorr pressure. The substrate was normally maintained by an ohmic heater at 500°C-650°C. After the film had been fabricated, the surface morphology of the films was investigated by the Scanning Electron Microscope (SEM). From the picture of SEM, we can determine the surface morphology as well as the relative importance of problems associated with particulates. Moreover, the cross section image of the multi-layer films and the interface quality were studied by SEM. From these the thickness of the multi-layer films could also be revealed. The structural characteristics of the thin film were investigated by X-ray Diffraction (XRD). The epitaxial relation of the thin film was evaluated by the four-circle XRD analysis too.

The electrical properties of single layer or multi-layer films were investigated. The change in resistivity as a function of temperature was studied. It was measured by a simply two point probe setup. The rectifying properties of these p-n junctions and p-i-n junctions were determined from the current-voltage characteristic curves. Magnetoresistance occurred in one of the grown film materials. Therefore we also analyzed the effect of magnetic field on the



performance of the junction.

It is worthy and useful to find out the band gap energy of the semiconducting oxide film. Towards this goal, transmission spectra of the films were examined. The spectral and temporal photo-responses of the junction were also measured.

3.2 Equipment

3.2.1 Excimer laser

The laser wavelengths used in our PLD system lies in the UV range. At this spectral region, the oxide materials exhibit strong absorption and the interaction between the target and the laser beam is primarily of non-thermal nature. Ablated target materials are ejected from the surface without melting. Our PLD system used a commercial available excimer laser. Excimer laser is a gas discharge laser system. It emits pulsed coherent radiation directly in the UV region and delivers high output in excess of 1 J/pulse. In this research, a KrF excimer laser ($\lambda = 248\text{nm}$) was used. Excimer is a diatomic molecule in an electronically excited state. The upper state of the excimer is formed by a chemical reaction, from its constituents after one of them or both have been electrically excited or ionized in a fast high voltage discharge. The excimer can undergo laser transitions from its upper state to its repulsive or rapidly discharging ground state. Due to the high ratio of upper state lifetime to lower state lifetime, population inversion and high gain can be achieved very easily in excimer laser. A Lambda Physik COMPeX 200 excimer laser was used through out our experiments. The



output spatial profile of this particular laser was a “top hat” with a rectangular dimension of $1 \times 3 \text{ cm}^3$. The maximum laser energy per pulse and maximum repetition rate were $\sim 500 \text{ mJ}$ and 20 Hz respectively.



3.2.2 Optics

The optical elements that couple the laser to the target include lenses and apertures, mirrors, and laser window. Laser-quality optical “UV-grade fused silica” lenses and window were used in the deposition system. UV-grade fused silica has a transmittance of over 90% for the wavelength range from 185 nm to 2000 nm. Commonly, laser fluence of several J/cm^2 is required to achieve target ablation. Lens is used for collecting the radiation from the excimer laser source. The focal length of the lens is 30 cm to match the size of the chamber so that the focused laser spot converges on the target surface.

Laser window is a port which allows the focused laser beam to pass into the chamber, as well as to retain the isolated condition of the chamber. Window of 3 mm thick and 381 mm diameter was used in the deposition system.

Flexibility is one of the advantages of PLD technique. Laser source is decoupled from the deposition chamber, so that a single laser could serve a number of deposition chambers. Beam steering mirrors are used to direct the laser to appropriate chamber. Multi-layered dielectric narrow band high reflection mirrors provide a reflectivity of higher than 95% for the laser beam at 248nm. These dielectric mirrors are essential for minimizing the laser propagation loss.

3.2.3 Vacuum system

The PLD vacuum system comprises of the following elements: chamber, target manipulator, substrate holder and heater, vacuum pump, gas flow, and vacuum gauging. The schematic diagram of the PLD system is shown on Fig. 3.1. In addition to the standard ports required on all vacuum chambers (e.g., pumping port, gas inlet, pressure gauging, and viewports), the PLD chamber must have ports for the targets, substrates, and laser beam.

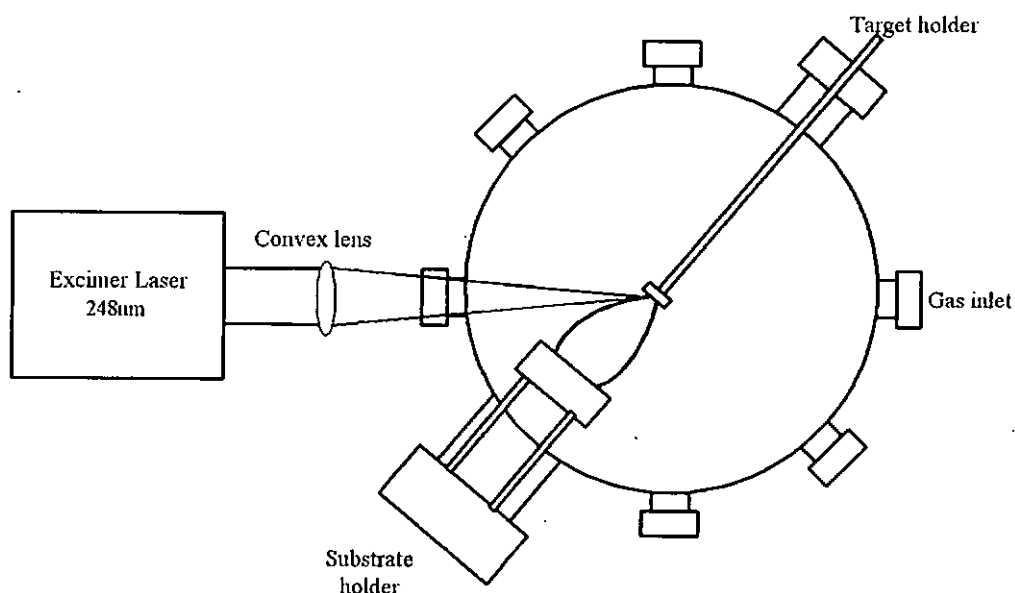


Fig. 3.1 The schematic diagram of the PLD deposition system



In this research, films were made in a chamber connected to a rotary pump and a diffusion pump. Since oxide thin films were fabricated, extra oxygen was required for providing a sufficient oxygen environment. So a gas inlet port was used for afflux of oxygen gas of 99.7% purity. The chamber was first pumped down to a base pressure of 10^{-3} Torr and then back fill with pure oxygen to the desired film growth pressure (~ 100 mTorr). So only the rotary pump was needed to create the desired oxygen ambient (~ 1 mTorr). In some cases where higher vacuum deposition condition is needed, the diffusion pump will be operated continuously to maintain a chamber pressure of 10^{-6} Torr.

In the system, Kanthal wire was used as the heating filament with a total resistance of 11Ω . A high temperature of 650°C could be achieved. And hence the film could be fabricated under a relatively higher temperature, promoting a better crystallinity.

3.3 Testing instrument

3.3.1 X-ray diffraction

The crystallinity of thin film was investigated by an x-ray diffractometer (Philip mode X'pert system) operated in four-circle mode. Since x-rays have high energies and short wavelength, when it is impinged on a solid material, a portion of the beam would be scattered in all directions by the atoms. If the crystalline solid consists a regular array of atoms, it may form a natural three-dimensional “diffraction grating” for x-rays. So, the atomic arrangements in the crystal could be deduced by x-ray diffraction.

When a parallel monochromatic beam of x-rays is incident on the testing film, some of the rays will be reflected from the crystal planes but some will be absorbed or scattered. If this collimated beam of x-rays is allowed to fall on a crystal, the atoms in the crystal become diffraction centers and constructive interference in certain direction will be formed.

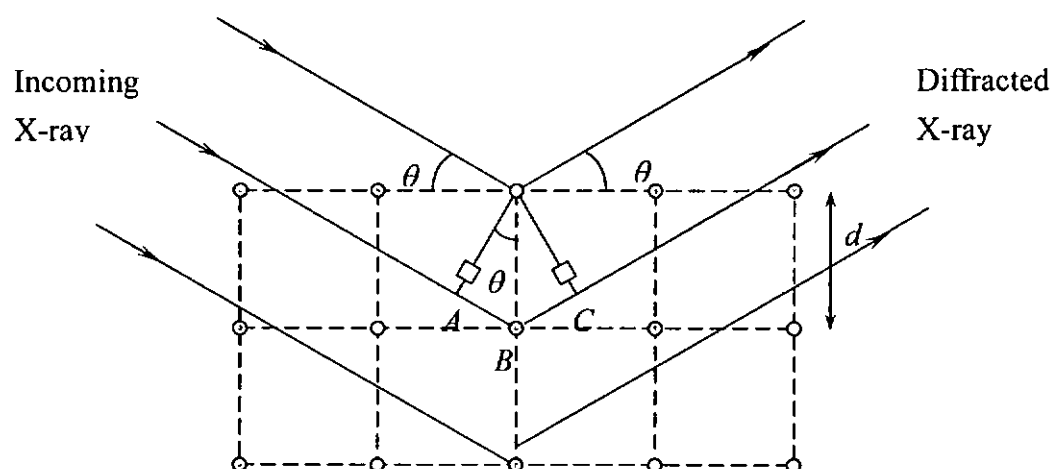


Fig. 3.2 Constructive interference of a lattice structure



Indeed, strong constructive interference is formed if the diffraction satisfies the Bragg's Law:

$$n\lambda = 2d_{hkl}\sin\theta.$$

This equation gives us a simple relation between x-rays wavelength (λ), inter-atomic spacing (d_{hkl}) and angle of the diffracted beam (θ). The d_{hkl} value in cubic structure is $d_{hkl} = \frac{a_0}{(h^2 + k^2 + l^2)^{1/2}}$, where h, k, and l are the Miller index and a_0 is the lattice constant. Table 3.1 lists the d_{hkl} values in different crystal structure

Table 3.1 Equation of interplanar spacing at different structure material

System	Interplanar Spacing
Cubic	$d_{hkl} = \frac{a_0}{(h^2 + k^2 + l^2)^{1/2}}$
Tetragonal	$\frac{1}{d_{hkl}^2} = \frac{h^2 + k^2}{a^2} + \frac{l^2}{c^2}$
Hexagonal	$\frac{1}{d_{hkl}^2} = \frac{4}{3} \left(\frac{h^2 + hk + k^2}{a^2} \right) + \frac{l^2}{c^2}$
Rhombohedral	$\frac{1}{d_{hkl}^2} = \frac{(h^2 + k^2 + l^2)\sin^2 \alpha + 2(hk + kl + hl)(\cos^2 \alpha - \cos \alpha)}{a^2(1 - 3\cos^2 \alpha + 2\cos^3 \alpha)}$
Orthorhombic	$\frac{1}{d_{hkl}^2} = \frac{h^2}{a^2} + \frac{k^2}{b^2} + \frac{l^2}{c^2}$
Monoclinic	$\frac{1}{d_{hkl}^2} = \frac{1}{\sin^2 \beta} \left(\frac{h^2}{a^2} + \frac{k^2 \sin^2 \beta}{b^2} + \frac{l^2}{c^2} - \frac{2hl \cos \beta}{ac} \right)$
Triclinic	$\frac{1}{d_{hkl}^2} = \frac{a^2 b^2 c^2}{V^2} \left[\frac{h^2 \sin^2 \alpha}{a^2} + \frac{k^2 \sin^2 \beta}{b^2} + \frac{l^2 \sin^2 \gamma}{c^2} + \frac{2hk}{ab} (\cos \alpha \cos \beta - \cos \gamma) + \frac{2kl}{bc} (\cos \beta \cos \gamma - \cos \alpha) + \frac{2lh}{ac} (\cos \gamma \cos \alpha - \cos \beta) \right]$



3.3.2 Scanning electron microscope

Scanning electron microscope (SEM) is used to image the specimen's surface and cross section profile. From the micrographs we can examine the microstructures and morphology in details. SEM is a kind of test that a narrow beam of electrons is focused on and scanned across the specimen surface. While scanning the specimen, the electron beam interacts with the specimen. The interaction between the electron beam and the specimen can be divided into two classes: (1) elastic events which affect the trajectories of the beam of electrons within the specimen and (2) inelastic events which result in a transfer of energy from the electron beam to the solid specimen. In the processes of both elastic events and inelastic events, various detectable signals such as secondary electrons, backscattered electrons, characteristics and continuum x-ray etc would be generated. And as there is change in composition, texture or topography at the specimen surface, the collected signal changes too. So the SEM image formed in the display reflects surface features in their correct relative positions. It is just like an optical picture of the specimen surface. The scanned size of the surface of the specimen is much smaller than the size of the screen of the display. Thus the picture shown is a magnified image of the surface of the specimen.



3.4 Experimental procedures

3.4.1 Target fabrication

All the pulsed laser ablation targets were fabricated by the standard solid state reaction method. The required proportions of the constituent oxides were weighed according to the desired stoichiometry. They were then mixed and ground by ball milling for 10 hours. Afterwards calcinations were carried out in order to get rid of the organic component from the mixed powder as well as to initiate the chemical reaction between the oxides. The calcined powder was re-ground again in mortar. Then the powder was compressed by an oil-compressor at a pressure of 3.5 Ton into circular pellets of 2.5 cm in diameter. Sintering was carried out to obtain the desired ceramic target. Both the calcinations and sintering were done at the desired temperature and lasted for 10 hours. The targets shrunk slightly after the thermal treatment. Finally the structural properties and the chemical composition of these ceramic targets were evaluated by XRD and Energy Dispersive X-ray (EDX), respectively.

3.4.2 Substrate preparation

In this study, all thin films were grown on single crystal oxide substrates such as LaAlO_3 (LAO), MgO , and Nb-SrTiO_3 (NSTO). All substrates were purchased from commercial vendors, with sizes of 0.5mm (T) x 5mm (W) x 10mm (L) and 0.5mm (T) x 10mm (W) x 10mm (L). Due to the contamination on the surface, which will greatly affect the quality of the as-prepared film, the



substrate must be thoroughly cleaned before it can be used. We cleansed and degreased the substrates ultrasonically for 10 minutes using spectroscopic grade acetone.

3.4.3 Deposition process

Proper alignment of the target, substrate and optics should be done before the deposition. The target was mounted on the rotating target holder as shown in Fig. 3.1. The target-substrate distance was 4 cm apart. For special fabrication process, such as making a particulate free film, a shadow mask was placed in between the target and substrate. At first, we manipulated the mirrors and lens so that the laser beam passed unobstructed into the chamber through the window and focused onto the target surface. The chamber was then evacuated and back filled with oxygen to the desired pressure, for example 100mTorr. Finally the shape and direction of the energetic plasma plume were checked. The plume should emanate from the target at a direction normal to the target surface. The tip of the plume should point toward the centre of the substrate holder.

After the appropriate alignment had been carefully done, the substrate was attached to the ohmic heater by silver paste which acts as the heat conduction medium between the heater and the substrate. In some cases, a small strip of stainless steel was placed at a corner of the substrate surface. The mark left there after deposition produces a step profile, so that the thickness of the film could be determined by surface profiler (Tencor P-10 surface profiler). The chamber was evacuated by rotary pump to 1 mTorr. Then the heater was set to the desired temperature. When the temperature reached the desired value, oxygen was filled



into the chamber to ~ 100 mTorr for most of the film growth cases. When the ambient pressure and temperature were stabilized, the laser was switched on and pulsed at a repetition of 10 Hz. The laser fluence was ~ 4.8 J/cm². The deposition time was about 10 minutes to obtain films of ~ 250 nm thick. The deposited film was in-situ annealed for 10 minutes at the deposition temperature in order to achieve a better crystalline film.

3.5 Structural analysis of thin films

3.5.1 Thickness measurement

The thickness of the thin films was measured by Tencor P-10 surface profiler. A schematic diagram of an alpha step machine is shown in Fig. 3.3. The needle probe with a tip diameter of $10\mu\text{m}$ is scanned across the step, so that the difference in height between the film and substrate would be measured and the film thickness would be deduced.

Very often we also use the SEM images of the cross-section of the films to counter check thickness measurement.

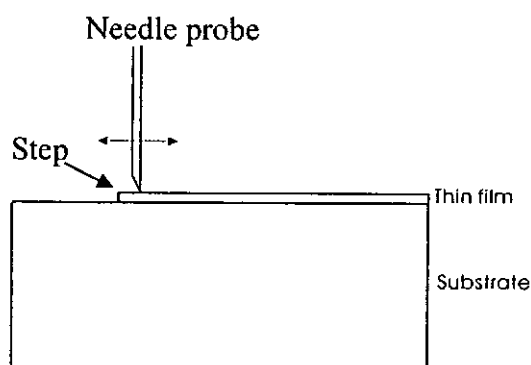


Fig 3.3 Film thickness measurement by surface profiler

3.5.2 In-plane and out-of-plane structure measurement

The structure of the thin films was characterized by x-ray diffractometer (XRD). Fig 3.4 shows the three axes rotation of the sample. We use the CuK_α radiation (1.54\AA) for the XRD. The unwanted CuK_β radiation is filtered out by a nickel filter. The θ - 2θ scan is used to determine the polycrystalline phases of the films. The ω scan is applied to determine the crystalline orientation quality of the film. The in-plane mosaicity and the epitaxial growth relationship of the film and substrate are determined by the 360° - ϕ scan.

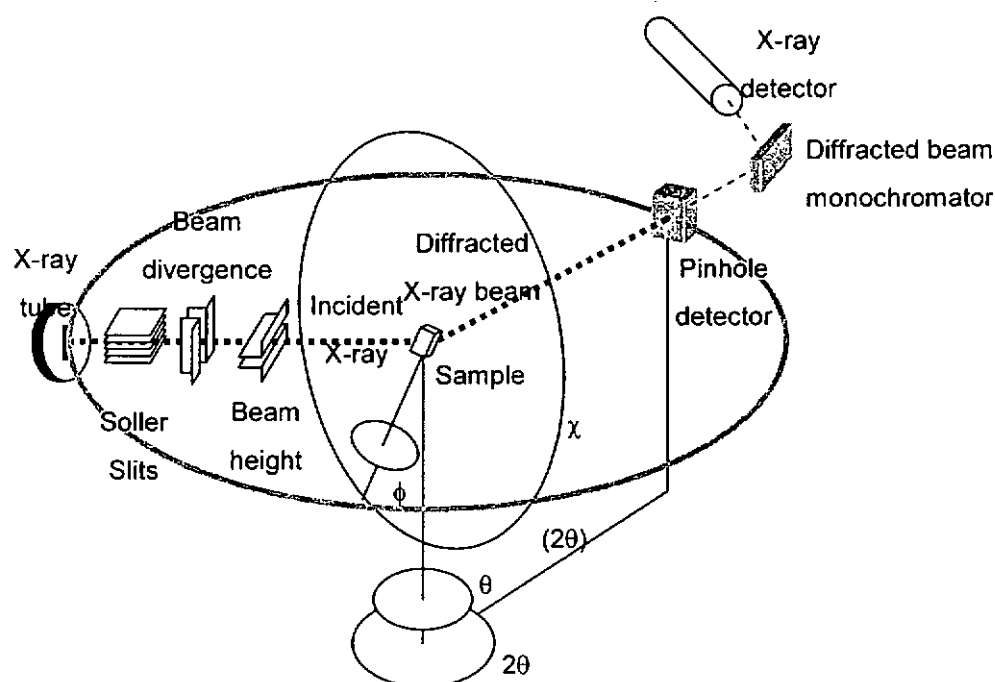


Fig. 3.4 Experimental geometry, showing four primary axes of goniometer, X-ray tube, detector and slits

From the θ - 2θ scan out-of-plane lattice parameter of the film can be determined. The various crystalline phases and orientation of the film are



revealed. At the same time, the substrate orientation is identified in the same θ - 2θ profile.

In the ω scan, which is carried out by fixing the 2θ value at a selected diffraction peak and the angle θ is “rocked” over a few degree. The value of the Full Width at Half Maximum (FWHM) of this “rocking curve” reflects the degree of the crystalline grain orientation in the thin films. The smaller the value of FWHM, the better is the grain orientation. Generally, a FWHM of $\sim 1^\circ$ is considered to be good oriented film and if it is $\leq 1^\circ$, a highly oriented film is suggested.

For the θ - 2θ scan, it only yields the out-of-plane parameter of the film. In order to characterize the epitaxial relation of the film, the in-plane structure of the film should be determined. ϕ -scan is used to characterize the in-plane structure of the film. The ϕ angle is titled to a suitable value first (45° for cubic structures) and the 2θ and θ angles are locked onto the diffraction peaks of a selected plane. For example, we want to evaluate the epitaxial relation of a cubic structure which is (100) out-of-plane oriented film. The family of (h0l) planes of the substrate and film are selected for the investigation. If the ϕ angle is titled to 45° , θ - 2θ scan yield (h0l) diffractions. So if we use the (100) plane diffraction, as the cubic structure is four-fold symmetric, four peaks with separation of 90° corresponding to (101), $(\bar{1}0\bar{1})$, $(10\bar{1})$, and $(\bar{1}01)$ would be observed in the 360° ϕ -scan. If the four characteristic peaks of the film fall on the same ϕ angles as that of the substrate, it can be deduced that the film is cube-on-cube epitaxially grown on the substrate.

3.5.3 Surface morphology measurement

Scanning Electron Microscope (SEM) was used to observe the film surface morphology and film thickness. Generation of particulates is a detrimental issue in fabricating device quality thin films and heterostructures by PLD. The presence of the particulates severely degrades the thin film performance. For this reason we have carried out a set of experiments to investigate the effect of the shadow mask in attempts to eliminate the particulates.

3.6 Electrical properties of thin films

3.6.1 Resistivity against temperature relation

A simple Resistance-Temperature (R-T) measuring setup as shown schematically in Fig. 3.5 was used. Due to the relatively large resistance of the thin film (~several $M\Omega$), a two-point contact setup was adequate to provide accurate measurement. The resistance of the thin film was measured in the temperature range from 80K to 500K. From the R-T relation, we can deduce the film's conduction mechanism at room temperature as well.

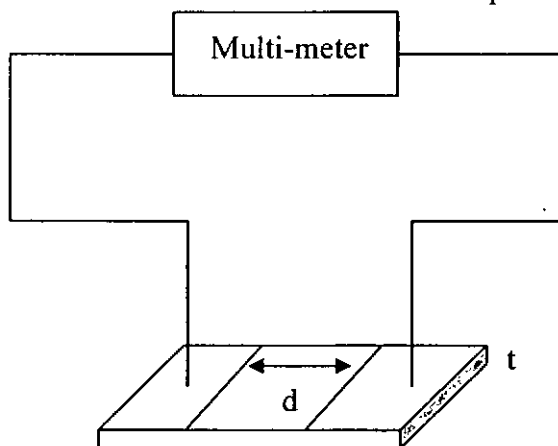


Fig. 3.5 Resistivity vs temperature setup



The sample together with the probe heads were placed in the thermostatic chamber. The resistance at different temperature could be measured directly by the multi-meter. And the resistivity was calculated as: $\rho = w \cdot t \cdot R / d$

and the conductivity $\sigma = 1 / \rho$

3.6.2 Current-voltage measurement

The rectifying properties of a p-n junction could be revealed by measuring its current-voltage characteristics. For precise measurement an electrometer (Keithley 6517A Electrometer / High resistance meter) was used. The lowest current limit and upper current limit are 20pA and 10mA respectively. Typical current flowing through the fabricated p-n junctions ranged from several hundred nano- amperes to several milli- amperes. A typical I-V characteristic of a conventional semiconductor diode is shown in Fig. 3.6. It shows four regions of interest: (i) linear region, (ii) exponential region, (iii) leakage current region, and (iv) breakdown region, where V_D is the diffusion potential and I_s is the saturation current.

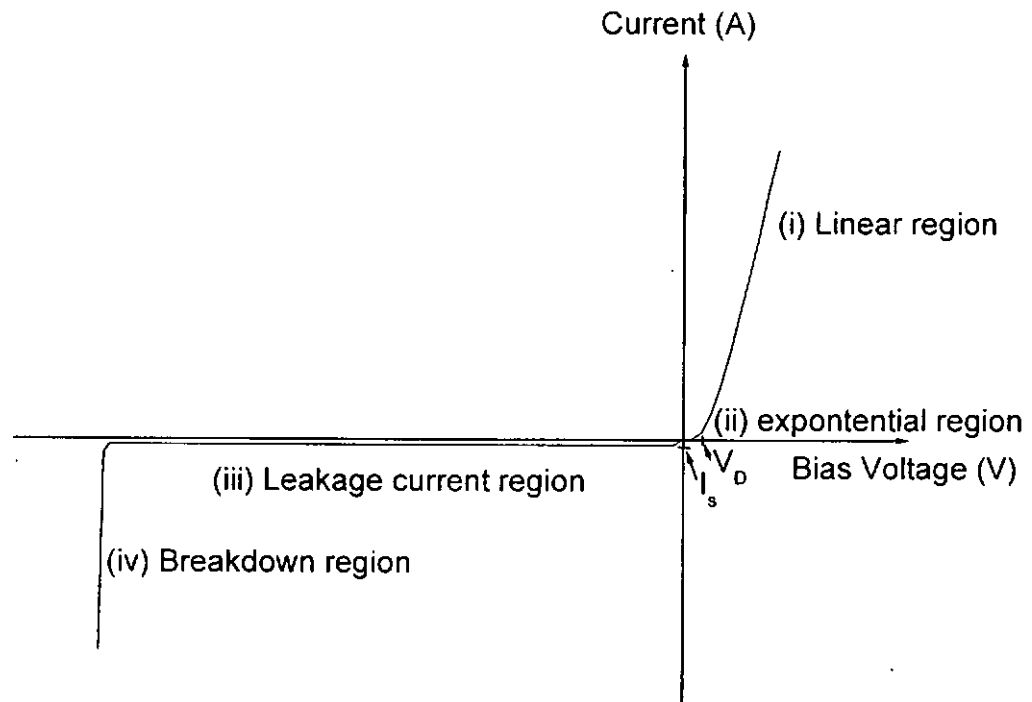


Fig. 3.6 Typical I-V characteristics of conventional p-n junctions

3.6.3 Magnetoresistance (MR) effect

Since magnetoresistive materials, such as LSMO, are used to fabricate the p-n junction, it is of interest to perform the MR effect measurement on the single layer film and also on the p-n junction. The magnetometer (Vibrating sample magnetometer Microprocessor controlled Model 9500) in this study provided a uniform magnetic field up to 1T. Therefore the sample's MR effect could be measured at up to a 1T magnetic field at room temperature.



3.7 Optical properties of thin films

Fabricating transparent all-oxide p-n junction is one of the major tasks in this work. It is essential to measure the optical transmittance of both the single layer film and the p-n junction heterojunction. From the transmission measurement, the optical bandgap of the films can be deduced. It provides useful information for us to investigate the band structure of these junctions. Transparent oxide films always accompany with a wide band gap, having absorption in the UV region. We have reason to expect that the all-oxide p-n junctions exhibit strong photo-response in UV, and they are potentially useful as a UV detector.

3.7.1 Transmission measurement

Transmittance of the films was measured by a UV-VIS Scanning Spectrophotometer, UV-2101PC, which has a broad light source wavelength from 200nm to 900nm. The transmittance against wavelength profile gave clear band gap energy of the materials. The band gap energy and the transition mechanism could be deduced by a profile of $\alpha h\nu^n$ against $h\nu$, where α is the absorption coefficient and n is dependent on the transition mechanism. α can be expressed as

$\alpha = \frac{\ln 1/T}{d}$, where T is the transmittance and d is the thickness of the film. If

$n = 0.5$, the material is of an indirect band gap, and if $n = 2$, it is of a direct band gap



3.7.2 UV Exposure measurement

Both pulsed UV source and continuous wave UV source were employed to measure the photo-excitation of the p-n junction. Pulsed UV source of 248nm and the continuous UV source ranged from 250nm to 500nm were irradiated onto the transparent p-n junction. The photovoltage was plotted against the radiation wavelength, so the wavelength with the highest photo-response could be deduced. Besides the measurement of the photovoltage of the junctions, the photocurrent of the single layer film was measured. The rise and decay times of the photo-response were also studied.



Chapter 4

Fabrication and characterization of $\text{La}_{1-x}\text{Sr}_x\text{MnO}_3 / \text{SrTiO}_3 / \text{La}_{1-y}\text{Sr}_y\text{TiO}_3$ junction

4.1 Introduction

Recently, perovskite oxides are used to fabricate all-oxide p-n junctions [Nakasaka et. al. 2001]. The first of such junction based on $\text{p-La}_{0.85}\text{Sr}_{0.15}\text{MnO}_3/\text{i-SrTiO}_3/\text{n-La}_{0.05}\text{Sr}_{0.95}\text{TiO}_3$ structure was reported in 1999 [Sugiura et. al. 1999, 2001], and a good rectifying property was demonstrated. $\text{La}_{0.85}\text{Sr}_{0.15}\text{MnO}_3$ is a p-type semi-conducting oxide [Kudo et. al. 1998] and $\text{La}_{0.05}\text{Sr}_{0.95}\text{TiO}_3$ is a n-type semi-conducting oxide. Both the $\text{La}_{0.85}\text{Sr}_{0.15}\text{MnO}_3$ and $\text{La}_{0.05}\text{Sr}_{0.95}\text{TiO}_3$ are degenerated semiconductors because of their extremely high charge carrier density at room temperature. Due to the high charge carrier densities $\text{La}_{0.85}\text{Sr}_{0.15}\text{MnO}_3$ and $\text{La}_{0.05}\text{Sr}_{0.95}\text{TiO}_3$ can only form a very narrow depletion layer at the interface. The induced leakage current is therefore prohibitively large. For this reason no rectifying property is observed. So an insulating SrTiO_3 layer was inserted at the interface [Tachiki et. al. 1998, Iwabuchi et. al. 1994] to broaden the transition region and hence reducing the leakage current. Immediately after the success of this all perovskite oxides p-i-n junction, several other publications on the all-oxide p-n junction have been reported. For example, $(\text{La,Ba})\text{MnO}_3/\text{NSTO}$ [Tanaka et. al. 2002], and $\text{La}_{0.32}\text{Pr}_{0.35}\text{Ca}_{0.33}\text{MnO}_3/\text{NSTO}$ [Sun et. al. 2004] p-n junctions have been fabricated.



In this study, the effect of film composition on the junction characteristics was investigated. Two different composition LSMO targets ($\text{La}_{0.85}\text{Sr}_{0.15}\text{MnO}_3$, and $\text{La}_{0.7}\text{Sr}_{0.3}\text{MnO}_3$) and three different composition LSTO targets ($\text{La}_{0.05}\text{Sr}_{0.95}\text{TiO}_3$, $\text{La}_{0.1}\text{Sr}_{0.9}\text{TiO}_3$, and $\text{La}_{0.15}\text{Sr}_{0.85}\text{TiO}_3$) have been prepared. Consequently p-i-n⁺ junctions with layers of different combinations were fabricated. The change in chemical composition of the oxide thin films may alter the charge carrier concentration. This, in turn, changes the conductivity of the oxide layer and hence varies the series resistance of the p-n junction. Therefore an increase in conductivity of individual oxide layer affects the current flow in the junction. In addition the temperature effect on the I-V characteristics has also been investigated.



4.2 Structural characteristics of $\text{La}_{1-x}\text{Sr}_x\text{MnO}_3$, and $\text{La}_{1-y}\text{Sr}_y\text{TiO}_3$ targets

4.2.1 Fabrication of $\text{La}_{1-x}\text{Sr}_x\text{MnO}_3$, and $\text{La}_{1-y}\text{Sr}_y\text{TiO}_3$ targets

Standard solid state reaction method was used to fabricate all the $\text{La}_{1-x}\text{Sr}_x\text{MnO}_3$, and $\text{La}_{1-y}\text{Sr}_y\text{TiO}_3$ targets. The chemicals involved and their appropriate weight ratios are shown in Table 4.1.

Table 4.1 Required chemical and their weight

	La_2O_3	SrCO_3	MnO_2	TiO_2
$\text{La}_{0.7}\text{Sr}_{0.3}\text{MnO}_3$				
Molar Weight	114.16 g	44.74 g	86.95 g	-
Desired Weight	5.71 g	2.24 g	4.35 g	-
$\text{La}_{0.85}\text{Sr}_{0.15}\text{MnO}_3$				
Molar Weight	138.62 g	22.37 g	86.95 g	-
Desired Weight	6.93 g	1.12 g	4.35 g	-
$\text{La}_{0.05}\text{Sr}_{0.95}\text{TiO}_3$				
Molar Weight	8.15 g	141.67 g	-	79.91 g
Desired Weight	0.41 g	7.08 g	-	4.0 g
$\text{La}_{0.1}\text{Sr}_{0.9}\text{TiO}_3$				
Molar Weight	16.31 g	134.21 g	-	79.91 g
Desired Weight	0.82 g	6.71 g	-	4.0 g
$\text{La}_{0.15}\text{Sr}_{0.85}\text{TiO}_3$				
Molar Weight	24.46 g	126.75 g	-	79.91 g
Desired Weight	1.22 g	6.34 g	-	4.0 g

The amount of oxide powder was weighed according to the desired stoichiometric ratio. The powder was mixed with ethanol and then ball milled for 10 hours. Calcinations was carried out in order to get rid of the organic



components from the mixed powder and to allow the chemical reaction to occur. The calcinated powder was compressed by an oil-compressor at a pressure of 3.5 Ton into 3 mm thick circular pellets of 2.5 cm in diameter. Sintering was then carried out to form the desired target. The calcinations and sintering temperatures were tabulated in Table 4.2. Each of the calcinations and sintering processes were done in air and lasted for 10 hours at the desired temperature.

Table 4.2 Calcination and sintering temperature

	Calcination Temp.	Sintering Temp.
$\text{La}_{1-x}\text{Sr}_x\text{MnO}_3$	1200 °C	1320 °C
$\text{La}_{1-y}\text{Sr}_y\text{TiO}_3$	1200 °C	1400 °C

4.2.2 Structural characteristics of $\text{La}_{1-x}\text{Sr}_x\text{MnO}_3$ and $\text{La}_{1-y}\text{Sr}_y\text{TiO}_3$ targets

XRD was carried out for structural characterization of the as-prepared targets. Fig. 4.1 and Fig. 4.2 are the θ -2 θ scans of all the $\text{La}_{1-x}\text{Sr}_x\text{MnO}_3$, and $\text{La}_{1-y}\text{Sr}_y\text{TiO}_3$ targets. Major sharp x-ray diffraction peaks are well matched with those listed in the database (International centre for Diffraction Data, ICDD). EDX was carried out to verify the chemical composition.

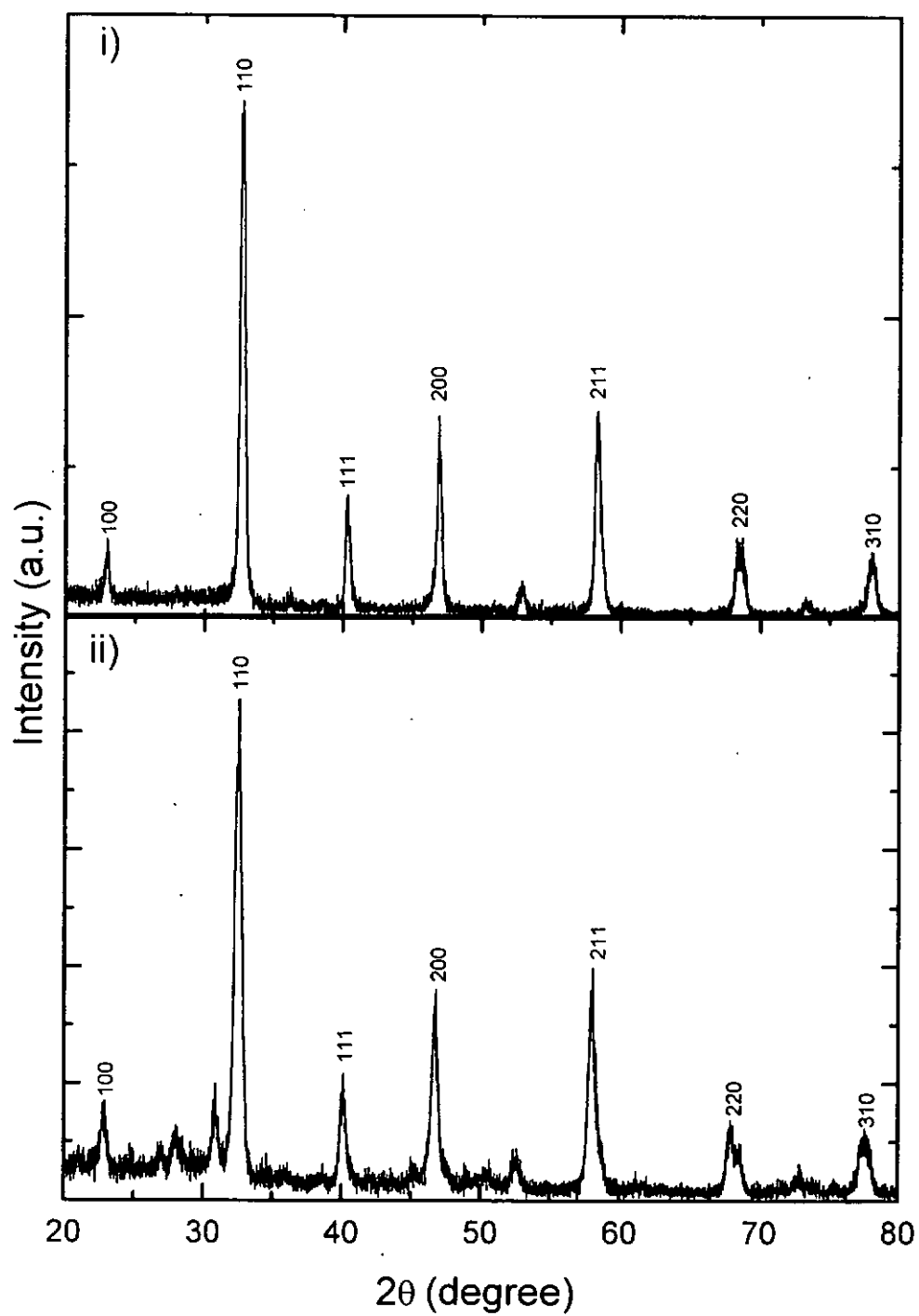


Fig. 4.1 XRD patterns of LSMO target with different composition, i) La_{0.7}Sr_{0.3}MnO₃ and ii) La_{0.85}Sr_{0.15}MnO₃

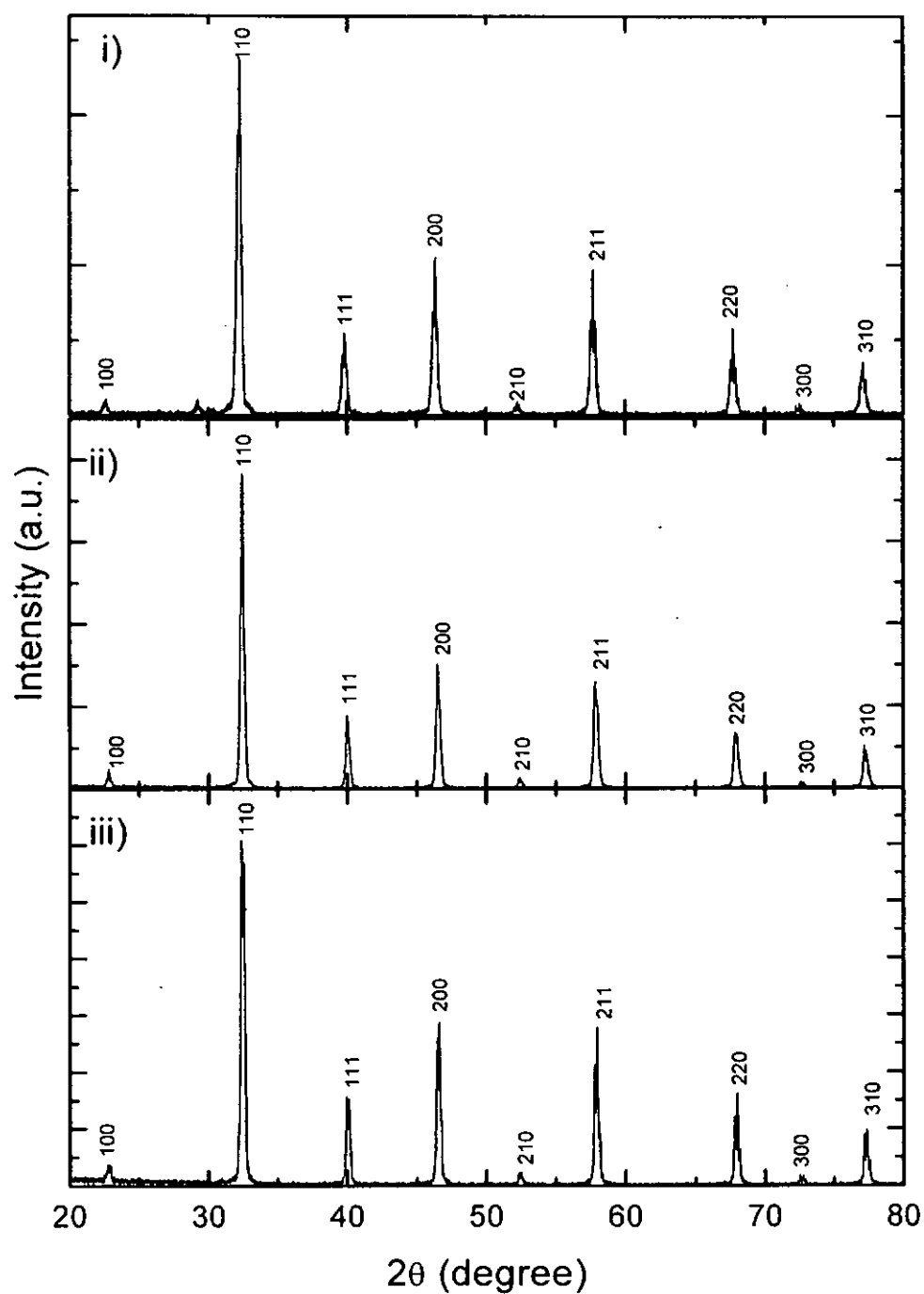


Fig. 4.2 XRD patterns of LSTO target with different composition, i) $\text{La}_{0.05}\text{Sr}_{0.95}\text{TiO}_3$, ii) $\text{La}_{0.1}\text{Sr}_{0.9}\text{TiO}_3$, and iii) $\text{La}_{0.15}\text{Sr}_{0.85}\text{TiO}_3$



4.3 Structural characteristics of $\text{La}_{1-x}\text{Sr}_x\text{MnO}_3$, and $\text{La}_{1-y}\text{Sr}_y\text{TiO}_3$ thin films and $p\text{-La}_{1-x}\text{Sr}_x\text{MnO}_3/i\text{-SrTiO}_3/n\text{-La}_{1-y}\text{Sr}_y\text{TiO}_3$ tri-layer structure

4.3.1 Fabrication of LSMO, LSTO and STO thin films

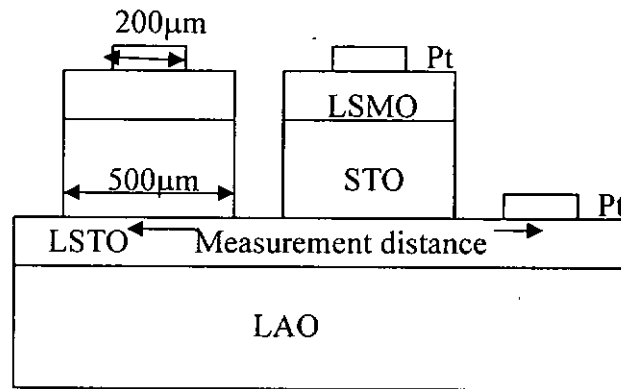
All the LSMO, LSTO and STO films were deposited by PLD. For these materials, their lattice constants are more or less the same at around 3.9\AA . To facilitate a lattice matching condition, commercial single crystal (100) LaAlO_3 (LAO) was selected as the deposition substrate; LAO is cubic in structure and has a lattice mismatch of less than 5% to all the three oxides studied in this work. All films were fabricated at a substrate temperature of 650°C and an ambient oxygen pressure of 100mTorr. The laser fluence was kept to $\sim 5\text{ Jcm}^{-2}$. The deposition times for LSMO and LSTO thin films were 7 minutes and that for STO was 14 minutes. The resulted film thickness is $\sim 400\text{nm}$ for STO and $\sim 200\text{nm}$ for both LSMO and LSTO. The films are poor in contact with the connecting aluminum wire. A $\phi\text{-}200\mu\text{m}$ platinum spot was deposited on top of both LSMO and LSTO films. A sufficient high substrate temperature could improve the adhesion and create the ohmic contact between the oxide films and the Pt electrode. Therefore the deposition of Pt was carried out at a substrate temperature of 300°C and at a pressure of several mTorr.

During the p-i-n junction production, LSTO film was first deposited on (100) LAO single crystal. It is followed by a STO insulating layer. The STO and the final LSMO film were deposited as pattern of 0.25mm^2 square array via transmission through a thin stainless steel shadow mask of the same pattern.



Spot of Pt electrodes, which has a diameter of $200\mu\text{m}$, was laid on top of the small part of LSMO and LSTO layer. Fig. 4.3 is the schematic diagram and the top view of real image of the LSMO/STO/LSTO junction. Fig. 4.4 shows the SEM cross-sections images of the $\text{p-La}_{0.85}\text{Sr}_{0.15}\text{MnO}_3/\text{i-SrTiO}_3/\text{n-La}_{0.05}\text{Sr}_{0.95}\text{TiO}_3$ and $\text{p-La}_{0.7}\text{Sr}_{0.3}\text{MnO}_3/\text{i-SrTiO}_3/\text{n-La}_{0.05}\text{Sr}_{0.95}\text{TiO}_3$ heterostructures. The SEM cross section diagram gives the actual thicknesses of the $\text{La}_{0.85}\text{Sr}_{0.15}\text{MnO}_3$ and $\text{La}_{0.7}\text{Sr}_{0.3}\text{MnO}_3$ film. Due to the likeness of composition and structural character of SrTiO_3 and $\text{La}_{0.05}\text{Sr}_{0.95}\text{TiO}_3$, no distinct boundary between these two layers is observed. Their combined thickness is about to be 600nm for both junctions. From the previous experimental results, a SrTiO_3 film of thickness of 400nm would be produced for a 14 minutes deposition duration. Hence the thicknesses of $\text{La}_{0.05}\text{Sr}_{0.95}\text{TiO}_3$ and SrTiO_3 should be 200nm and 400nm respectively.

i)



ii)

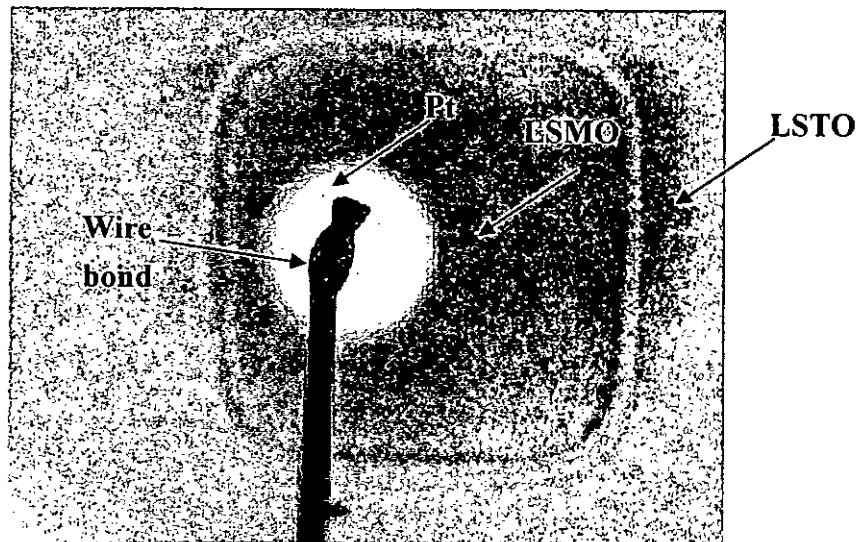


Fig. 4.3 i) The schematic diagram of the p-i-n junction, ii) the top view of real image of the p-i-n junction.

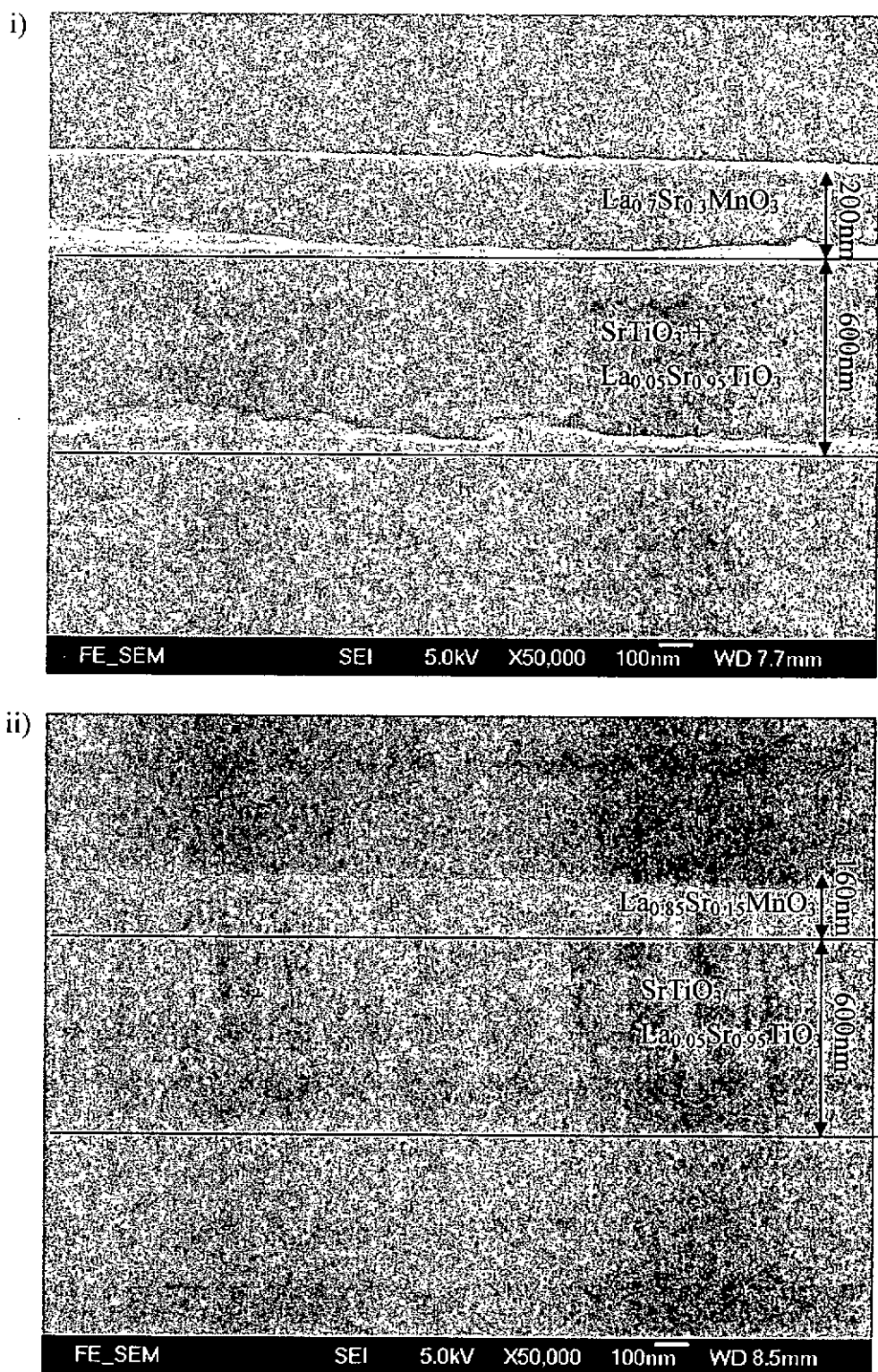


Fig. 4.4 SEM images of the cross-section of the p-i-n junctions, i) p-La_{0.7}Sr_{0.3}MnO₃/i-SrTiO₃/n-La_{0.05}Sr_{0.95}TiO₃ and ii) p-La_{0.85}Sr_{0.15}MnO₃/i-SrTiO₃/ n-La_{0.05}Sr_{0.95}TiO₃



4.3.2 Structural characterization of $\text{La}_{1-x}\text{Sr}_x\text{MnO}_3$ thin films

Before the junction fabrication, single layer LSMO films grown on (100) LAO substrates were examined, especially the structural properties of the grown films on LAO substrate. LSMO has a pseudocubic structure and the out-of-plane lattice parameter (a) was found to be $\sim 3.9\text{\AA}$. Although LSMO has a lattice mismatch of $\sim 2.5\%$ with LAO, the epitaxial growth of LSMO is expected.

The composition of LSMO would change its lattice dimension. LSMO with more strontium doping has a smaller lattice parameter a . For example, the lattice constants of ceramic $\text{La}_{0.85}\text{Sr}_{0.15}\text{MnO}_3$ and $\text{La}_{0.7}\text{Sr}_{0.3}\text{MnO}_3$ are 3.88 \AA and 3.87 \AA respectively. Fig. 4.5 presents the θ - 2θ scans of LSMO thin film grown on (100) single crystal. The θ - 2θ scans indicate the growth of single phase LSMO film on LAO. Only the (h00) oriented peaks are observed. Inset diagram gives the (200) rocking curves for $\text{La}_{0.85}\text{Sr}_{0.15}\text{MnO}_3$ and $\text{La}_{0.7}\text{Sr}_{0.3}\text{MnO}_3$ with FWHMs of 0.5° and 0.4° respectively.

So far the out-of-plane structural characteristic of the LSMO film was determined. However the in-plane structural quality and grain orientation mosaicity could not be determined by the above measurement. Therefore additional ϕ -scan was applied to examine the in-plane parameter of the film. Fig. 4.6 shows the ϕ -scans of (202) $\text{La}_{0.85}\text{Sr}_{0.15}\text{MnO}_3$ and (202) LAO reflection peaks. For these ϕ -scans, the angle of χ was tilted to 45° , so that the (h0l) phase family aligned normal to the incident x-ray beam at some specific



ϕ angles. For example, in a cubic system the (h0l) family planes meet the incident x-ray beam at Bragg's condition for four times during a 360° ϕ -rotation. Consequently four sharp peaks separated by 90° are obtained in the ϕ -scan. The four fold symmetry observed in the XRD patterns confirms the cubic structure of the grown $\text{La}_{0.85}\text{Sr}_{0.15}\text{MnO}_3$ film and LAO substrate. The four characteristic peaks of the $\text{La}_{0.85}\text{Sr}_{0.15}\text{MnO}_3$ reflections are very sharp and their ϕ angle values match that of the LAO reflections. This is a clear indication of cube-on-cube epitaxially grown LSMO film on LAO substrate. Although it is not shown here, the ϕ -scan of (202) $\text{La}_{0.7}\text{Sr}_{0.3}\text{MnO}_3$ reveals cube-on-cube growth relation between the film and substrate as well.

In conclusion, both single phased (100) $\text{La}_{0.85}\text{Sr}_{0.15}\text{MnO}_3$ and (100) $\text{La}_{0.7}\text{Sr}_{0.3}\text{MnO}_3$ were grown on single crystal (100) LAO substrate epitaxially. Good crystalline structure and grain orientation were found for these two films deposited at substrate temperature of 650°C .

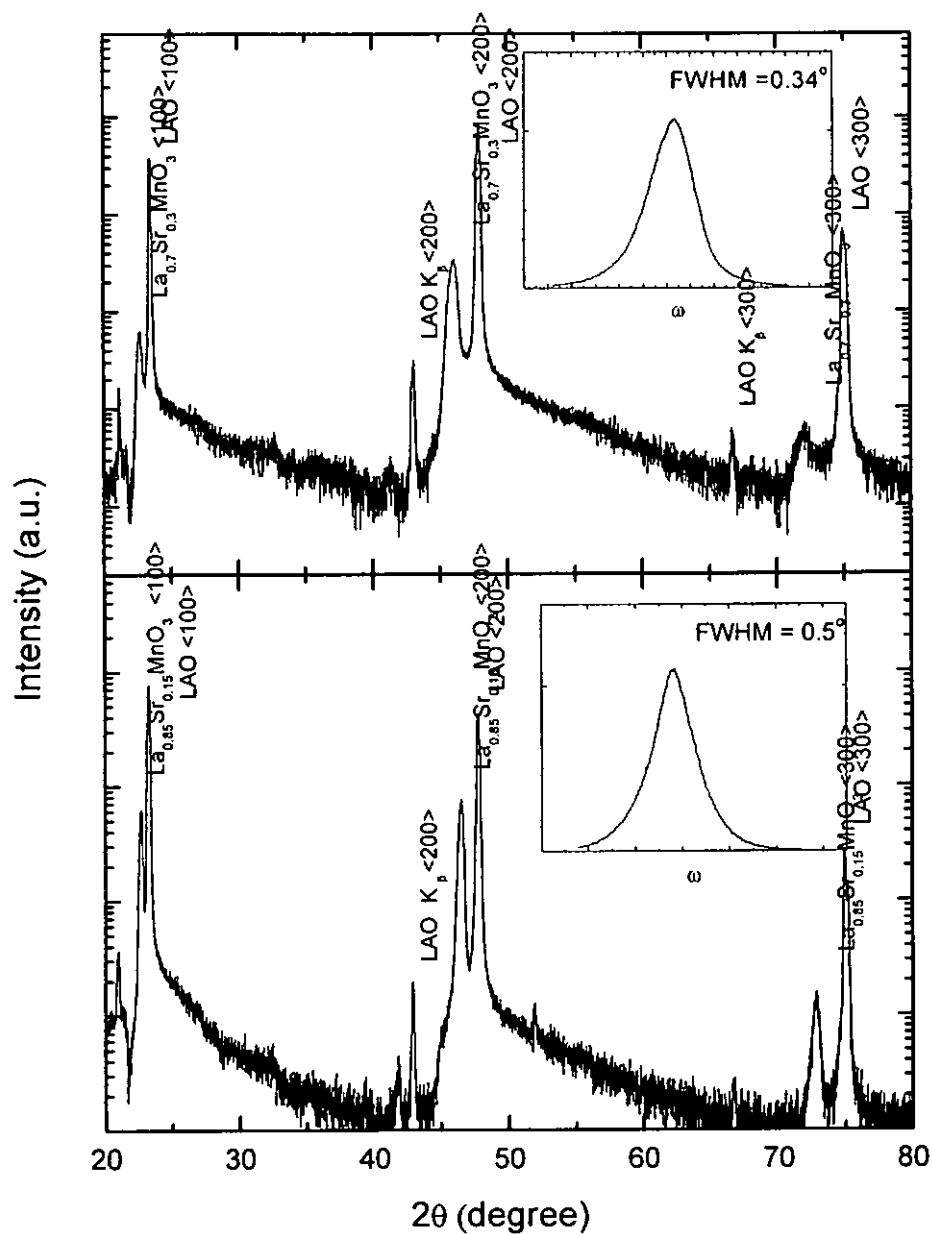


Fig. 4.5 X-ray θ - 2θ diffraction patterns for i) the $\text{La}_{0.7}\text{Sr}_{0.3}\text{MnO}_3/\text{LAO}$ structure and ii) the $\text{La}_{0.85}\text{Sr}_{0.15}\text{MnO}_3/\text{LAO}$ structure, inset shows the rocking curve of these two LSMO films

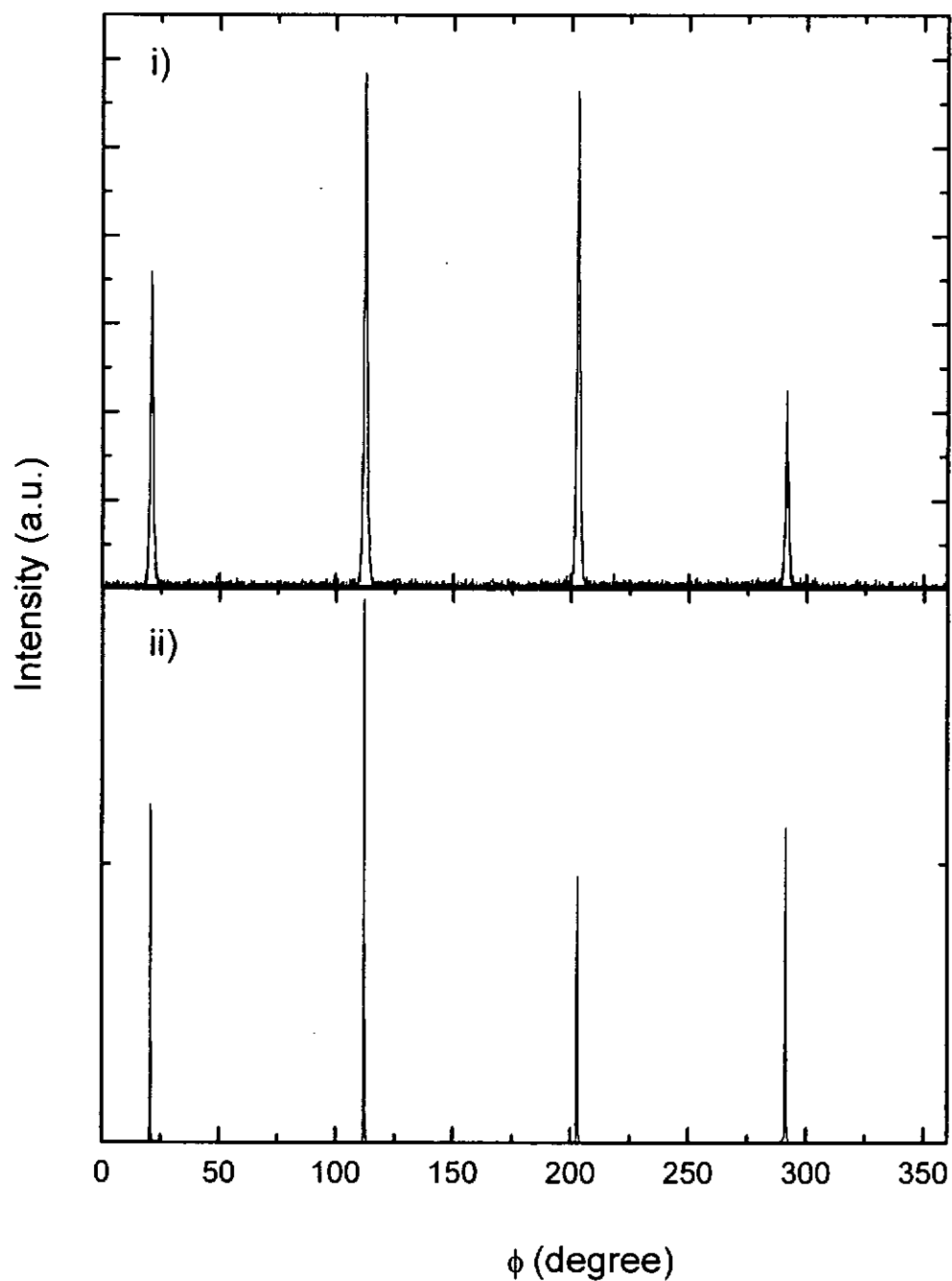


Fig. 4.6 ϕ scans of i) (202) $\text{La}_{0.85}\text{Sr}_{0.15}\text{MnO}_3$ and ii) (202) LAO reflection peaks



4.3.3 Structural characterization of $\text{La}_{1-y}\text{Sr}_y\text{TiO}_3$ thin films

LSTO thin films were grown on single crystal (100) LAO substrate at a substrate temperature of 650°C. Fig. 4.7 displays the θ -2 θ scans of the $\text{La}_{1-y}\text{Sr}_y\text{TiO}_3$ /LAO heterostructures. Three different compositions of LSTO films, namely $\text{La}_{0.05}\text{Sr}_{0.95}\text{TiO}_3$, $\text{La}_{0.1}\text{Sr}_{0.9}\text{TiO}_3$ and $\text{La}_{0.15}\text{Sr}_{0.85}\text{TiO}_3$ have been studied. Only the (h00) family planes are observed, implying the single phased LSTO film growth. All the films have the same lattice constant of 3.93 Å, and the FWHMs of the rocking curve of the films are less than 1° as illustrated in the inset of Fig. 4.7. Fig. 4.8 presents the ϕ -scan profiles of (202) $\text{La}_{0.1}\text{Sr}_{0.9}\text{TiO}_3$ and the corresponding profiles of the substrate. The four sharp peaks with 90° apart on the ϕ -scan is a good indication of four fold symmetry of a cubic structure. The completely matched ϕ angles of diffraction of (202) $\text{La}_{0.1}\text{Sr}_{0.9}\text{TiO}_3$ and (202) LAO characteristics peaks, suggests a cube-on-cube heteroepitaxy. Similar results are also observed in $\text{La}_{0.05}\text{Sr}_{0.9}\text{TiO}_3$ and $\text{La}_{0.15}\text{Sr}_{0.9}\text{TiO}_3$ films.

It has been revealed that good epitaxial LSMO and LSTO thin films could be easily grown on LAO single crystal substrate. It can be deduced that epitaxially grown tri-layer p-LSMO/i-STO/n-LSTO heterostructure could also be easily obtained. In the following sections, the tri-layered structures are reported.

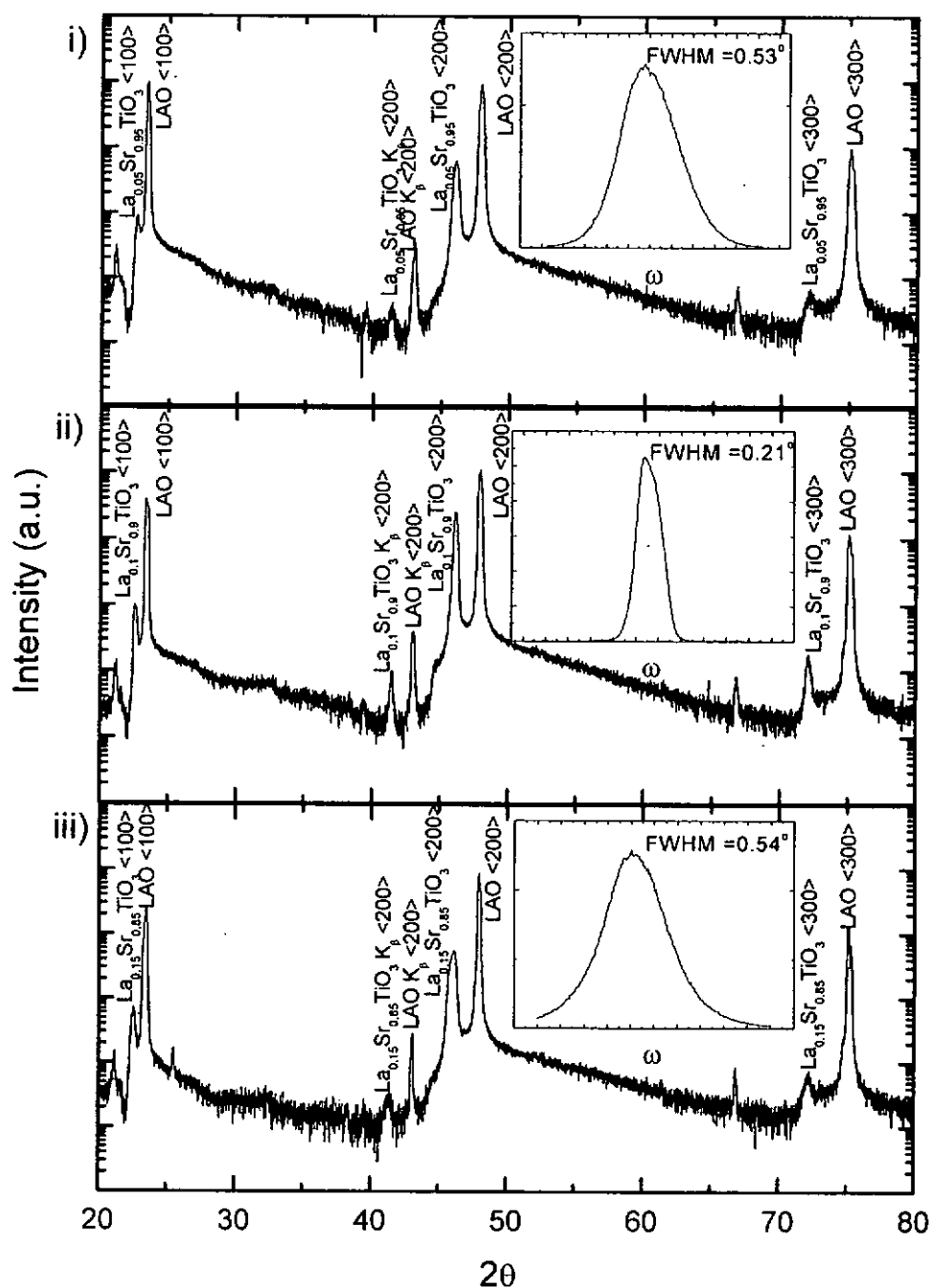


Fig. 4.7 X-ray θ - 2θ diffraction patterns for i) the $\text{La}_{0.05}\text{Sr}_{0.95}\text{TiO}_3/\text{LAO}$ structure, ii) the $\text{La}_{0.1}\text{Sr}_{0.9}\text{TiO}_3/\text{LAO}$ structure, and iii) the $\text{La}_{0.15}\text{Sr}_{0.85}\text{TiO}_3/\text{LAO}$ structure, the inset diagram shows the rocking curve of these three LSTO films

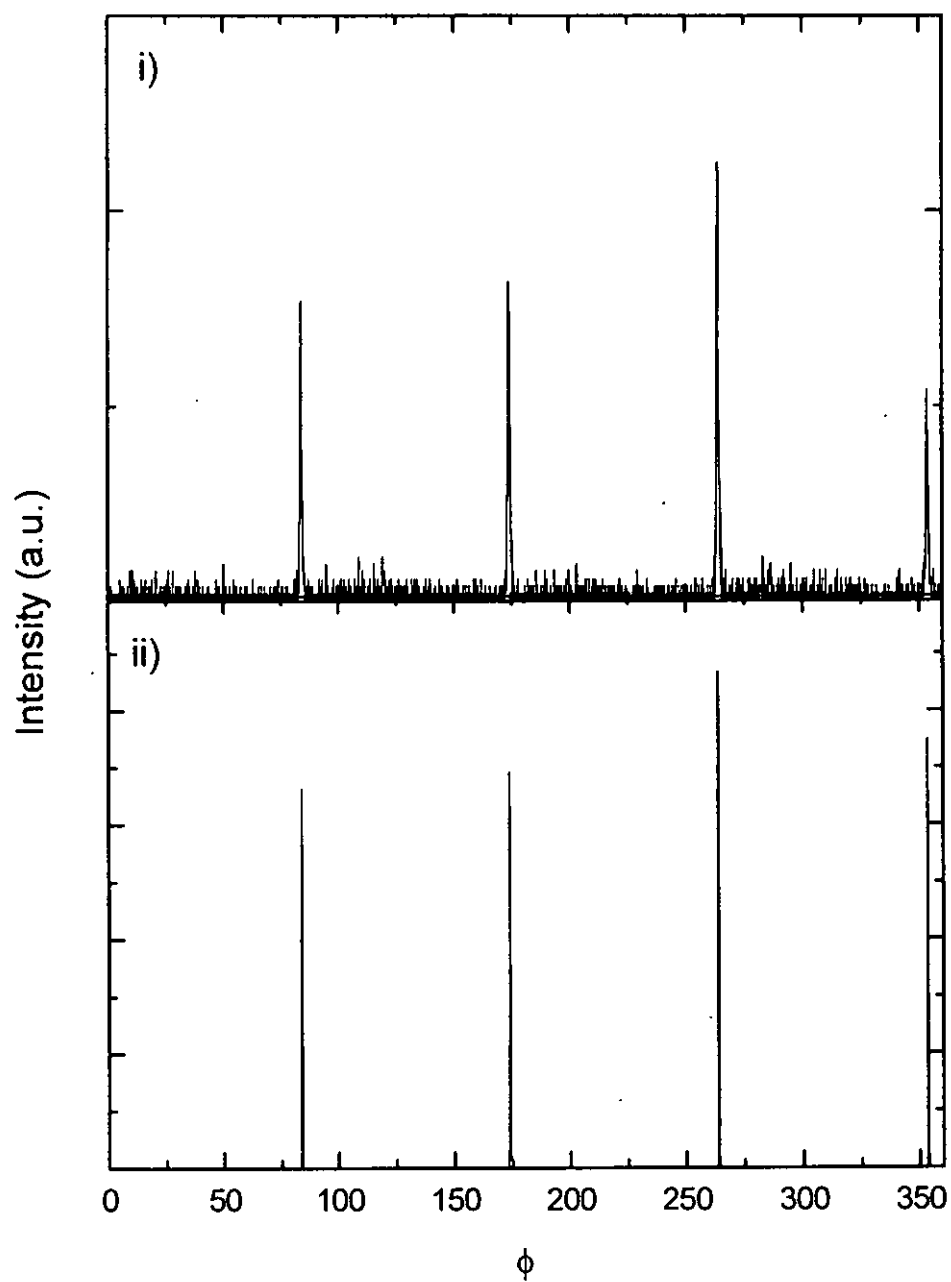


Fig. 4.8 ϕ scans of i) (202) $\text{La}_{0.1}\text{Sr}_{0.9}\text{TiO}_3$ and ii) its corresponding (202) LAO reflection peaks



4.3.4 Structural characterization of p-La_{1-x}Sr_xMnO₃/i-SrTiO₃ n-La_{1-y}Sr_yTiO₃ tri-layer structure.

The structural characteristics of the single layered LSMO and LSTO films were analyzed in the previous two sections. We now come to study the structural properties of the tri-layer junctions. In this section, the θ -2 θ scan, ω scan and ϕ scan of the two p-i-n junctions, La_{0.85}Sr_{0.15}MnO₃/SrTiO₃/La_{0.05}Sr_{0.95}TiO₃ and La_{0.7}Sr_{0.3}MnO₃/SrTiO₃/La_{0.05}Sr_{0.95}TiO₃, are investigated.

A sharp $\langle 200 \rangle$ La_{0.05}Sr_{0.95}TiO₃ reflection peak and a smaller $\langle 200 \rangle$ La_{0.85}Sr_{0.15}MnO₃ reflection peak are found in between 45° and 50° in Fig. 4.9. Since the lattice constant of La_{0.05}Sr_{0.95}TiO₃ matches closely with that of SrTiO₃, it is believed that their reflection peaks coincided with each other in the XRD profiles and could not be resolved. So it is assured that all the La_{0.05}Sr_{0.95}TiO₃ reflections shown on the XRD profile mingle with the SrTiO₃ reflections. The lattice constant of La_{0.05}Sr_{0.95}TiO₃ is 3.93 Å and that of La_{0.85}Sr_{0.15}MnO₃ is 3.89 Å. Their lattice constants also close to its bulk target values, indicating no internal strain on the film. Due to the close lattice constants between the two films, the reflection peak $\langle 200 \rangle$ La_{0.85}Sr_{0.15}MnO₃ overlaps with the tail of the $\langle 200 \rangle$ La_{0.05}Sr_{0.95}TiO₃ reflection. Reflections from these two layers, however, can be resolve at higher diffraction order, e.g. the $\langle 300 \rangle$ La_{0.85}Sr_{0.15}MnO₃ and $\langle 300 \rangle$ La_{0.05}Sr_{0.95}TiO₃ reflections. There are no more XRD peaks other than the (h00) families of La_{0.85}Sr_{0.15}MnO₃, La_{0.05}Sr_{0.95}TiO₃ and LAO. This is a good evidence that all the layers are single



phase and oriented.

The rocking curves of $\text{La}_{0.85}\text{Sr}_{0.15}\text{MnO}_3$ and $\text{La}_{0.05}\text{Sr}_{0.95}\text{TiO}_3$ are shown in Fig. 4.10. The FWHM of $\text{La}_{0.85}\text{Sr}_{0.15}\text{MnO}_3$ and $\text{La}_{0.05}\text{Sr}_{0.95}\text{TiO}_3$ are 0.59° and 0.35° respectively. The narrow peaks of the rocking curves suggest growth of highly oriented films.

The epitaxial relation between the films and the substrate are shown in Fig. 4.11. The three patterns are the ϕ -scan measurement of $\langle 202 \rangle$ $\text{La}_{0.85}\text{Sr}_{0.15}\text{MnO}_3$, $\langle 202 \rangle$ $\text{La}_{0.05}\text{Sr}_{0.95}\text{TiO}_3$ and $\langle 202 \rangle$ LAO. The four fold symmetry confirms the cubic structure of the films and the substrate. The completely matched ϕ angles of the reflection peaks among the three layers ($\text{La}_{0.85}\text{Sr}_{0.15}\text{MnO}_3$, SrTiO_3 , and $\text{La}_{0.05}\text{Sr}_{0.95}\text{TiO}_3$) suggest cube-on-cube growth on LAO substrate.

Apart from the $\text{La}_{0.85}\text{Sr}_{0.15}\text{MnO}_3/\text{SrTiO}_3/\text{La}_{0.05}\text{Sr}_{0.95}\text{TiO}_3$ junction, structural analysis was carried out for the $\text{La}_{0.7}\text{Sr}_{0.3}\text{MnO}_3/\text{SrTiO}_3/\text{La}_{0.05}\text{Sr}_{0.95}\text{TiO}_3$ junction too. It shows a similar XRD θ - 2θ profile as $\text{La}_{0.85}\text{Sr}_{0.15}\text{MnO}_3/\text{SrTiO}_3/\text{La}_{0.05}\text{Sr}_{0.95}\text{TiO}_3$ junction. The SrTiO_3 reflection peak is completely coalesced with the $\text{La}_{0.05}\text{Sr}_{0.95}\text{TiO}_3$ reflection peak, just as in $\text{La}_{0.85}\text{Sr}_{0.15}\text{MnO}_3/\text{SrTiO}_3/\text{La}_{0.05}\text{Sr}_{0.95}\text{TiO}_3$ junction. Moreover the $\langle 200 \rangle$ $\text{La}_{0.85}\text{Sr}_{0.15}\text{MnO}_3$ reflection peak is displaced from the $\langle 200 \rangle$ $\text{La}_{0.05}\text{Sr}_{0.95}\text{TiO}_3$ reflection as shown in Fig. 4.12. It is due to the larger difference in lattice constants between $\text{La}_{0.7}\text{Sr}_{0.3}\text{MnO}_3$ and $\text{La}_{0.05}\text{Sr}_{0.95}\text{TiO}_3$ than $\text{La}_{0.85}\text{Sr}_{0.15}\text{MnO}_3$ and $\text{La}_{0.05}\text{Sr}_{0.95}\text{TiO}_3$.

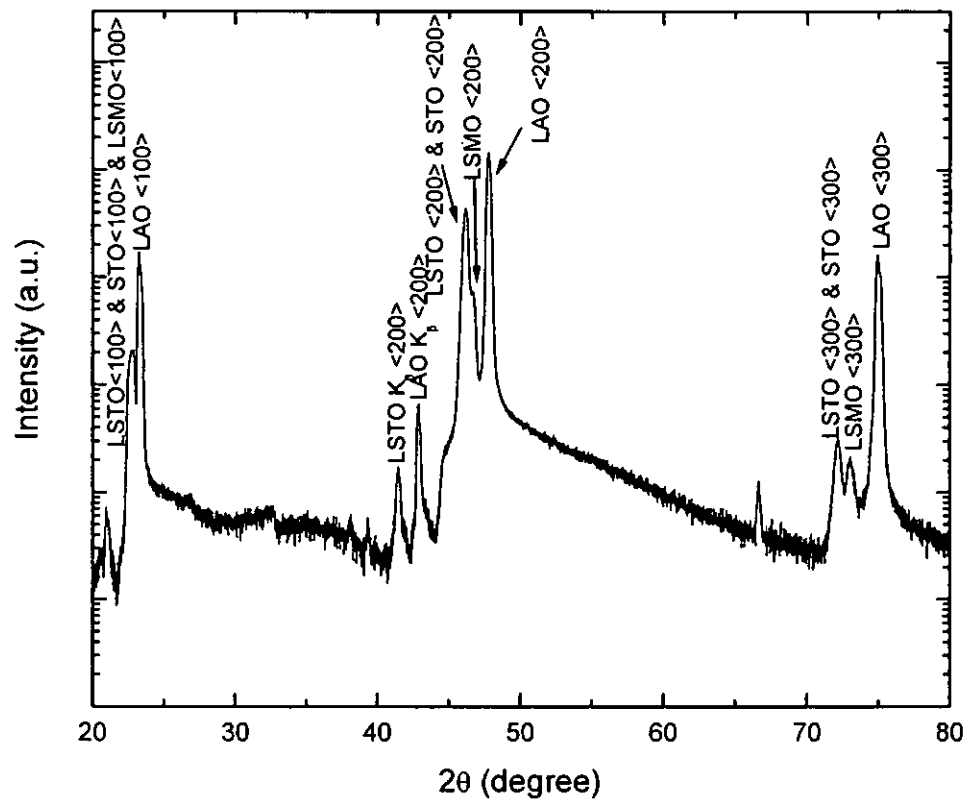


Fig. 4.9 XRD θ - 2θ scan of $\text{La}_{0.85}\text{Sr}_{0.15}\text{MnO}_3/\text{SrTiO}_3/\text{La}_{0.05}\text{Sr}_{0.95}\text{TiO}_3$ tri-layer p-i-n⁺ junction

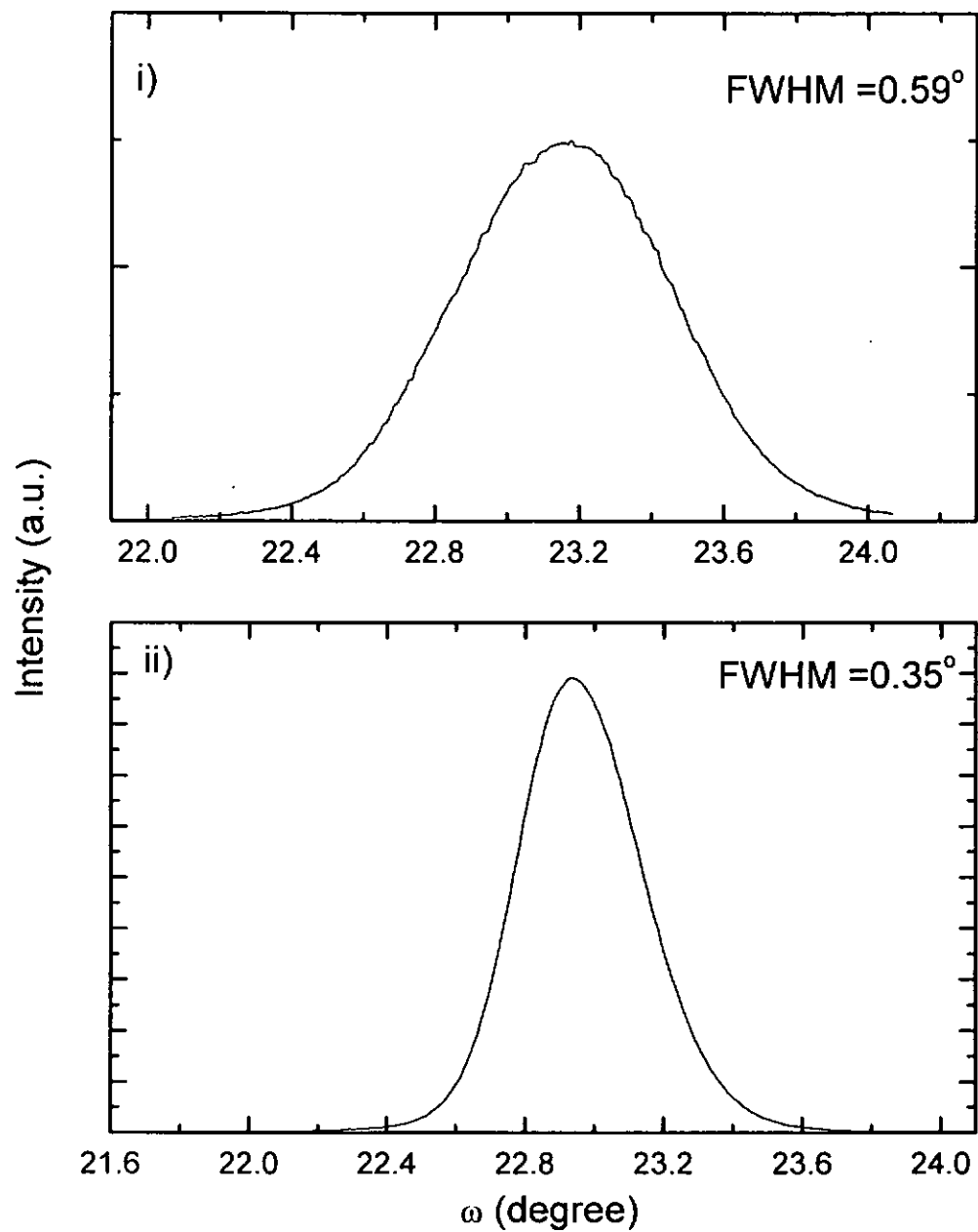


Fig. 4.10 Rocking curves of i) $\text{La}_{0.85}\text{Sr}_{0.15}\text{MnO}_3$ and ii) $\text{La}_{0.05}\text{Sr}_{0.95}\text{TiO}_3$ for the $\text{La}_{0.85}\text{Sr}_{0.15}\text{MnO}_3/\text{SrTiO}_3/\text{La}_{0.05}\text{Sr}_{0.95}\text{TiO}_3$ junction

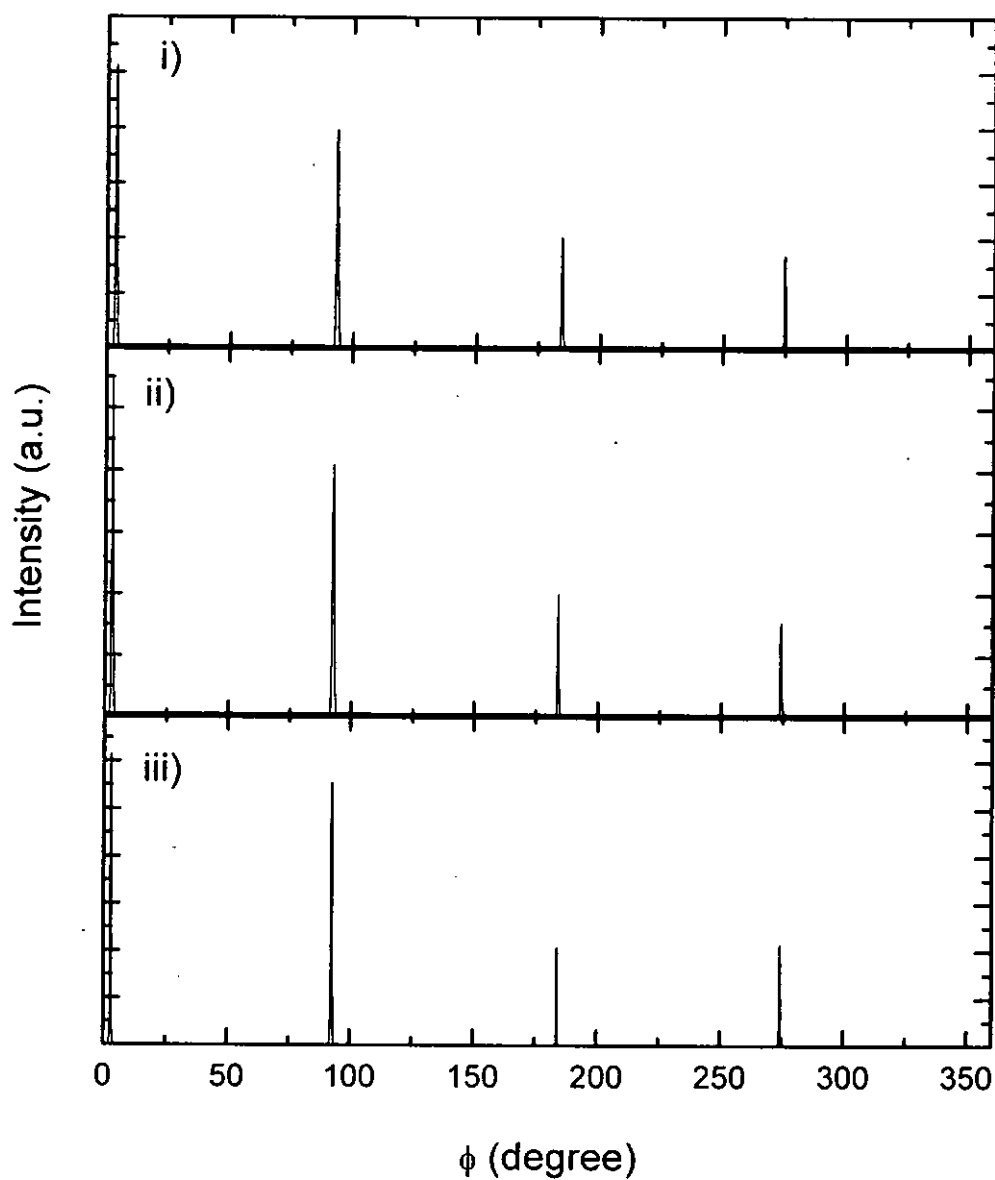


Fig. 4.11 XRD ϕ -scan of the i) $\langle 202 \rangle$ La_{0.85}Sr_{0.15}MnO₃, ii) $\langle 202 \rangle$ La_{0.05}Sr_{0.95}TiO₃ and iii) $\langle 202 \rangle$ LAO for the La_{0.85}Sr_{0.15}MnO₃/SrTiO₃/La_{0.05}Sr_{0.95}TiO₃ junction



From Fig. 4.13, the rocking curves of both the $\text{La}_{0.7}\text{Sr}_{0.3}\text{MnO}_3$ and $\text{La}_{0.05}\text{Sr}_{0.95}\text{TiO}_3$ films have the FWHM of 0.3° . The small FWHM values imply good orientation of the films. The $360^\circ \phi$ -scans of the three layers are shown on Fig. 4.14. It also confirms the epitaxial relation among the $\text{La}_{0.7}\text{Sr}_{0.3}\text{MnO}_3$, SrTiO_3 , $\text{La}_{0.05}\text{Sr}_{0.95}\text{TiO}_3$ and LAO.

The tri-layer system consisting of LSMO, LSTO and STO films are easily grown on LAO by the PLD system. All the three layers not only show good crystallinity, but possess the good epitaxial relation with each other. In conclusion, the tri-layer heteroepitaxial p-i-n junctions with the combination of LSMO, LSTO and STO could be easily grown with good structure by the PLD technique.

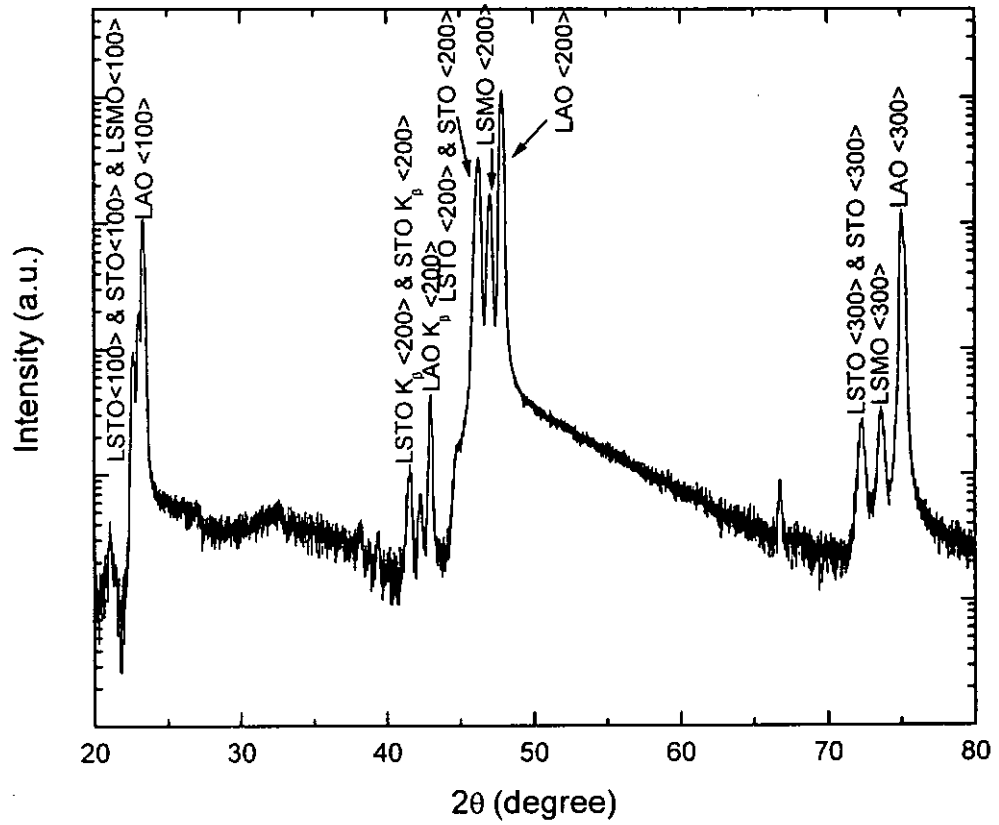


Fig. 4.12 XRD θ - 2θ scan of $\text{La}_{0.7}\text{Sr}_{0.3}\text{MnO}_3/\text{SrTiO}_3/\text{La}_{0.05}\text{Sr}_{0.95}\text{TiO}_3$ for tri-layer p-i-n⁺ junction

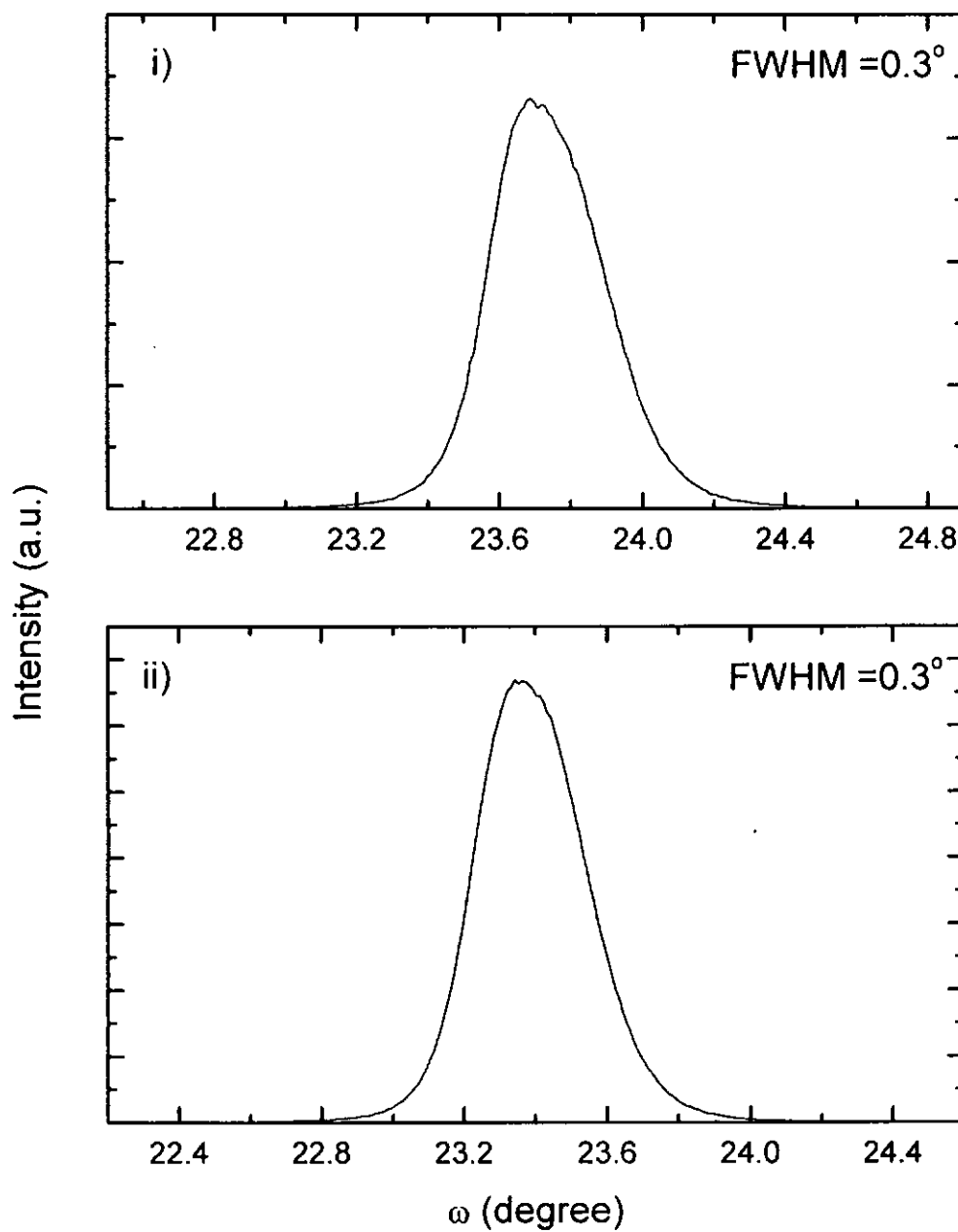


Fig. 4.13 Rocking curves of i) $\text{La}_{0.7}\text{Sr}_{0.3}\text{MnO}_3$ and ii) $\text{La}_{0.05}\text{Sr}_{0.95}\text{TiO}_3$ for the $\text{La}_{0.7}\text{Sr}_{0.3}\text{MnO}_3/\text{SrTiO}_3/\text{La}_{0.05}\text{Sr}_{0.95}\text{TiO}_3$ junction

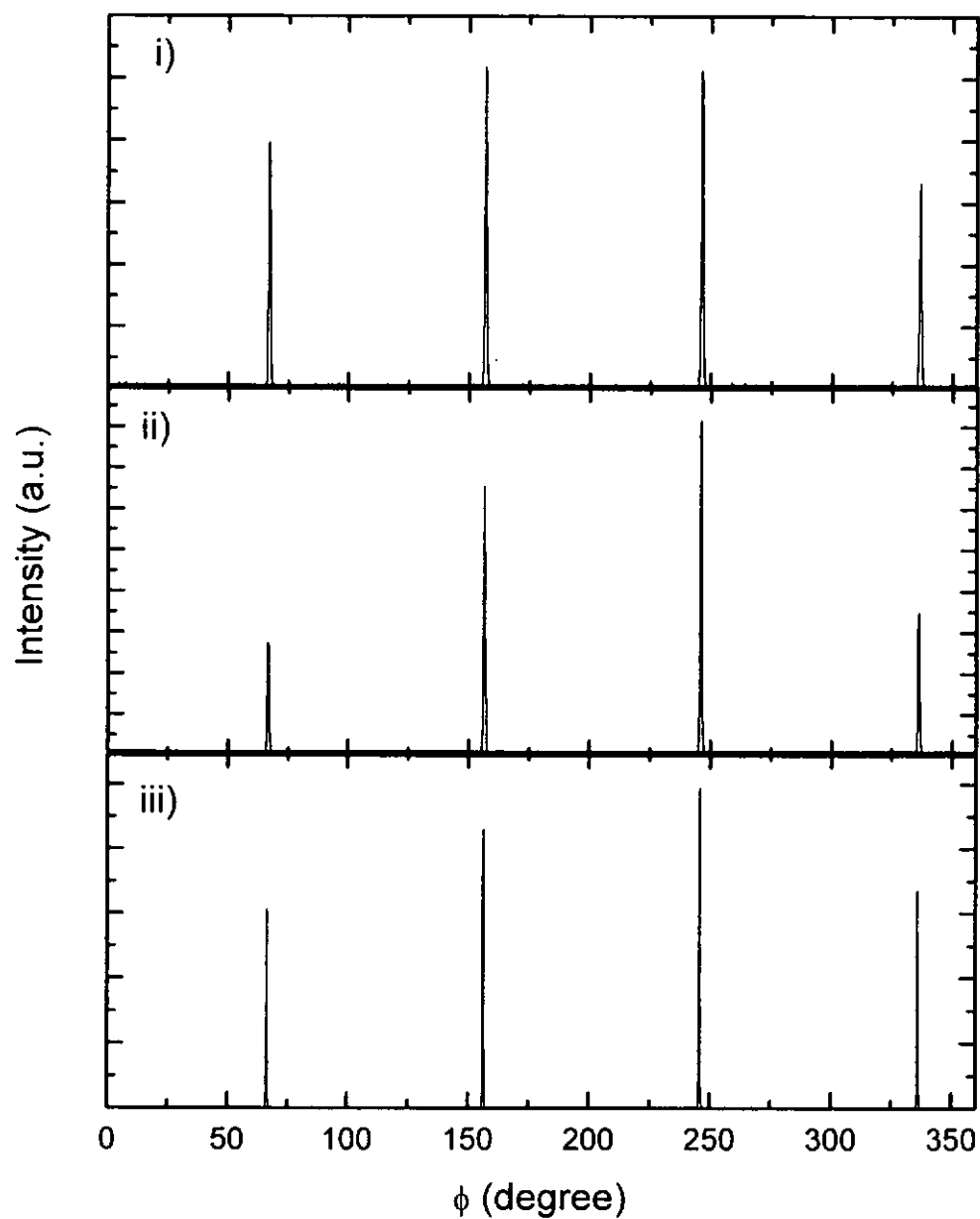


Fig. 4.14 XRD ϕ -scan of the i) $\langle 202 \rangle \text{La}_{0.7}\text{Sr}_{0.3}\text{MnO}_3$, ii) $\langle 202 \rangle \text{La}_{0.05}\text{Sr}_{0.95}\text{TiO}_3$ and iii) $\langle 202 \rangle \text{LAO}$ for the $\text{La}_{0.7}\text{Sr}_{0.3}\text{MnO}_3/\text{SrTiO}_3/\text{La}_{0.05}\text{Sr}_{0.95}\text{TiO}_3$ junction



4.4 Electrical properties of the p - $\text{La}_{1-x}\text{Sr}_x\text{MnO}_3/i$ - SrTiO_3 n - $\text{La}_{1-y}\text{Sr}_y\text{TiO}_3$ tri-layer junctions

$\text{La}_{1-x}\text{Sr}_x\text{MnO}_3$ and $\text{La}_{1-y}\text{Sr}_y\text{TiO}_3$ are known to be conducting/semiconducting oxides. Their electrical transport properties depend on their exact composition. Both the $\text{La}_{1-x}\text{Sr}_x\text{MnO}_3$ and $\text{La}_{1-y}\text{Sr}_y\text{TiO}_3$ thin films in this study have been fabricated from their corresponding bulk ceramic targets of the desired compositions. The resistivity against temperature (R-T) relations of the as-prepared single layer oxide films have been measured at temperature from 300 – 500K. The R-T relation not only displays the temperature dependence of the absolute resistivity but also yields useful information on the conduction mechanism (such as the metallic-like conduction or the semiconducting-like conduction).

4.4.1 Electrical properties of $\text{La}_{1-x}\text{Sr}_x\text{MnO}_3$ thin films

Two discrete LSMO targets, $\text{La}_{0.85}\text{Sr}_{0.15}\text{MnO}_3$ and $\text{La}_{0.7}\text{Sr}_{0.3}\text{MnO}_3$, were fabricated as mention in section 4.2.1. Bulk $\text{La}_{0.85}\text{Sr}_{0.15}\text{MnO}_3$ is semiconducting-like at room temperature. On the other hand bulk $\text{La}_{0.7}\text{Sr}_{0.3}\text{MnO}_3$ is metallic-like. A simple two point probe was used for the R-T measurement for these two LSMO films grown under the same substrate temperature of 650°C and ambient pressure of 100mTorr. The R-T relations shown in Fig. 4.15 reveal dissimilar properties. The first difference is the absolute resistivity. The $\text{La}_{0.85}\text{Sr}_{0.15}\text{MnO}_3$ films exhibits resistivity of some six orders of magnitude higher than that of $\text{La}_{0.7}\text{Sr}_{0.3}\text{MnO}_3$ film. It is the result of



higher strontium doping level in $\text{La}_{0.7}\text{Sr}_{0.3}\text{MnO}_3$. The higher the doping concentration, the more the charge carriers are induced. The second difference is the clear transition observed in the R-T profile of $\text{La}_{0.7}\text{Sr}_{0.3}\text{MnO}_3$ – a transition from metallic-like to semiconducting-like. As LSMO is a well known ferromagnetic material, it has a phase transition at around room temperature. The measured Curie temperature of the $\text{La}_{0.7}\text{Sr}_{0.3}\text{MnO}_3$ film is 290K as marked by arrow in Fig. 4.15. It means that the $\text{La}_{0.7}\text{Sr}_{0.3}\text{MnO}_3$ film could be metallic-like or semiconducting-like conducting in according to the ambient temperature. In fact, the phase transition temperature of LSMO depends on the composition. For example, $\text{La}_{0.85}\text{Sr}_{0.15}\text{MnO}_3$ shows no transition within 78K and 400K. Fig. 4.15 shows that its resistivity decreases monotonously as the temperature is increased, indicating the semiconducting-like electrical transportation. It is believed that its transition temperature exists at a much lower temperature than 78K. Indeed the electrical transport properties are so much different in $\text{La}_{0.7}\text{Sr}_{0.3}\text{MnO}_3$ and in $\text{La}_{0.85}\text{Sr}_{0.15}\text{MnO}_3$ that a p-i-n junction formed by matching these two p-type manganates with n-type oxide may lead to quite different properties, some of which are studied in later sections.

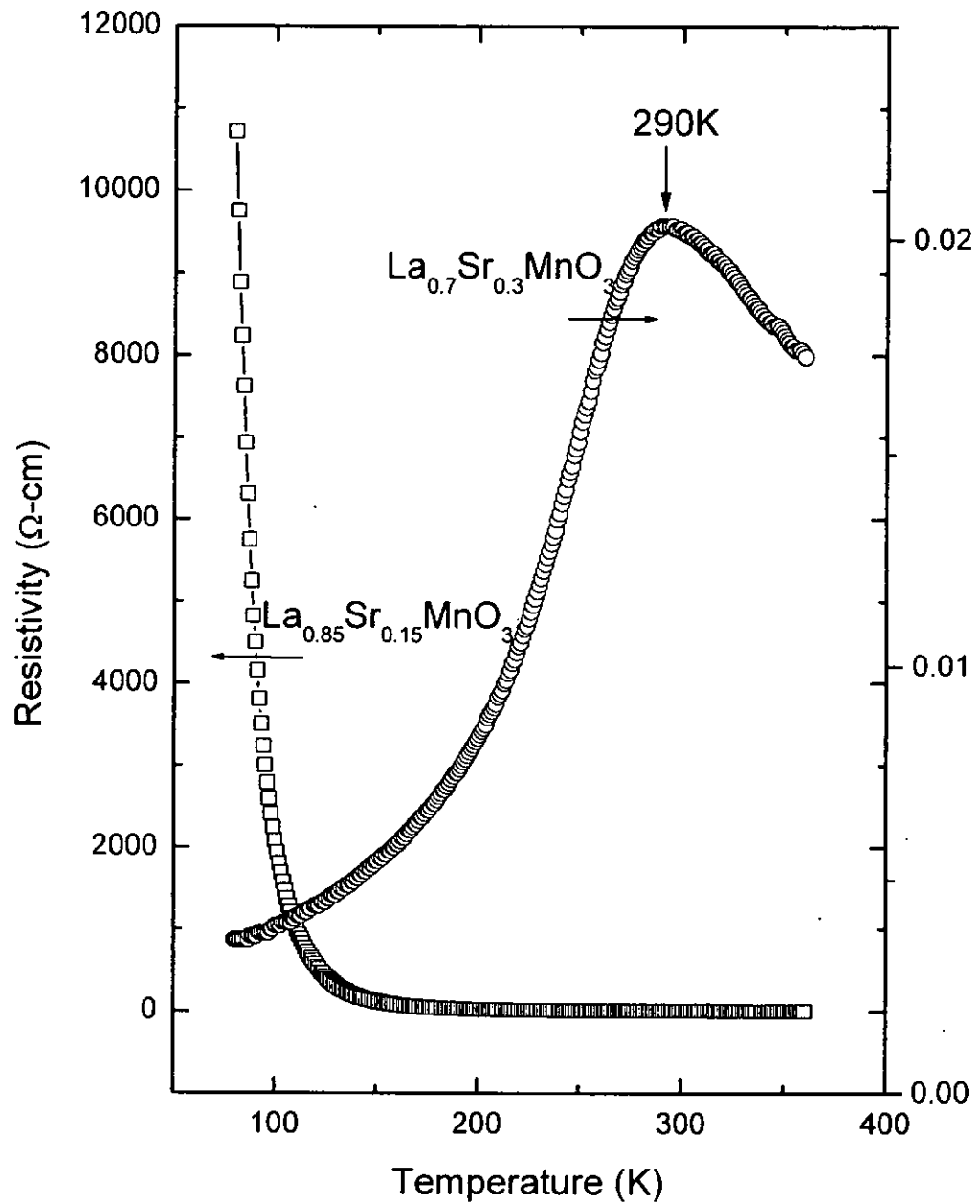


Fig. 4.15 Resistivity against temperature relations of LSMO films grown with different target compositions, $\text{La}_{0.7}\text{Sr}_{0.3}\text{MnO}_3$ (\circ) and $\text{La}_{0.85}\text{Sr}_{0.15}\text{MnO}_3$ (\square)



4.4.2 Electrical properties of $\text{La}_{1-y}\text{Sr}_y\text{TiO}_3$ thin films

STO is an insulator. By proper doping of La, however, a highly electrical conducting oxide could be formed. For example, $\text{La}_{0.5}\text{Sr}_{0.5}\text{TiO}_3$ thin film shows metallic transport behavior at 20 - 300K and an extremely low resistivity of $64\mu\Omega\text{cm}$ at room temperature [Wu et. al. 2000]. La-doped STO displays n-type transport behavior at room temperature. Although $\text{La}_{0.5}\text{Sr}_{0.5}\text{TiO}_3$ film possesses the highest conductivity among the $\text{La}_{1-y}\text{Sr}_y\text{TiO}_3$ series, it nevertheless does not match those of manganates, i.e. $\text{m}\Omega\text{-cm}$. In this study, the discrete $\text{La}_{0.05}\text{Sr}_{0.95}\text{TiO}_3$, $\text{La}_{0.1}\text{Sr}_{0.9}\text{TiO}_3$ and $\text{La}_{0.15}\text{Sr}_{0.85}\text{TiO}_3$ targets were fabricated by the standard solid state reaction. The absolute resistivities of LSTO thin films with different compositions were measured. It is seen in Fig. 4.16 i) that the higher the doping levels of lanthanum, the lower the resistivity of the films. Within the composition range studied, the lowest resistivity is $0.006\Omega\text{-cm}$ and the highest is $0.015\Omega\text{-cm}$ at room temperature.

Fig. 4.16 i) shows the $R\text{-}T^2$ relation of the LSTO thin films in the temperature range from 300K to 500K. The resistivity increases with temperature, suggesting a metallic-like conduction mechanism. It is reported that the resistivity is linearly proportion to the square of temperature in Kelvin [Tokura et. al. 1993]. Unfortunately no obvious linear relations are shown in the $R\text{-}T^2$ plots of these LSTO films. In fact, a linear relation is obtained in $R\text{-}T^4$ relation as shown in Fig. 4.16 ii). Till now all the LSTO film are confirmed with a metallic conduction mechanism under the temperature range from 300K to 500K. And so for all the fabricated p-i-n⁺ junctions consist of heavily doped



n-type conducting oxide layer, the junctions should be classified as p-i-n⁺.

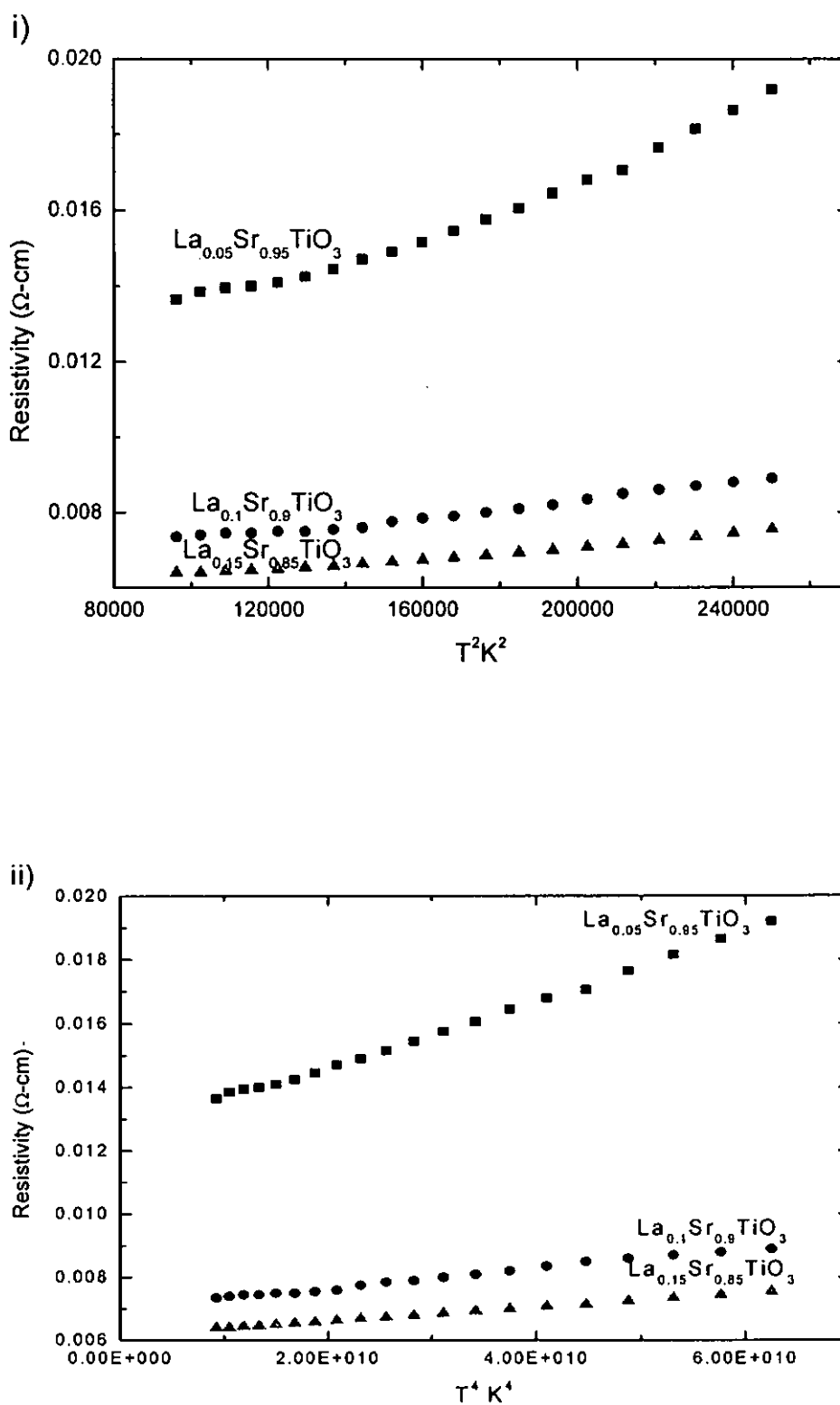


Fig. 4.16 The resistivity against temperature profile of the LSTO thin films i) ρ vs T^2 ii) ρ vs T^4



4.4.3 I-V characteristics of p-La_{1-x}Sr_xMnO₃/i-SrTiO₃/ n-La_{1-y}Sr_yTiO₃ junctions at room temperature

In 1999, Suguria and his co-worker fabricated the first p-La_{0.85}Sr_{0.15}MnO₃/i-SrTiO₃/n-La_{0.05}Sr_{0.95}TiO₃ [1999] junction. Moreover they fixed the composition of both LSMO and LSTO and focused on investigating the influence of STO thickness on the I-V characteristics. In this study, we are interested in the effect of dopant concentration of both LSMO and LSTO layers on the I-V characteristics. As reported in section 4.4.1 and section 4.4.2, a little change in doping concentration could induce a large change in resistivity. It is interested to see how the absolute resistivities of p-type and n-type oxide layers affect the I-V characteristics of the junction. Both La_{0.85}Sr_{0.15}MnO₃ and La_{0.05}Sr_{0.95}TiO₃ are semiconducting oxides. They are far from their highest conducting composition as reported by Suguria's paper [Suguria et. al. 1999]. According to the last section, all our LSTO films are metallic-like with high conductivity. It is totally different from the LSTO films used in Suguria's work, in which the grown La_{0.05}Sr_{0.95}TiO₃ film is semiconducting-liked. The dissimilar features of the two La_{0.05}Sr_{0.95}TiO₃ films may caused by the different PLD setup. Suguria has used the eclipse pulsed laser deposition method. In our approach, different composition LSMO and LSTO targets were made and hence different combinations of La_{1-x}Sr_xMnO₃/SrTiO₃/La_{1-y}Sr_yTiO₃ junction were fabricated. I-V characteristic of these junctions are presented in the following sections.



Prior to the fabrication of the tri-layer p-i-n junctions, the bi-layer $\text{La}_{0.85}\text{Sr}_{0.15}\text{MnO}_3/\text{La}_{0.05}\text{Sr}_{0.95}\text{TiO}_3$ junctions were prepared. All the layers were grown under the same deposition condition as mention in Section 4.3.1.

In all the oxide layer or junction electrical measurements we will use Pt as the conducting buffer to the external circuits. For this reason the I-V characteristics of the two junctions, Pt/LSMO and Pt/LSTO, have been measured and are shown in Fig. 4.17. Linear relationships traversing the origin indicate good ohmic contact in these junctions. The rectifying effect from any subsequent I-V characteristic curve comes from the contribution of the oxide-oxide junction only and not from the Pt-oxide junction.

Fig. 4.18 shows the I-V characteristics of the $\text{La}_{0.85}\text{Sr}_{0.15}\text{MnO}_3/\text{La}_{0.05}\text{Sr}_{0.95}\text{TiO}_3$ junction. It is a linear line traversing the origin. No rectifying property is observed. This is the same as reported by Suguria [1999]. It is argued that the created depletion layer at the junction is very narrow, and hence the tunneling leakage current is too large. The minority charge carrier could tunnel through the depletion layer easily under reverse biased condition. In order to remedy this large leakage current a STO insulating layer is sandwiched in between the LSMO and LSTO layers. It is aimed at broadening the transition region and hence lowering the transmission probability. However, the forward biased diffusion current will also be reduced by the insertion of such an insulator.

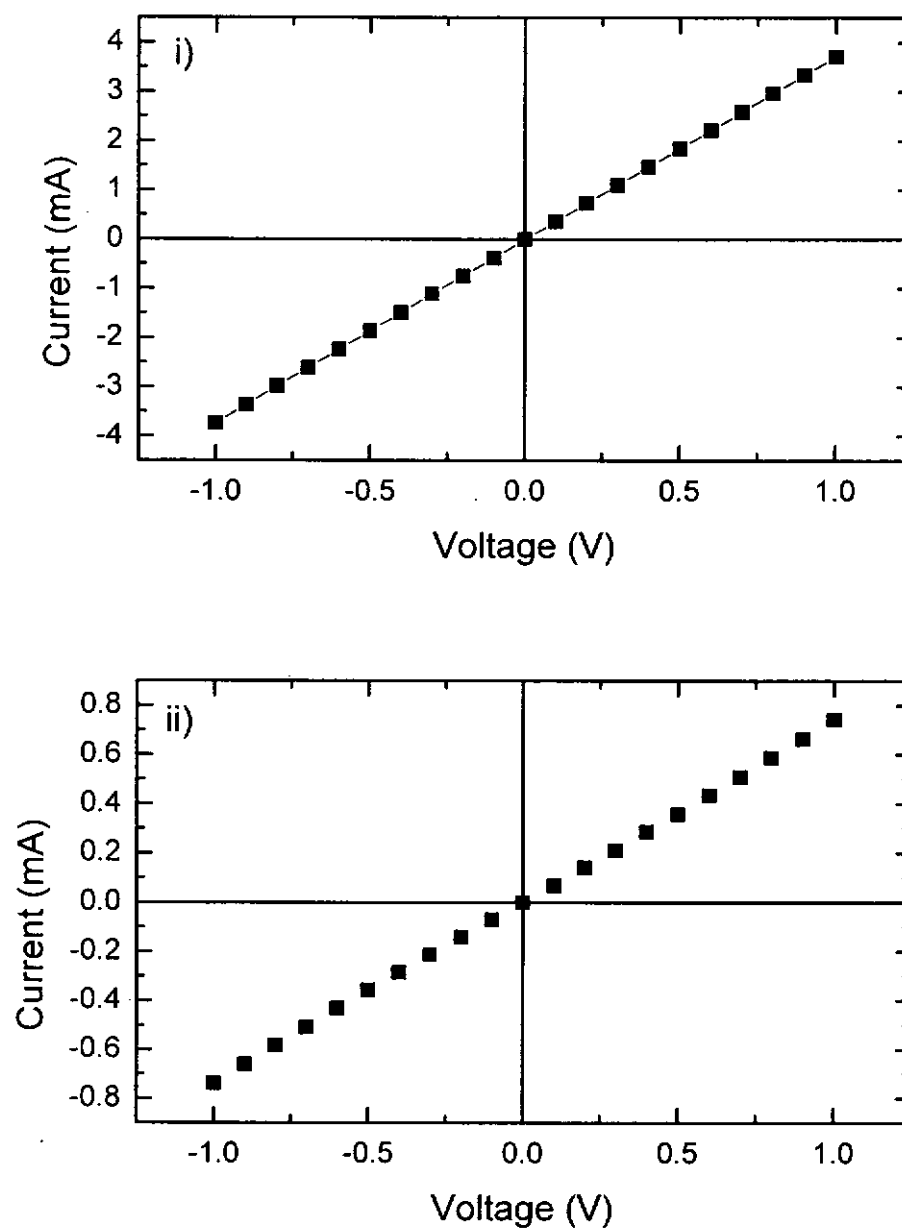


Fig. 4.17 I-V characteristics of i) Pt/LSMO/Pt and ii) Pt/LSTO/Pt

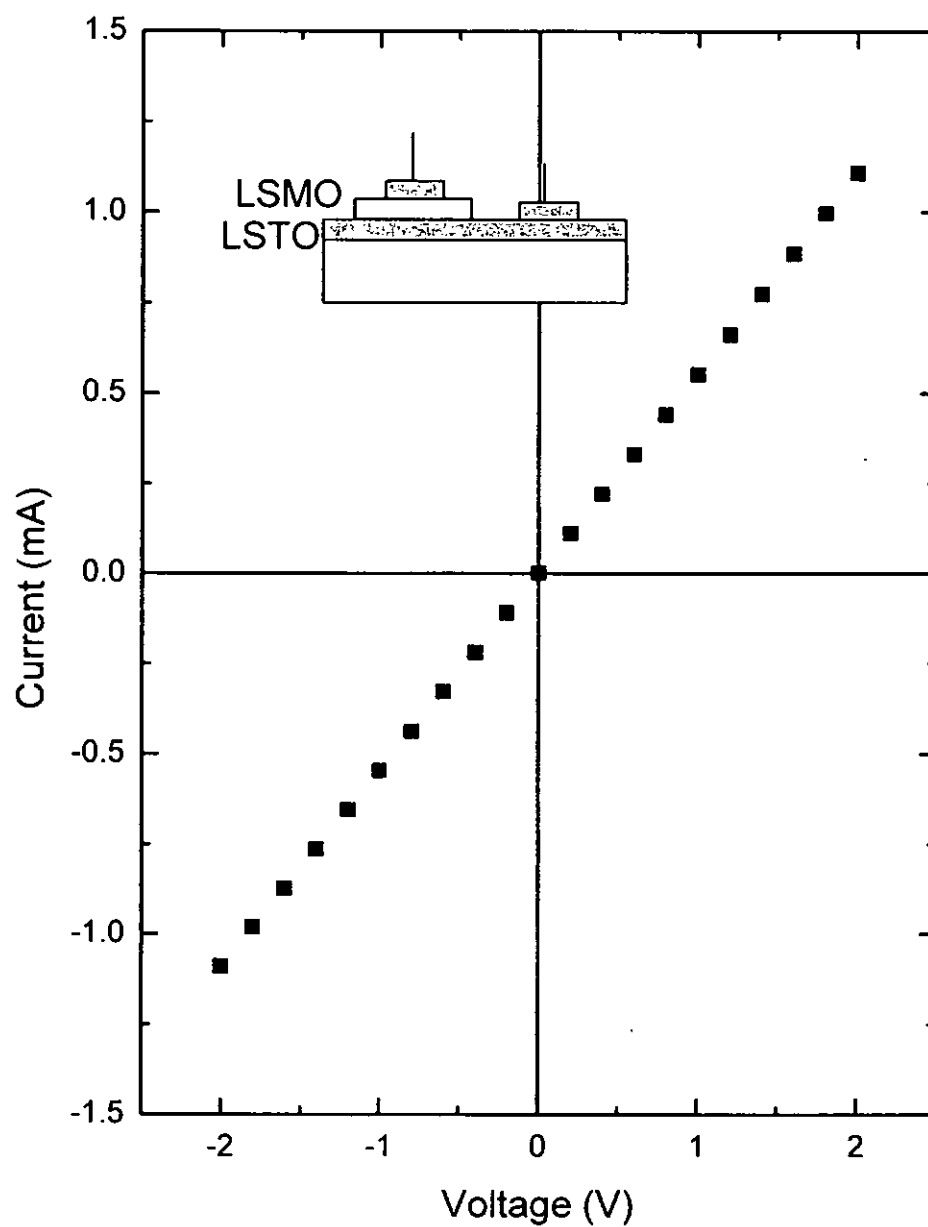


Fig. 4.18 I-V characteristics of $\text{La}_{0.85}\text{Sr}_{0.15}\text{MnO}_3/\text{La}_{0.05}\text{Sr}_{0.95}\text{TiO}_3$ junction with platinum electrodes



The LSMO/LSTO junction exhibits ohmic I-V characteristics denoting no rectifying effect in the bi-layer junction. In this section the tri-layer $\text{La}_{1-x}\text{Sr}_x\text{MnO}_3/\text{SrTiO}_3/\text{La}_{1-y}\text{Sr}_y\text{TiO}_3$ p-i-n⁺ junctions showing good rectifying property are described. We have mainly focused on two heterostructures: $\text{La}_{0.85}\text{Sr}_{0.15}\text{MnO}_3/\text{SrTiO}_3/\text{La}_{0.05}\text{Sr}_{0.95}\text{TiO}_3$ and $\text{La}_{0.7}\text{Sr}_{0.3}\text{MnO}_3/\text{SrTiO}_3/\text{La}_{0.05}\text{Sr}_{0.95}\text{TiO}_3$. In section 4.4.1, the two LSMO films showed a large dissimilarity in the R-T relation. Therefore we have fabricated the $\text{La}_{0.85}\text{Sr}_{0.15}\text{MnO}_3$ and $\text{La}_{0.7}\text{Sr}_{0.3}\text{MnO}_3$ based p-i-n⁺ junctions, in order to investigate the effect of the absolute resistivity on the junction performance. In this respect, $\text{La}_{0.05}\text{Sr}_{0.95}\text{TiO}_3$ is selected as the n-layer material. Temperature dependent I-V characteristics for these two junctions have been measured too. It is observed that the influence of temperature on the junction is not the same for these two junctions. We will discuss them in more details in later paragraphs. The performances of p-i-n⁺ junctions comprising LSMO and LSTO layers of different composition are compared.

The I-V characteristic of the $\text{La}_{0.85}\text{Sr}_{0.15}\text{MnO}_3/\text{SrTiO}_3/\text{La}_{0.05}\text{Sr}_{0.95}\text{TiO}_3$ heterostructure is shown in Fig. 4.19. A typical diode rectifying profile is obtained. Although the fabrication condition of these junctions is different from that used by Suguria [1999], the junction rectifying properties are similar. It is noted that the junction resistance of our samples is one order of magnitude lower than the one fabricated by Suguria et. al.. The turn-on voltage of our junctions, however, is a bit higher. In the forward biased region, the turn-on voltage of our p-i-n junction is 1V. The insertion of the STO layer forbids the tunneling current. It nevertheless increases the turn-on voltage, as it gives an



extra diffusion barrier for the majority charge carrier. No sudden surge of leakage current is observed. In fact the leakage current increases slowly with the reverse bias voltage and breakdown does not occur at bias of $<-5V$. The gradual increase of leakage current is caused by the tunneling current, which is in the form of $I = A_1 V \exp(1 - V / A_2)$ [Sugiura et.al.1999].

Fig. 4.19 shows not only the I-V characteristic of one p-i-n⁺ junction, but four p-i-n⁺ junctions with different conducting path distance along the LSTO film, constituting different series resistance in the measuring circuit. The turn-on voltage of these junctions appears more or less the same at around 1.2V; the slight difference may simply due to the non-uniformity of the grown STO film. The thicker the STO layer, the lower the internal electric field is induced at the same biased voltage and hence differs in the turn-on voltage. Excluding the dissimilarity in turn-on voltage, another notable feature is the large difference on the slope of the linear dependent region in the I-V characteristic. The unequal series resistance of the oxide layer in the p-i-n⁺ junction is held responsible. According to the p-i-n⁺ junction arrangement, the LSTO film contributes a larger series resistance than the LSMO film. Although all the measuring junctions are in the same sample, every junction has their own LSTO series resistances due to the varying measurement distance (defined in Fig. 4.3). The series resistances would introduce a sufficiently large influence on the slope in the linear I-V region. A small series resistance causes a steep slope. So that the slope of the linear region decreases as the measuring distance increases. Our results indicate that the steepness of the slope is primarily due to the conducting path length in LSTO only, and hence the LSMO layer



contributes little to the series resistance. Our conclusion here is in contrast with those of Suguria's work. As the junction and the LSTO layer resistances in Suguria's work are several $M\Omega$ and several Ω respectively, the change in LSTO resistance bears little effect on the magnitude of the junction current. On the other hand, our junction resistance is just one order of magnitude higher than the LSTO layer resistance. The change in LSTO resistance could therefore give a marked effect on the series resistance of the junction. This has in fact been indirectly verified by the I-V profiles shown in Fig. 4.19. Each I-V curve is measured from p-n junction at different location. The systematic change of I-V gradient at forward bias voltage with d values (equivalent to LSTO resistance) confirms the effect due to LSTO layer resistance.

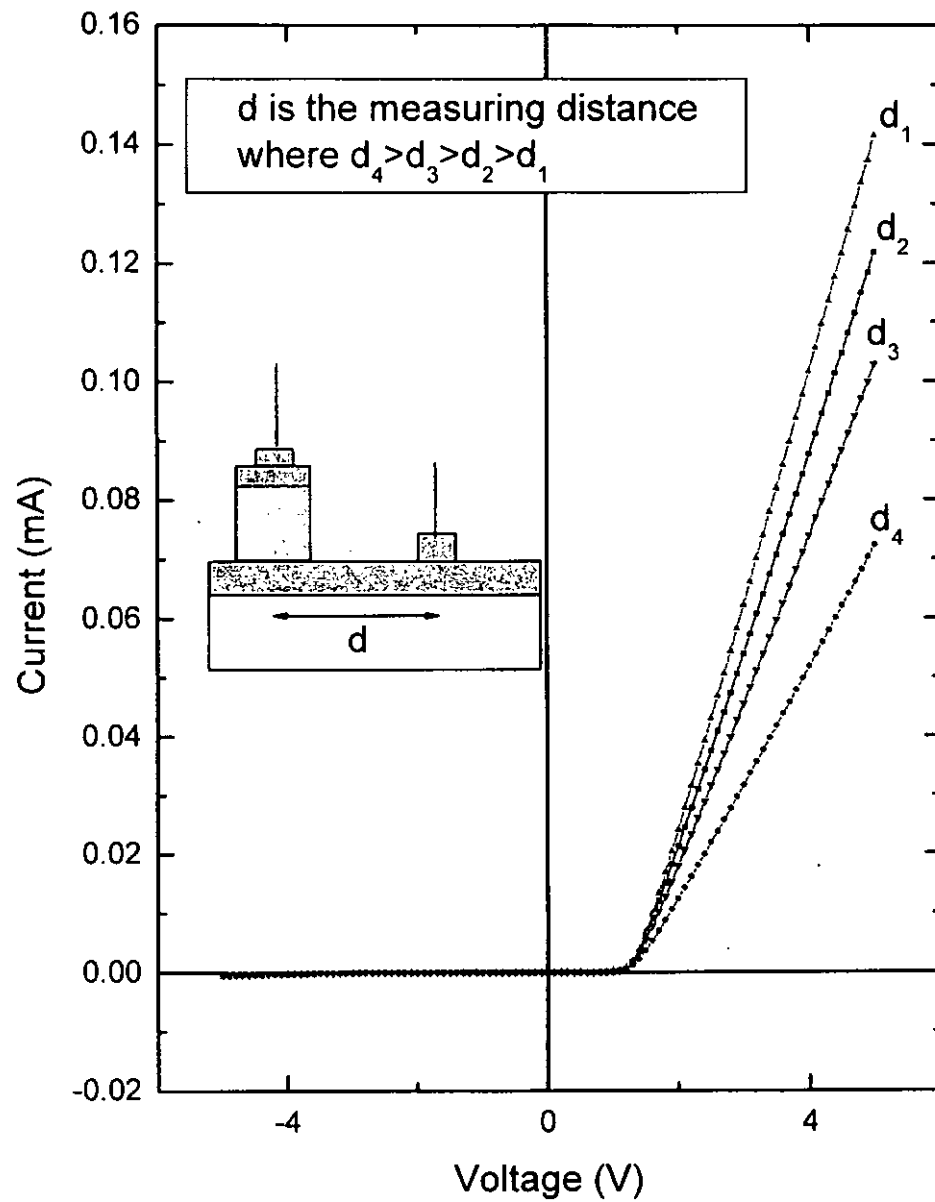


Fig. 4.19 I-V characteristics of $\text{La}_{0.85}\text{Sr}_{0.15}\text{MnO}_3/\text{SrTiO}_3/\text{La}_{0.05}\text{Sr}_{0.95}\text{TiO}_3$ p-i-n⁺ junctions on the same sample



I-V characteristics of these two LSMO/SrTiO₃/La_{0.05}Sr_{0.95}TiO₃ junctions are plotted on Fig. 4.20. These two junctions are grown under the same deposition condition except for using different of LSMO targets. The La_{0.85}Sr_{0.15}MnO₃/SrTiO₃/La_{0.05}Sr_{0.95}TiO₃ junction shows a turn-on voltage of 1V while the La_{0.7}Sr_{0.3}MnO₃/SrTiO₃/La_{0.05}Sr_{0.95}TiO₃ junction has a turn-on voltage of 0.9V.

The absolute forward biased current of the La_{0.7}Sr_{0.3}MnO₃/SrTiO₃/La_{0.05}Sr_{0.95}TiO₃ junction is much higher than those obtained in the La_{0.85}Sr_{0.15}MnO₃/SrTiO₃/La_{0.05}Sr_{0.95}TiO₃ junction. Moreover the slopes of the linear regions for these two junctions are not the same. La_{0.7}Sr_{0.3}MnO₃/SrTiO₃/La_{0.05}Sr_{0.95}TiO₃ gives a much steeper slope than La_{0.85}Sr_{0.15}MnO₃/SrTiO₃/La_{0.05}Sr_{0.95}TiO₃. This is the result of the higher resistivity of the La_{0.85}Sr_{0.15}MnO₃/SrTiO₃/La_{0.05}Sr_{0.95}TiO₃ junction. For the same reason La_{0.85}Sr_{0.15}MnO₃/SrTiO₃/La_{0.05}Sr_{0.95}TiO₃ exhibits a smaller current than La_{0.7}Sr_{0.3}MnO₃/SrTiO₃/La_{0.05}Sr_{0.95}TiO₃. Naturally its reverse bias leakage current is also smaller. The current of the La_{0.7}Sr_{0.3}MnO₃/SrTiO₃/La_{0.05}Sr_{0.95}TiO₃ junction starts an evident negative drop at -2V. The La_{0.85}Sr_{0.15}MnO₃/SrTiO₃/La_{0.05}Sr_{0.95}TiO₃ junction shows no sign of such a current drop at -5V. It is known that La_{0.7}Sr_{0.3}MnO₃ is more conductive than La_{0.85}Sr_{0.15}MnO₃. That means it possesses more mobile charge carrier. Consequently it provides higher forward biased current as well as higher leakage current.

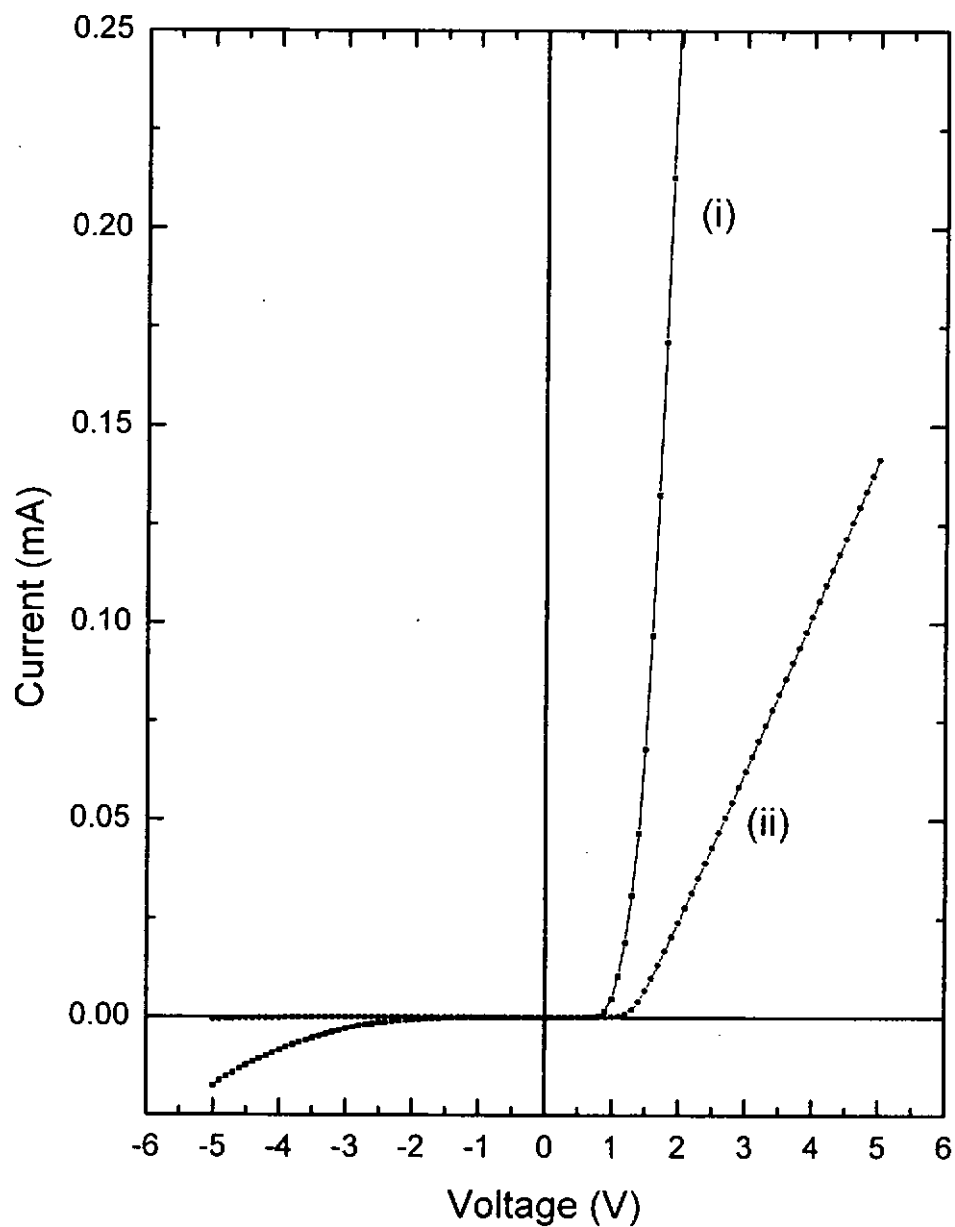


Fig. 4.20 I-V characteristics of (i) $\text{La}_{0.7}\text{Sr}_{0.3}\text{MnO}_3/\text{SrTiO}_3/\text{La}_{0.05}\text{Sr}_{0.95}\text{TiO}_3$ and (ii) $\text{La}_{0.85}\text{Sr}_{0.15}\text{MnO}_3/\text{SrTiO}_3/\text{La}_{0.05}\text{Sr}_{0.95}\text{TiO}_3$



Aside from the above two p-i-n⁺ junctions, three more have been fabricated. This time the p-layer is fixed with $\text{La}_{0.7}\text{Sr}_{0.3}\text{MnO}_3$. Three n-layers, $\text{La}_{0.05}\text{Sr}_{0.95}\text{TiO}_3$, $\text{La}_{0.1}\text{Sr}_{0.9}\text{TiO}_3$ and $\text{La}_{0.15}\text{Sr}_{0.85}\text{TiO}_3$ are selected for these three junctions. The three LSTO films are different in resistivity, so that a variation of resistivity and the junction characteristics could be related. Fig. 4.21 displays the I-V profiles of these three p-i-n⁺ junctions. It is observed that the overall resistivity decreases with the increase of lanthanum doping in the LSTO film. Doping of lanthanum introduces more charge carrier, and hence increases the conductivity of the LSTO films. The decrease in slope from $\text{La}_{0.7}\text{Sr}_{0.3}\text{MnO}_3/\text{SrTiO}_3/\text{La}_{0.15}\text{Sr}_{0.85}\text{TiO}_3$ to $\text{La}_{0.7}\text{Sr}_{0.3}\text{MnO}_3/\text{SrTiO}_3/\text{La}_{0.05}\text{Sr}_{0.95}\text{TiO}_3$ also suggests the fact that the $\text{La}_{0.7}\text{Sr}_{0.3}\text{MnO}_3/\text{SrTiO}_3/\text{La}_{0.05}\text{Sr}_{0.95}\text{TiO}_3$ possesses the largest series resistance.

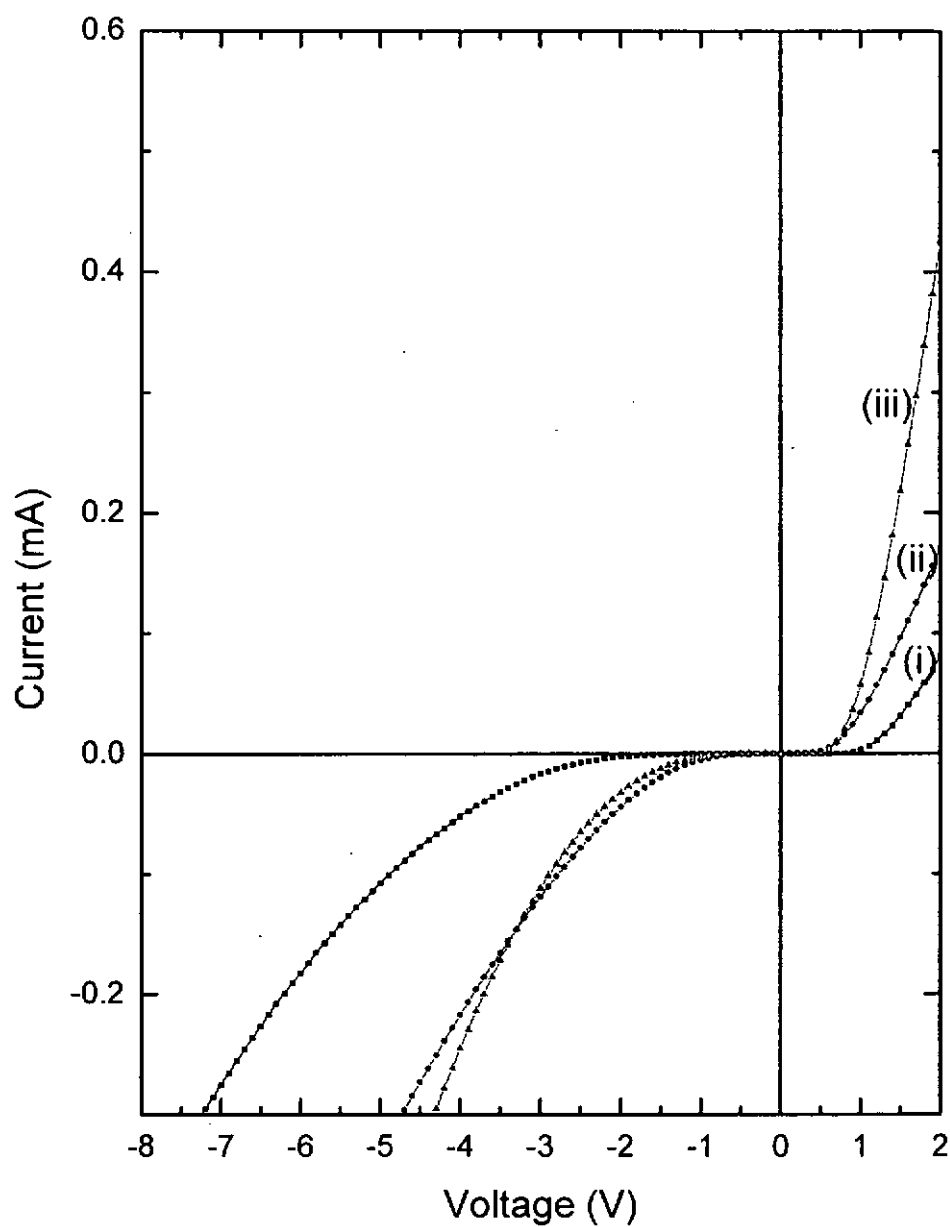


Fig. 4.21 I-V characteristics of (i) $\text{La}_{0.7}\text{Sr}_{0.3}\text{MnO}_3/\text{SrTiO}_3/\text{La}_{0.05}\text{Sr}_{0.95}\text{TiO}_3$ and (ii) $\text{La}_{0.7}\text{Sr}_{0.3}\text{MnO}_3/\text{SrTiO}_3/\text{La}_{0.1}\text{Sr}_{0.9}\text{TiO}_3$ and (iii) $\text{La}_{0.7}\text{Sr}_{0.3}\text{MnO}_3/\text{SrTiO}_3/\text{La}_{0.15}\text{Sr}_{0.85}\text{TiO}_3$



4.4.4 The influence of temperature on the properties of the $\text{La}_{1-x}\text{Sr}_x\text{MnO}_3/\text{SrTiO}_3/\text{La}_{1-y}\text{Sr}_y\text{TiO}_3$ junction

High temperature operation is one of the goals of all-oxide p-n junction research. Here we investigate how the temperature influences the performance of the junction. The temperature of interest ranges from 300K to 500K. Fig. 4.22 displays the I-V characteristic of the $\text{La}_{0.85}\text{Sr}_{0.15}\text{MnO}_3/\text{SrTiO}_3/\text{La}_{0.05}\text{Sr}_{0.95}\text{TiO}_3$ junction under various temperatures. It is observed that the turn-on voltage decreases as the temperature is increased. This is just the same as the conventional semiconductor p-n junction. It is believed that a higher thermal energy of the majority carrier helps to activate the carriers to diffuse through the depletion layer. Apart from lowering the turn-on voltage, leakage current increases at high temperature too. According to the thermal effect, it is expected that the leakage current against temperature gives a “ $I_s \propto e^{-E_s/kT}$ ” relationship. Logarithmic plot of current against the inverse temperature is represented by linear straight line as shown in Fig. 4.23. Till now the temperature dependence of the tri-layer oxide p-i-n⁺ junction is similar to conventional semiconductor p-n junction. However, the change in slope in the linear region under various temperatures differs from conventional semiconductor junction. The slope decreases dramatically at first from 300K to 360K. Thereafter the slope increases again with temperature. Evidently there are two opposite mechanisms counter acting on each other during the temperature change; one mechanism will give rise the overall series resistance and the other lower the overall series resistance. It is believed that the LSTO contributes to the rise of series resistance. As mentioned in section 4.4.2, LSTO



is a metallic-like conducting material, its resistance increases with the temperature according to $R \propto T^4$. Due to the sample configuration (Fig. 4.3 i)), the junction resistance is in several tens of kilo-ohm and the resistance of LSTO is in kilo-ohm. The change in resistance on LSTO layer would therefore give a considerable effect on the junction characteristic. The drop in slope with the raised temperature is due to the increase of LSTO resistance. However the slope gradually increases again at high temperature. This is attributed to the increase of space-charge-limitation current via the trap defect, where the space-charge-limitation current increases exponentially with temperature $I_t \sim (V_2^2 / N_t) \exp(-E_t / kT)$ [Sugiura 1999], where N_t and E_t are the trap density and trap level respectively. Therefore with the increase of temperature, more current pass through the depletion layer and hence the series resistance decreases. The forward current should increase exponentially with temperature. It is well proved by the linear logarithmic plot of current with inverse temperature for this p-i-n⁺ junction, which is shown in Fig. 4.24. In general, the increase of resistivity of the LSTO layer would dominate under a relatively low temperature range. At higher temperatures the exponential increase of space-charge-limitation current dominates the change and hence the slope gets steeper with temperature.

The change in temperature has a pronounced effect on the junction performance. For forward biased condition, the diffusion current and recombination current are strongly affected by the operation temperature, having the diffusion current to recombination current ratio



of $\sim \exp\left[-\frac{E_g - qV}{2kT}\right]$. At a given forward biased condition, the diffusion

current will increase more rapidly than the recombination current. The logarithmic plot of current against voltage is replotted in the inset of Fig. 4.22. At temperatures below 320K, both the recombination current and diffusion current are seen in the graph. However for temperature up to and above 360K, the recombination current characteristic disappears. It is a good indication that diffusion current predominates at or above 360K for this p-i-n⁺ junction.

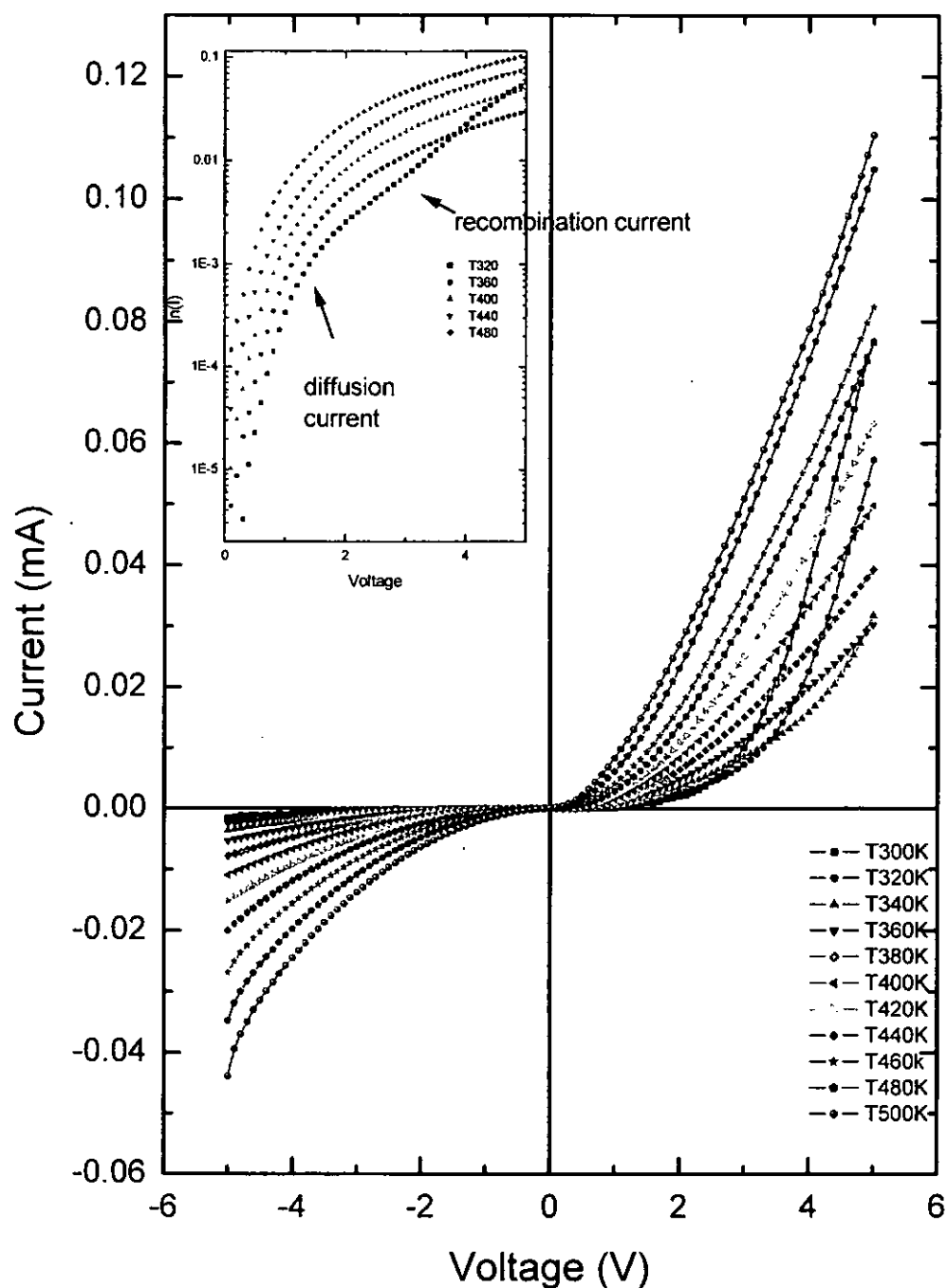


Fig. 4.22 Temperature dependence of the I-V characteristics of $\text{La}_{0.85}\text{Sr}_{0.15}\text{MnO}_3/\text{SrTiO}_3/\text{La}_{0.05}\text{Sr}_{0.95}\text{TiO}_3$ junction, the inset shows the logarithmic current against temperature graph

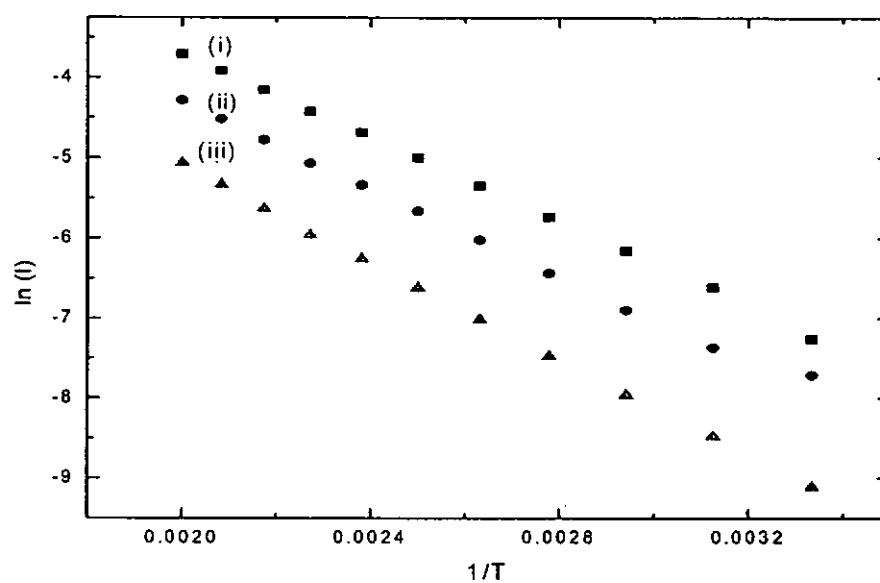


Fig. 4.23 Current vs temperature relationship at (i) -2V, (ii) -3V and (iii) -4V deduced from Fig. 4.22

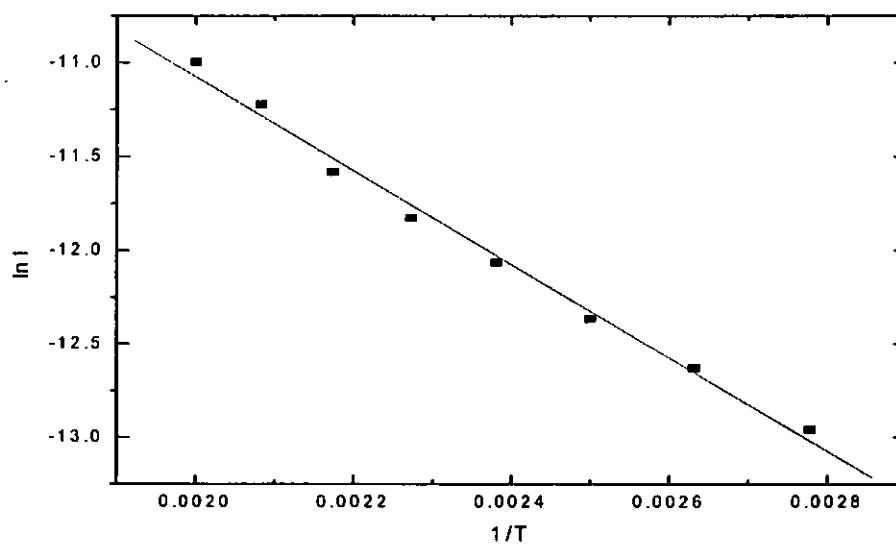


Fig. 4.24 Current vs temperature relationship at 1.5V deduced from Fig. 4.22



The temperature dependence of the I-V curve of $\text{La}_{0.7}\text{Sr}_{0.3}\text{MnO}_3/\text{SrTiO}_3/\text{La}_{0.05}\text{Sr}_{0.95}\text{TiO}_3$ junction (Fig. 4.25) exhibits a totally different feature to that of $\text{La}_{0.85}\text{Sr}_{0.15}\text{MnO}_3/\text{SrTiO}_3/\text{La}_{0.05}\text{Sr}_{0.95}\text{TiO}_3$. The slope of the linear region decreases as the temperature is increased. For $\text{La}_{0.7}\text{Sr}_{0.3}\text{MnO}_3/\text{SrTiO}_3/\text{La}_{0.05}\text{Sr}_{0.95}\text{TiO}_3$, the junction resistance is in several Kilo-ohm and LSTO resistance is in Kilo-ohm. This time the change in LSTO resistance with temperature can have a pronounced effect on the I-V characteristic. For the change in LSMO layer resistance, it is less pronounced due to the heterostructure configuration, so that the variation of LSMO resistance does not contribute much to the junction performance. The influence of temperature on the junction performance is dominated by the change in LSTO resistance only. LSTO resistance is metallic-like and increases with temperature. It is reasonable to expect a decrease of slope with temperature. However it is not clear that the space-charge limitation current effect is less important in this junction. The inset of Fig. 4.25 shows diffusion and recombination current on the $\ln(I) - V$ curve. At the temperature of 478K, diffusion current predominate the forward biased current.

Apart from the change in I-V slope, the temperature dependent performance of the $\text{La}_{0.7}\text{Sr}_{0.3}\text{MnO}_3/\text{SrTiO}_3/\text{La}_{0.05}\text{Sr}_{0.95}\text{TiO}_3$ junction is similar to that of $\text{La}_{0.85}\text{Sr}_{0.15}\text{MnO}_3/\text{SrTiO}_3/\text{La}_{0.05}\text{Sr}_{0.95}\text{TiO}_3$. The turn-on voltage of the junction evidently decreases as the temperature is increased. Also the leakage current has a relation of $I \propto \exp(-\frac{E_g}{kT})$. Fig. 4.26 gives the logarithmic plot of current against temperature relation. It is of no surprise that a linear straight line is found.

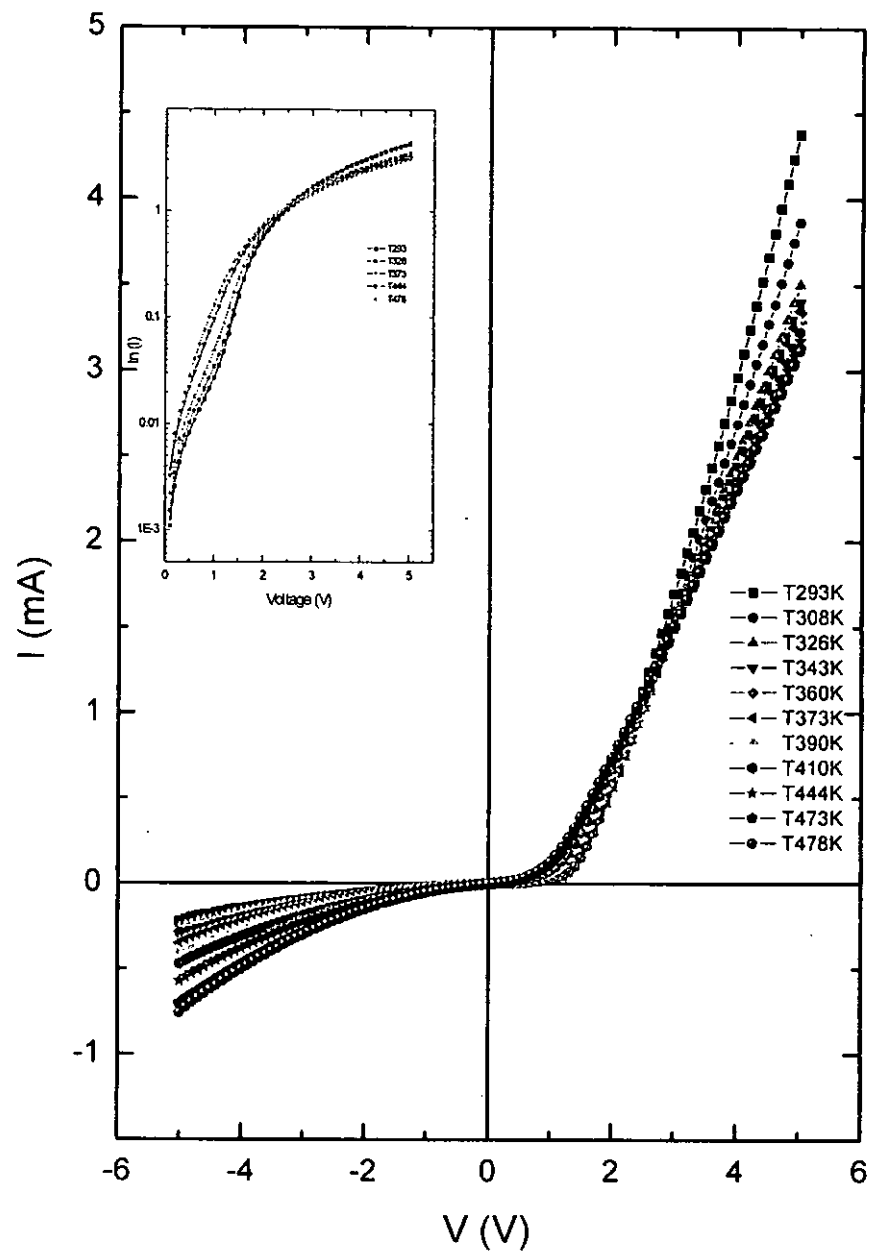


Fig. 4.25 Temperature dependence of the I-V characteristics of $\text{La}_{0.7}\text{Sr}_{0.3}\text{MnO}_3/\text{SrTiO}_3/\text{La}_{0.05}\text{Sr}_{0.95}\text{TiO}_3$ junction, the inset shows the logarithmic current against temperature graph

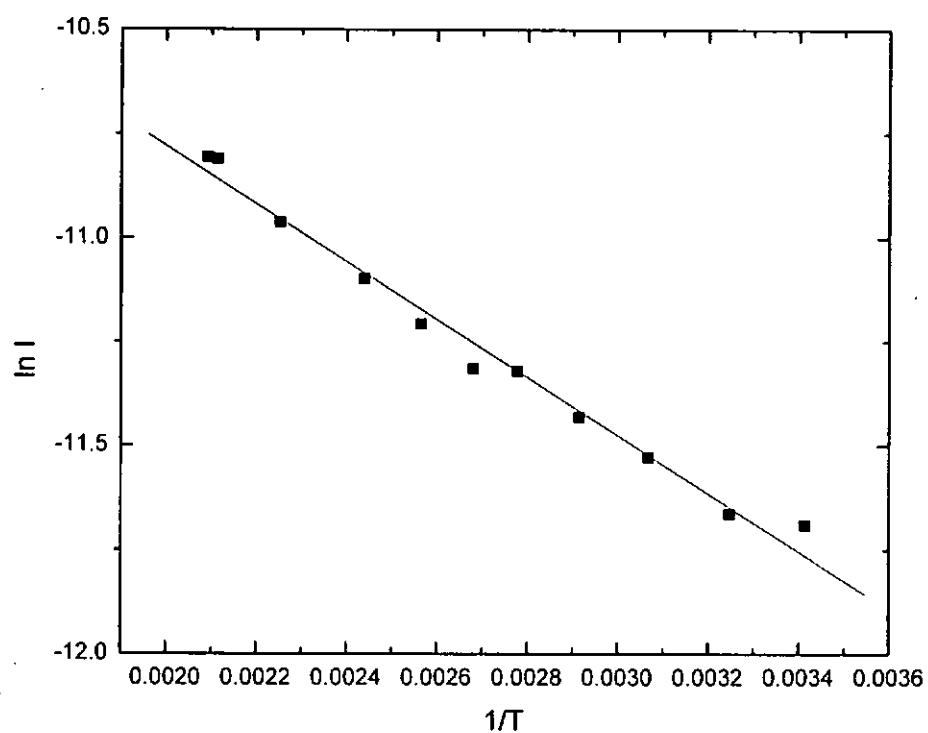


Fig. 4.26 Current vs temperature relationship at -0.5V deduced from Fig. 4.25



The $\text{p-La}_{1-x}\text{Sr}_x\text{MnO}_3/\text{i-SrTiO}_3/\text{n-La}_{0.05}\text{Sr}_{0.95}\text{TiO}_3$ junctions work properly up to a temperature of 500K. Leakage current increases with operation temperature according to $I_s \propto \exp\left(\frac{-E_g}{kT}\right)$. Therefore the turn-on voltage decreases with temperature just like the conventional semiconductor p-n junction. Moreover, it is discovered that the change of slope in the linear region is affected by two counteracting mechanisms. Higher temperature will increase the space-charge-limited current, meaning that more current flows through the junction. At the same time, resistance of LSTO (the bottom n-layer) increases with temperature, driving the slope of the linear region to decrease with temperature. Therefore the net change in slope is the combined effect of these two mechanisms.

In conclusion, epitaxial $\text{La}_{1-x}\text{Sr}_x\text{MnO}_3/\text{SrTiO}_3/\text{La}_{1-y}\text{Sr}_y\text{TiO}_3$ tri-layer p-i-n⁺ junctions have been produced with different composition of LSMO and LSTO films. Evidently, with the use of a higher resistivity LSMO or LSTO films, the absolute current under the same biased voltage is lowered. All the fabricated LSTO films are metallic-like in this work. Our successes in constructing the p-i-n⁺ junction point to the fact that highly conducting oxide layers can also be used for all-oxide junction production. Consequently choice of junction materials has increased.

Temperature dependence of the I-V characteristic reveals the influence of space-charge-limited current and LSTO layer resistance. The two counteracting effects control the slope in the linear I-V region. It leads to the different



variation on the slope for $\text{La}_{0.7}\text{Sr}_{0.3}\text{MnO}_3/\text{SrTiO}_3/\text{La}_{0.05}\text{Sr}_{0.95}\text{TiO}_3$ and $\text{La}_{0.85}\text{Sr}_{0.15}\text{MnO}_3/\text{SrTiO}_3/\text{La}_{0.05}\text{Sr}_{0.95}\text{TiO}_3$ as a function of temperature. The two junctions retain good rectifying properties at temperatures up to 500K. We have therefore demonstrated the high temperature operation of all-oxide p-i-n⁺ junction. In comparison, conventional semiconductor p-n junction operates stably at typical temperatures of up to 350K only.



Chapter 5

Fabrication and characterization of

$\text{La}_{0.7}\text{Sr}_{0.3}\text{MnO}_3/\text{Nb-1wt\% doped SrTiO}_3$

5.1 Introduction

Colossal magnetoresistance (CMR) effect has been observed in the family of manganese perovskite oxides [Sun et. al. 2004, Urushibara et. al. 1995]. LaMnO_3 is an antiferromagnetic insulator; however with the addition of divalent ions, p-type conducting oxide is formed. $\text{La}_{1-x}\text{A}_x\text{MnO}_3$ ($\text{A}=\text{Ca}, \text{Sr}, \text{Ba}, \text{etc}$) has a phase transformation at the Curie Temperature (T_c): ferromagnetic phase at low temperature ($T \leq T_c$), and paramagnetic phase at high temperature ($T \geq T_c$). In addition, it exhibits a strong negative magnetoresistance (MR) effect. Recently manganite based p-n junctions have also been fabricated [Tanaka et. al. 2002, Zhang et. al. 2002, Mitra et. al. 2001]. Sun et. al. [2004] studied the magnetic field dependent rectifying characteristic of $\text{La}_{0.32}\text{Pr}_{0.35}\text{Ca}_{0.33}\text{MnO}_3/\text{Nb-SrTiO}_3$ junction. They showed the band gap of $\text{La}_{0.32}\text{Pr}_{0.35}\text{Ca}_{0.33}\text{MnO}_3$ ($e_g \uparrow - e_g \downarrow$) varied with the magnetic state. The spin deviation of Mn^{4+} ions from fully ferromagnetic alignment caused a reduction of energy gap between e_g , and hence lowered the turn-on voltage of the junction.

In this study an all-oxide p-n junction has been made by growing an epitaxial $\text{La}_{0.7}\text{Sr}_{0.3}\text{MnO}_3$ thin film on single crystal substrate Nb-SrTiO₃ (NSTO).



$\text{La}_{0.7}\text{Sr}_{0.3}\text{MnO}_3$ appears to be more suitable for subsequent studies because of its well defined T_c and big change in electric transport property at around T_c . $\text{La}_{0.7}\text{Sr}_{0.3}\text{MnO}_3$ is metallic-like at low temperature ($T \leq T_c$) and semiconducting-like at high temperature ($T \geq T_c$) [Tanaka et. al. 2002]. With a well control of the deposition oxygen pressure, T_c of the films can be varied [Dho et. al. 2003]. It is reported that the MR effect is the highest at around T_c . In this work the deposition pressure has been purposely adjusted for T_c to occur at around room temperature and hence the effect of phase transition on the rectifying property can be investigated conveniently. Furthermore the temperature dependence of the junction performance has been analyzed. Some degradation processes on the junction characteristic have been identified. Due to the successful grown of p-i-n junction in the previous chapter, the insertion of STO has also been applied to solve some of the degradation problems.

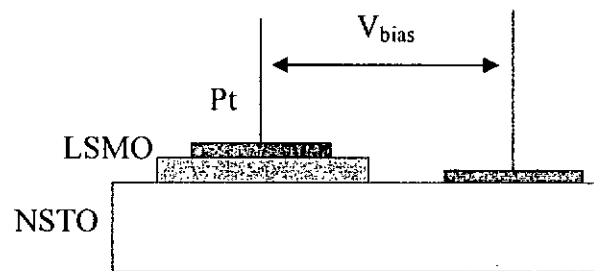
5.2 Structural characterization of $\text{La}_{0.7}\text{Sr}_{0.3}\text{MnO}_3/\text{NSTO}$ junction

5.2.1 Fabrication of $\text{La}_{0.7}\text{Sr}_{0.3}\text{MnO}_3/\text{NSTO}$ junction

Commercial NSTO single crystal substrate is a conducting n-type material. An all oxide p-n junction can be obtained by simply growing a p-type oxide layer on top of this substrate. We have prepared $\text{La}_{0.7}\text{Sr}_{0.3}\text{MnO}_3/\text{NSTO}$ junctions by depositing epitaxial $\text{La}_{0.7}\text{Sr}_{0.3}\text{MnO}_3$ film, defined by a 2-dimensioal arrays of $2.5 \times 10^{-4} \text{ cm}^2$ masked pattern, on (100) NSTO single crystal substrate by PLD technique. The deposition process was performed under a substrate temperature

of 650°C and an ambient oxygen pressure of 100mTorr. Films with thickness of ~200nm were obtained. Post-annealing for ten minutes at the same deposition atmosphere was conducted to enhance crystallinity. Finally, spots of platinum electrodes were grown on both the $\text{La}_{0.7}\text{Sr}_{0.3}\text{MnO}_3$ and NSTO layers. The schematic side view of these p-n junctions is shown in Fig. 5.1.

i)



ii)

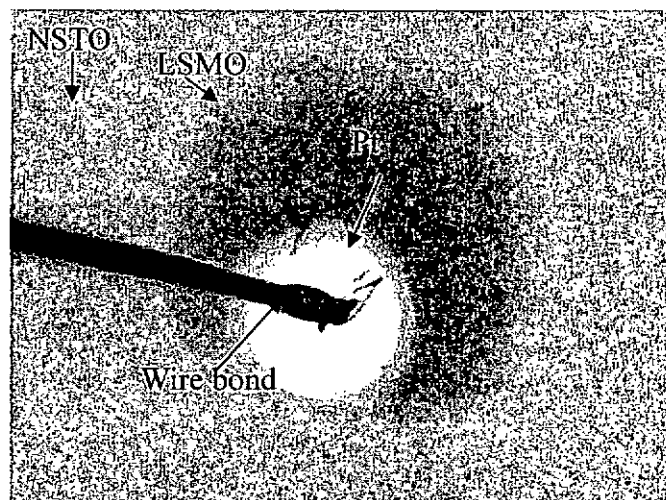


Fig. 5.1 Configuration of $\text{La}_{0.7}\text{Sr}_{0.3}\text{MnO}_3/\text{NSTO}$ junction i) the cross section schematic diagram and ii) top view photograph of the real object



5.2.2 Structural characterization of $\text{La}_{0.7}\text{Sr}_{0.3}\text{MnO}_3/\text{NSTO}$ junction

Fig. 5.2 shows the θ -2 θ XRD patterns of the PLD grown $\text{La}_{0.7}\text{Sr}_{0.3}\text{MnO}_3$ films on (100) NSTO single crystal substrate. Reflection peaks of single phase oriented $\text{La}_{0.7}\text{Sr}_{0.3}\text{MnO}_3$ and NSTO are observed in the XRD profile. It is seen that only the (h00) family of planes are observed. The sharp (200) peaks of NSTO and $\text{La}_{0.7}\text{Sr}_{0.3}\text{MnO}_3$ are observed at 46.4° and 47.34° respectively. They correspond to lattice constants of 3.91\AA and 3.84\AA . The out-of-plane lattice parameter of the grown $\text{La}_{0.7}\text{Sr}_{0.3}\text{MnO}_3$ film is almost the same as the $\text{La}_{0.7}\text{Sr}_{0.3}\text{MnO}_3$ bulk sample, which has the lattice constant a of 3.87\AA . The FWHM of the film (Fig. 5.3) is only 0.20° , suggesting an excellent grain orientation.

So far the out-of-plane structural characteristic of the $\text{La}_{0.7}\text{Sr}_{0.3}\text{MnO}_3$ films has been determined. The epitaxial relationship between the film and the substrate is examined by ϕ -scan, which not only gives the in-plane parameter of the sample but also the structural relation between the film and the substrate. Fig. 5.4 shows the ϕ -scan of the (202) $\text{La}_{0.7}\text{Sr}_{0.3}\text{MnO}_3$ and also the (202) NSTO reflection peaks. The four characteristic peaks of (202) $\text{La}_{0.7}\text{Sr}_{0.3}\text{MnO}_3$ are very sharp and their ϕ angles match with that of the (202) NSTO reflections. This is a clear indication of a cube-on-cube epitaxially grown of $\text{La}_{0.7}\text{Sr}_{0.3}\text{MnO}_3$ film on NSTO substrate.

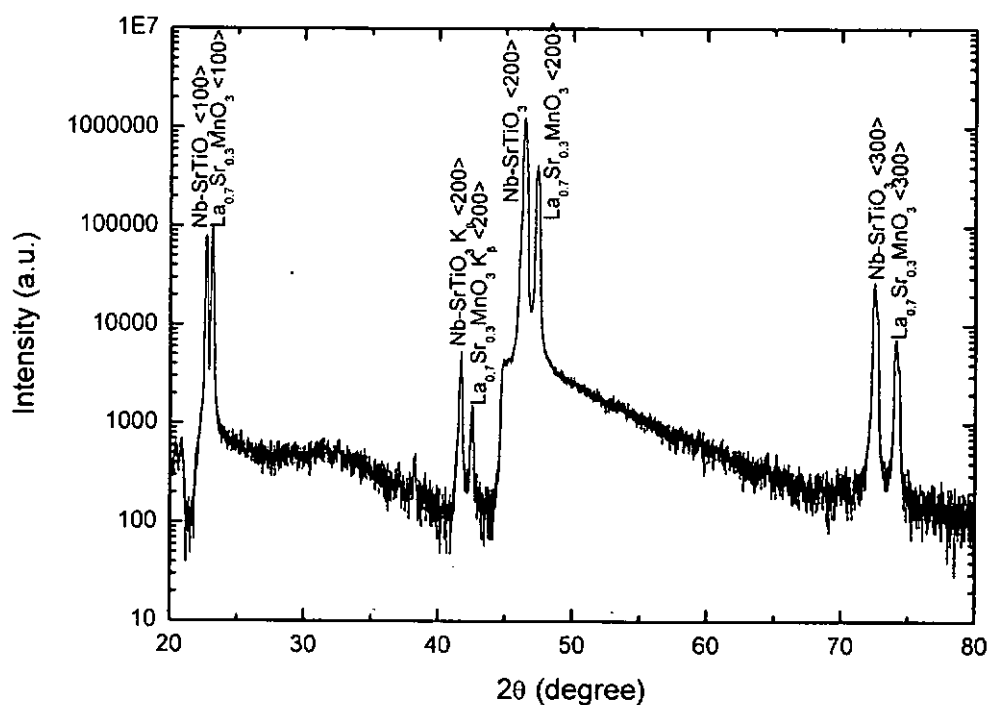


Fig. 5.2 θ -2 θ pattern of $\text{La}_{0.7}\text{Sr}_{0.3}\text{MnO}_3$ grown on single crystal (100) NSTO substrate

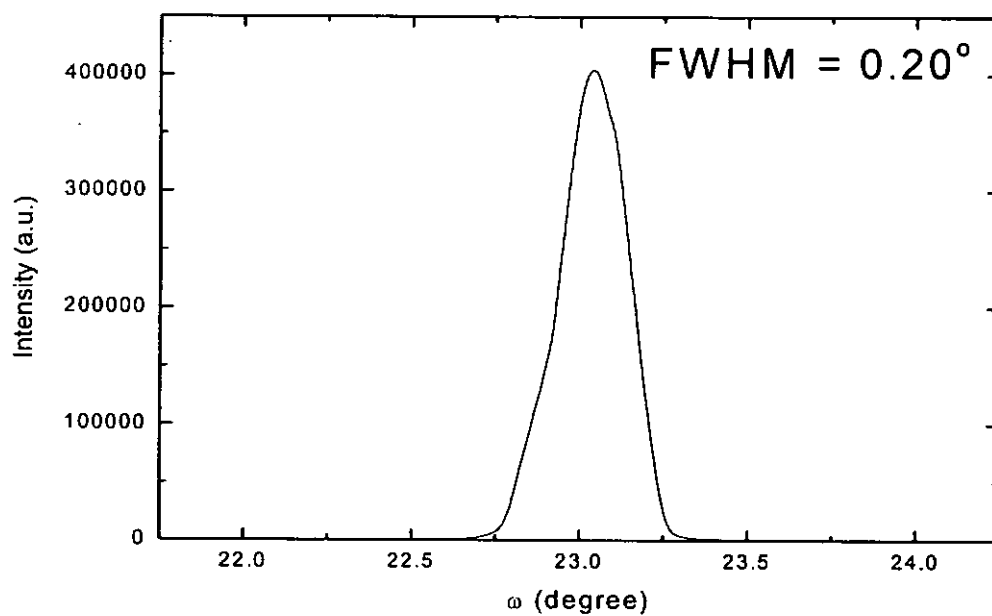


Fig. 5.3 The rocking curve of $\text{La}_{0.7}\text{Sr}_{0.3}\text{MnO}_3$ film grown on (100) NSTO single crystal substrate

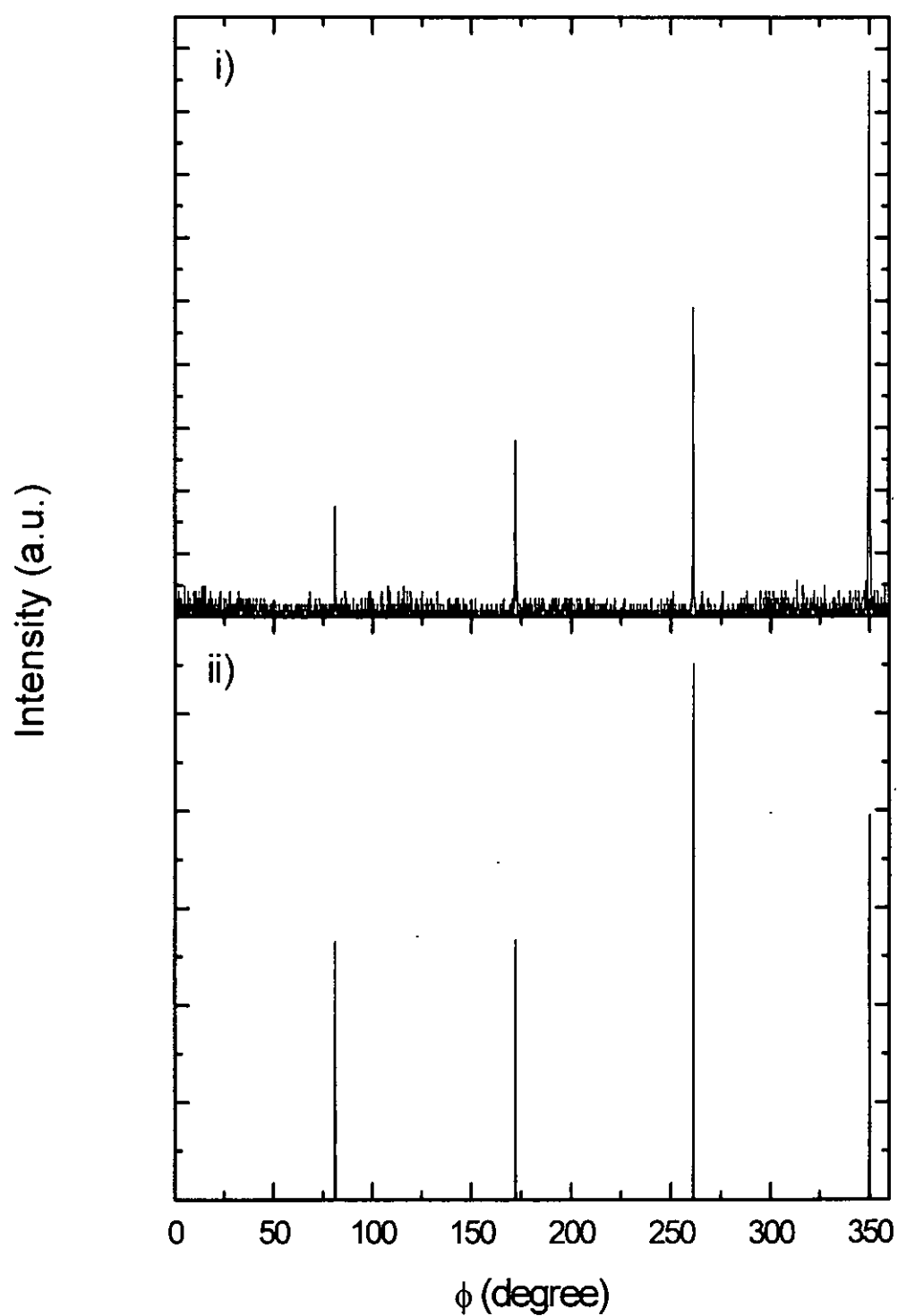


Fig. 5.4 ϕ -scan of i) (202) $\text{La}_{0.7}\text{Sr}_{0.3}\text{MnO}_3$ and ii) (202) NSTO reflection peaks



5.3 Electrical characterization of $\text{La}_{0.7}\text{Sr}_{0.3}\text{MnO}_3/\text{NSTO}$ junction

5.3.1 The influence of deposition pressure on $\text{La}_{0.7}\text{Sr}_{0.3}\text{MnO}_3$ film

This section aims to examine the effect of phase transition on the junction characteristic. It is known that the MR effect of manganese oxide is most prominent at around T_c . For ease of measurement, $\text{La}_{0.7}\text{Sr}_{0.3}\text{MnO}_3$ film with T_c at room temperature is most desirable. $\text{La}_{0.7}\text{Sr}_{0.3}\text{MnO}_3$ films grown under different deposition pressure are studied. Fig. 5.5 shows the R-T relation of $\text{La}_{0.7}\text{Sr}_{0.3}\text{MnO}_3$ films deposited at different ambient pressure. All the three $\text{La}_{0.7}\text{Sr}_{0.3}\text{MnO}_3$ films show a clear transition from metallic-like at low temperature to semiconducting-like at high temperature. Increase of deposition pressure raises the transition temperature, and the T_c value of the films gradually approaches to that of the bulk $\text{La}_{0.7}\text{Sr}_{0.3}\text{MnO}_3$ (350K). The data also reveals the oxygen dependence of the absolute resistivity of $\text{La}_{0.7}\text{Sr}_{0.3}\text{MnO}_3$. The resistivity of the film grown at 60 mTorr is one order of magnitude higher than that of film grown at 100mTorr. Eventually film grown under 100mTorr is used in the study because of its proximity of T_c (290K) to room temperature. Besides the influence of temperature on the single crystal NSTO substrate has also been investigated and no evident change is observed in its resistivity across the temperature range from 300K to 500K.

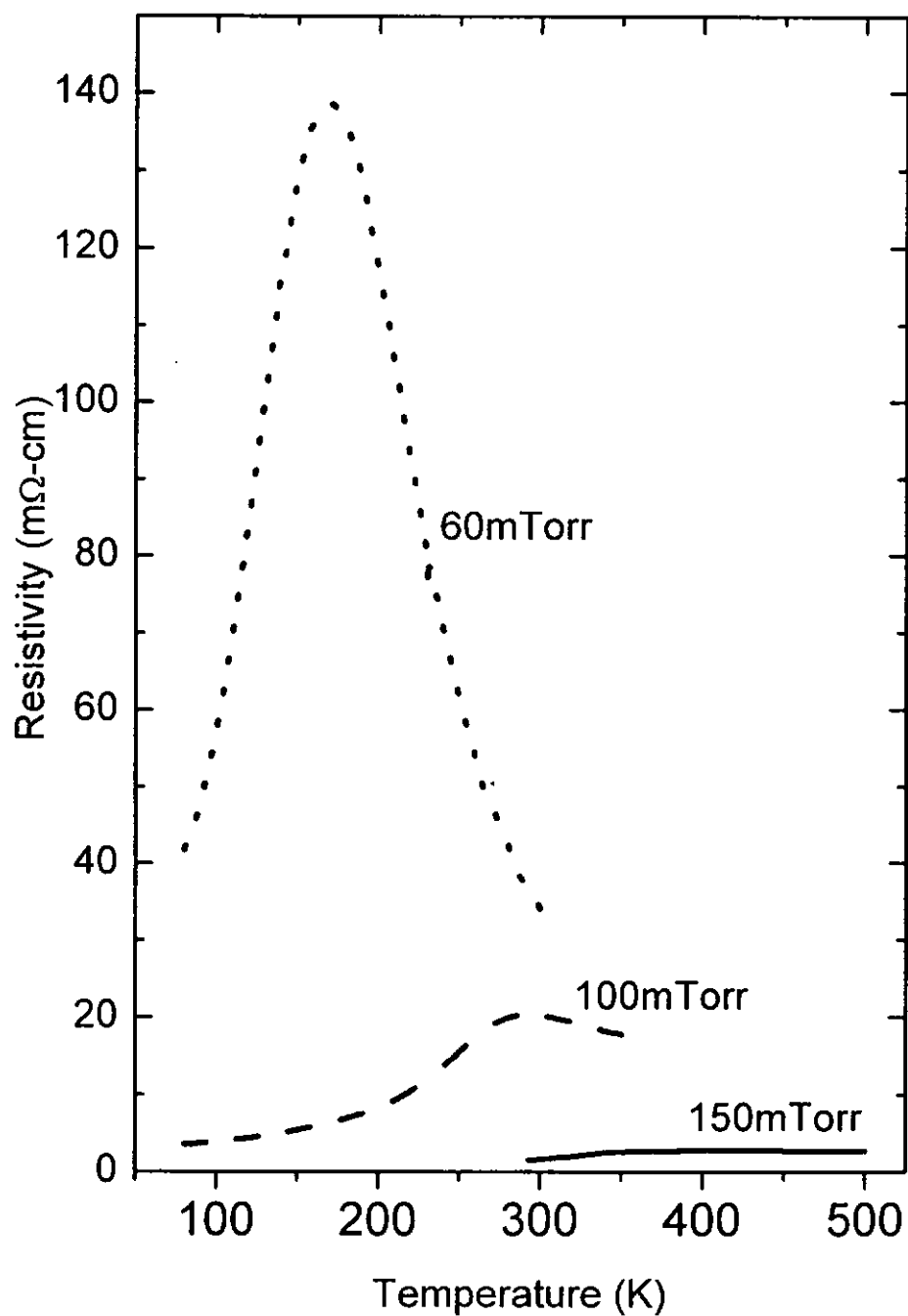


Fig. 5.5 Resistivity-temperature relations of $\text{La}_{0.7}\text{Sr}_{0.3}\text{MnO}_3$ films at different deposition oxygen pressure



5.3.2 I-V characteristics $\text{La}_{0.7}\text{Sr}_{0.3}\text{MnO}_3/\text{NSTO}$ junction

The room temperature I-V characteristic curve is displayed in Fig. 5.6. A fair rectifying profile having a turn-on voltage of 0.2V is obtained. The ideality factor of the junction is 1.4 (Fig. 5.7), indicating both the diffusion and recombination current are comparable to each other. The inset diagram shows the I-V characteristic of the Pt/NSTO junction. A linear relationship traversing the origin is obtained, inferring a good ohmic contact. That means the rectifying property measured in the Pt/ $\text{La}_{0.7}\text{Sr}_{0.3}\text{MnO}_3$ /NSTO heterostructure is the contribution from junction between the film and substrate. Unfortunately the junction exhibits a large leakage current under a relatively low reverse bias. This is the result of a narrow depletion layer. Both the $\text{La}_{0.7}\text{Sr}_{0.3}\text{MnO}_3$ film and NSTO substrate are highly conducting. The created depletion layer is therefore expected to be very narrow and the tunneling current is very large. To solve this problem, a thin layer (150nm) of insulating STO is introduced in between $\text{La}_{0.7}\text{Sr}_{0.3}\text{MnO}_3$ and NSTO. The tunneling current drops markedly but the forward bias current is depleted too. For example, the current in $\text{La}_{0.7}\text{Sr}_{0.3}\text{MnO}_3/\text{NSTO}$ is sixty times higher than that in $\text{La}_{0.7}\text{Sr}_{0.3}\text{MnO}_3/\text{STO}/\text{NSTO}$. In addition, the insulating layer also raises the turn-on voltage to 0.9V at room temperature. It is therefore difficult to compare the merits of the two junctions directly.

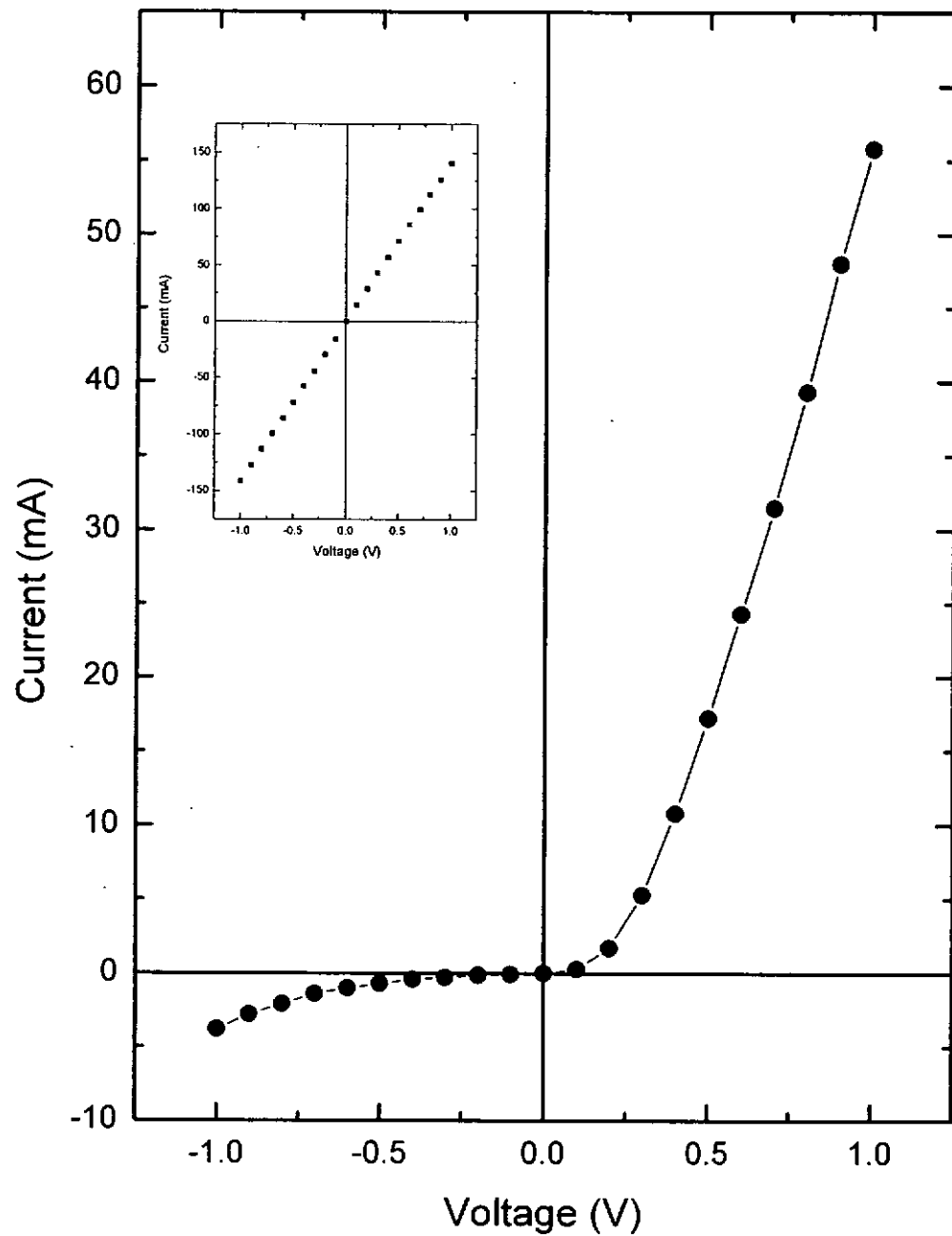


Fig. 5.6 I-V characteristic of $\text{La}_{0.7}\text{Sr}_{0.3}\text{MnO}_3/\text{Nb-SrTiO}_3$ at room temperature, inset diagram show the linear I-V relation of Pt/Nb-SrTiO₃/Pt junction

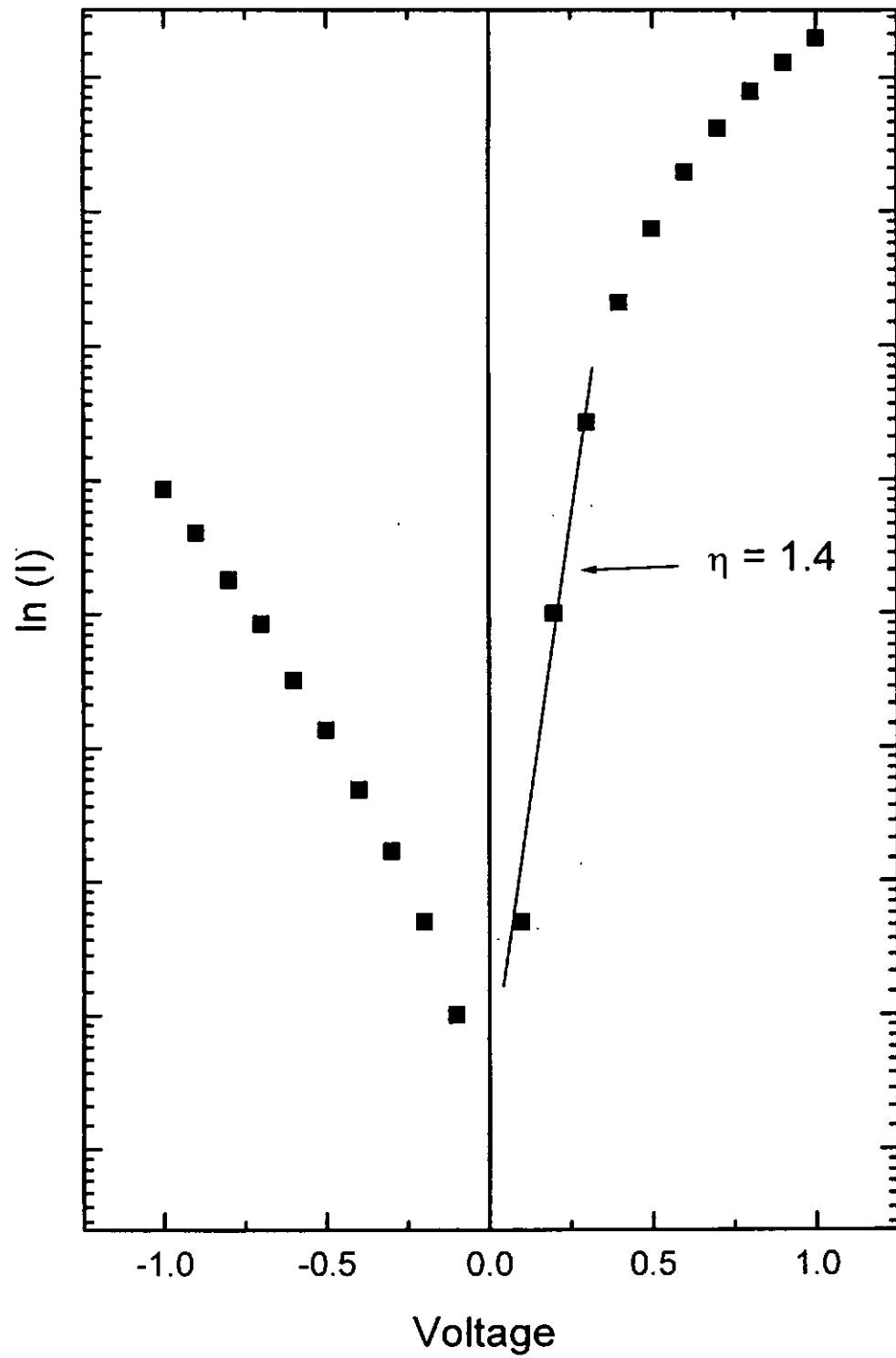


Fig. 5.7 The logarithmic current plot against voltage of $\text{La}_{0.7}\text{Sr}_{0.3}\text{MnO}_3/\text{Nb-SrTiO}_3$ junction under room temperature



The temperature dependences of the $\text{La}_{0.7}\text{Sr}_{0.3}\text{MnO}_3/\text{NSTO}$ and $\text{La}_{0.7}\text{Sr}_{0.3}\text{MnO}_3/\text{STO}/\text{NSTO}$ junction performance are evaluated. The influences of temperature on these junctions over the temperature range between 77K and 500K are shown in Fig. 5.8 and Fig. 5.11. The turn-on voltage of $\text{La}_{0.7}\text{Sr}_{0.3}\text{MnO}_3/\text{NSTO}$ junction decreases as the operation temperature is increased. It ranges from 0.2V to 0V for temperature from 77K to 500K. This feature is attributed to the increase of kinetic energy of the majority charge carriers so that they surmount the potential barrier more easily. Despite a continuous decrease in magnitude, the junction maintains an identifiable turn-on voltage till 380K. At above 380K a near ohmic relation is observed in the forward biased condition. Apart from a reduction of the turn-on voltage and an increase in forward biased current at higher temperatures, no evident change in slope of the I-V curve is observed. The NSTO resistance has not changed throughout the temperature range. The change of resistance in $\text{La}_{0.7}\text{Sr}_{0.3}\text{MnO}_3$ is small and can be neglected. So less variation of the slope values with the increasing temperature is observed. The current increases linearly with the temperature under a forward biased voltage of 0.5V as shown in Fig. 5.9. In a reverse bias condition, however, the raised temperature enhances the leakage current. Logarithmic plot of current against the inverse temperature is shown in Fig. 5.10. The current values fluctuate at the low temperature regime (77K – 220K). It then increases exponentially at higher temperatures. It is likely that charge carriers can not be activated with the thermal energy under $\sim 0.019\text{eV}$ (kT). Overall speaking, the phase transition seems not to play any role on the I-V characteristics of these all-oxide p-n junctions. The phase transition of LSMO occurs at around 290K. No abrupt changes in the I-V characteristic curves are seen at around 290K.

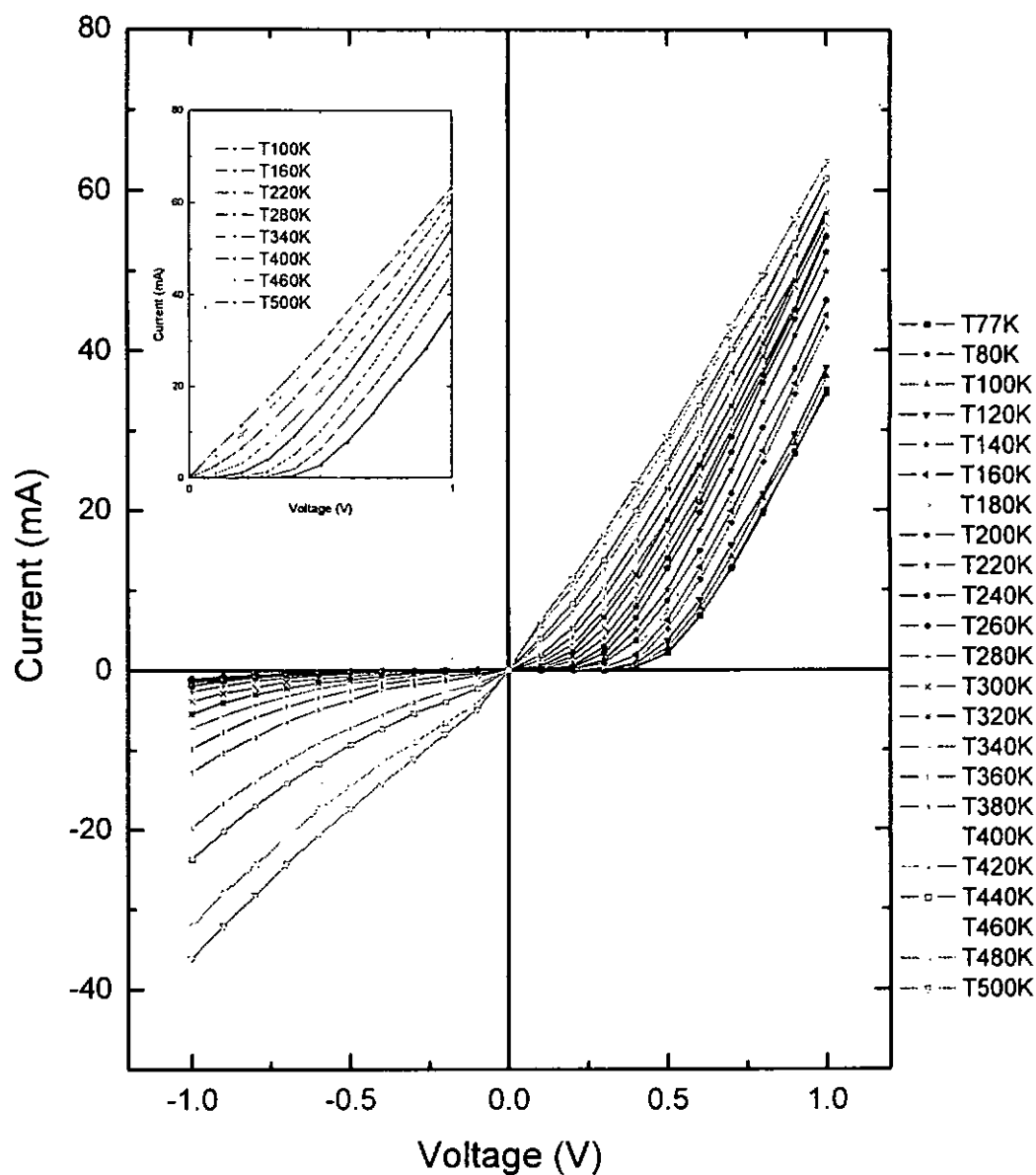


Fig. 5.8 Temperature dependence on I-V characteristics of $\text{La}_{0.7}\text{Sr}_{0.3}\text{MnO}_3/\text{NSTO}$ junction, inset shows the enlargement of some I-V profile on the forward biased condition

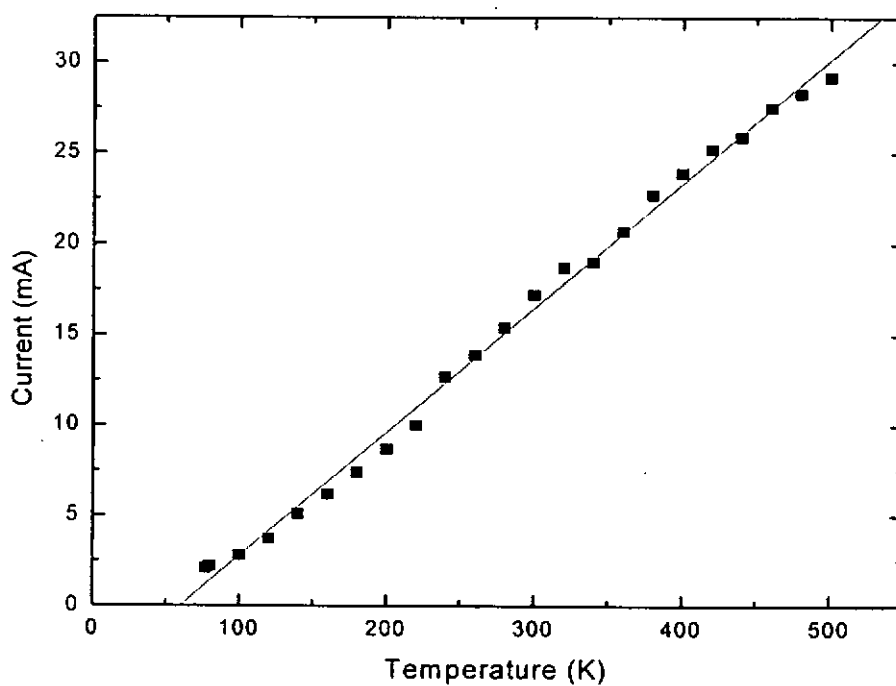


Fig. 5.9 Current-Temperature relation of $\text{La}_{0.7}\text{Sr}_{0.3}\text{MnO}_3/\text{NSTO}$ under the forward biased voltage of 0.5V

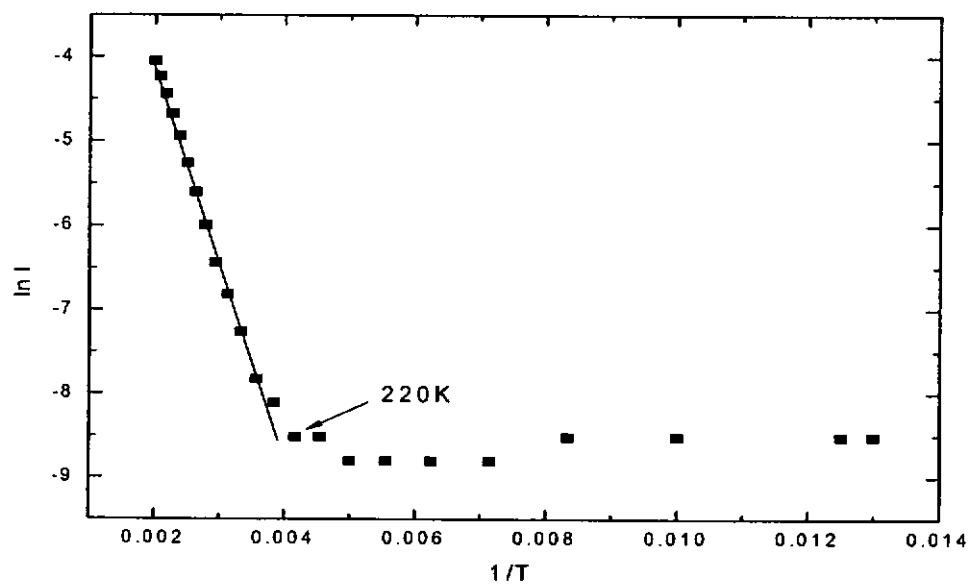


Fig. 5.10 Current-Temperature relation of $\text{La}_{0.7}\text{Sr}_{0.3}\text{MnO}_3/\text{NSTO}$ under the reverse biased voltage of 0.5V

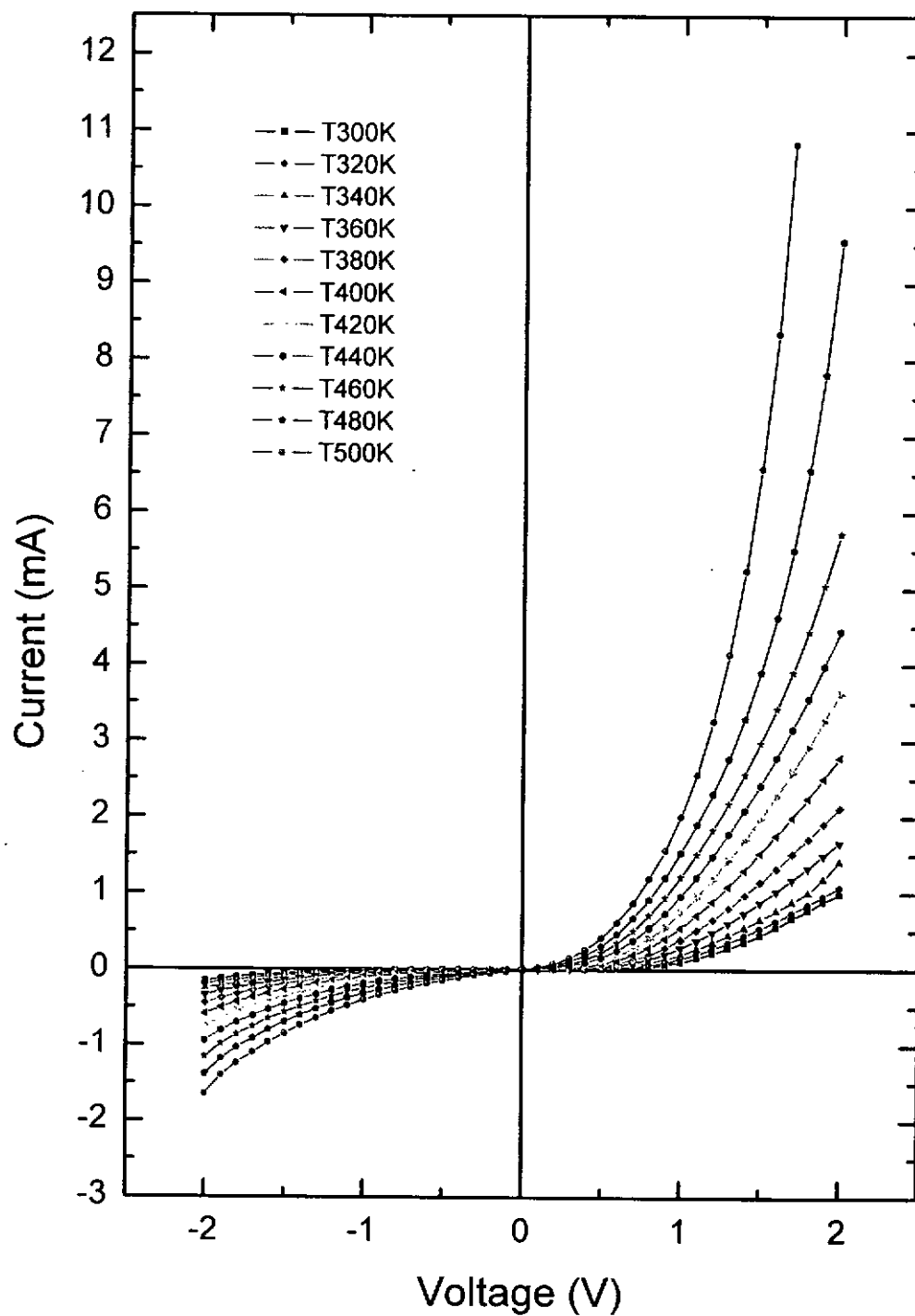


Fig. 5.11 Temperature dependence of the I-V characteristics of $\text{La}_{0.7}\text{Sr}_{0.3}\text{MnO}_3/\text{STO}/\text{NSTO}$ junction



Improvement of the p-n junction characteristic by insertion of a thin STO layer (150nm) to form a $\text{La}_{0.7}\text{Sr}_{0.3}\text{MnO}_3/\text{STO}/\text{NSTO}$ junction is shown in the temperature dependence I-V characteristic curves in Fig. 5.11. Although the diffusion current of this junction is much smaller than that of $\text{La}_{0.7}\text{Sr}_{0.3}\text{MnO}_3/\text{NSTO}$, the characteristic under reverse biased condition is much improved. This is particular so at high operation temperature. The leakage current increases exponentially with temperature. This is confirmed by the linear relationship in the logarithmic plot of current against the inverse temperature in Fig. 5.12. Similar to the $\text{La}_{0.7}\text{Sr}_{0.3}\text{MnO}_3/\text{NSTO}$ junction, the turn-on voltage decreases as the operation temperature is increased according to the same mechanism. Therefore a definable turn-on voltage is still observed in the I-V characteristic at 500K operation temperature. The change of slope is totally different for the $\text{La}_{0.7}\text{Sr}_{0.3}\text{MnO}_3/\text{STO}/\text{NSTO}$ and $\text{La}_{0.7}\text{Sr}_{0.3}\text{MnO}_3/\text{NSTO}$ junctions. The slope change in $\text{La}_{0.7}\text{Sr}_{0.3}\text{MnO}_3/\text{STO}/\text{NSTO}$ junction is much more apparent. The only difference between $\text{La}_{0.7}\text{Sr}_{0.3}\text{MnO}_3/\text{STO}/\text{NSTO}$ and $\text{La}_{0.7}\text{Sr}_{0.3}\text{MnO}_3/\text{NSTO}$ is the insertion of the STO layer. The STO layer is therefore likely to be the cause of the slope change. Sugiura and his coworker suggested that the insertion of the insulating STO layer would introduce the space-charge-limitation-current effect [Sugiura et. al. 2001]. The space-charge-limitation-current effect follows the voltage-temperature relation of $V_2 \propto \exp(E_t/2kT)$, and hence the current increases exponentially with temperature (Fig. 5.12 ii)). The slope change is caused by the temperature dependence of space-charge-limited-current effect on the p-i-n junction. Generally, the $\text{La}_{0.7}\text{Sr}_{0.3}\text{MnO}_3/\text{STO}/\text{NSTO}$ junction could retain a fine rectifying property at operation temperatures up to 500K.



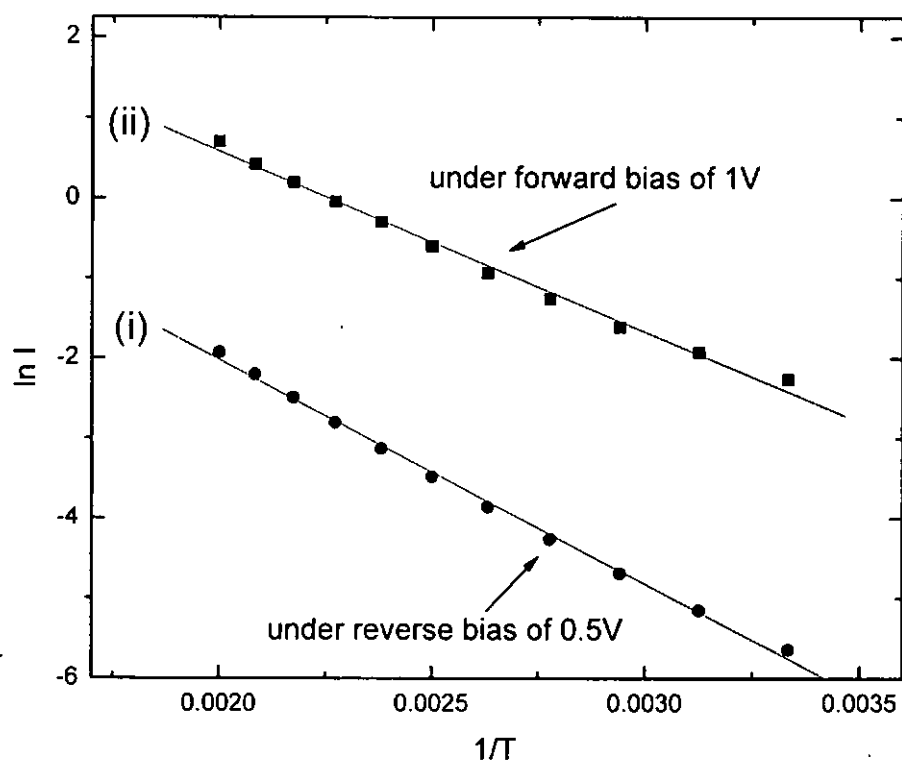


Fig. 5.12 Current against temperature relationship at (i) -0.5V and (ii) 1V deduced from Fig. 5.9



5.3.3 The influence of magnetic field on the manganite based $\text{La}_{0.7}\text{Sr}_{0.3}\text{MnO}_3/\text{NSTO}$ junction

The MR effect of the $\text{La}_{0.7}\text{Sr}_{0.3}\text{MnO}_3$ film deposited at 100mTorr has been measured at room temperature (300K). Although a high negative MR ratio at room temperature is expected, the MR ratio at the present $\text{La}_{0.7}\text{Sr}_{0.3}\text{MnO}_3$ film is only -4.5% under a magnetic field of 1 Tesla. The I-V characteristic curve of the $\text{La}_{0.7}\text{Sr}_{0.3}\text{MnO}_3/\text{NSTO}$ junction under a magnetic field of 1T is plotted in Fig. 5.13. As mentioned by Sun [Sun et. al. 2004], the application of magnetic field could modify the I-V relation significantly. In this study, no noticeable difference in the I-V curve has been observed. The absence of discernable effect in an external magnetic field may due to the small MR ratio of the grown manganite film (-4.5% as against the -90% reported by Sun). Another possible reason is that the measurement temperature is too high. The colossal magnetoresistance (MR) behavior only shows up just below T_c . And now the I-V characteristic measurement was carried out at 300K which is higher than T_c (290K). So now the effect of magnetic field on the manganite based $\text{La}_{0.7}\text{Sr}_{0.3}\text{MnO}_3/\text{Nb-SrTiO}_3$ junction is small. The actual cause, however, needs further studies. The inset shows the dominance of diffusion current against recombination current in the I-V characteristic.

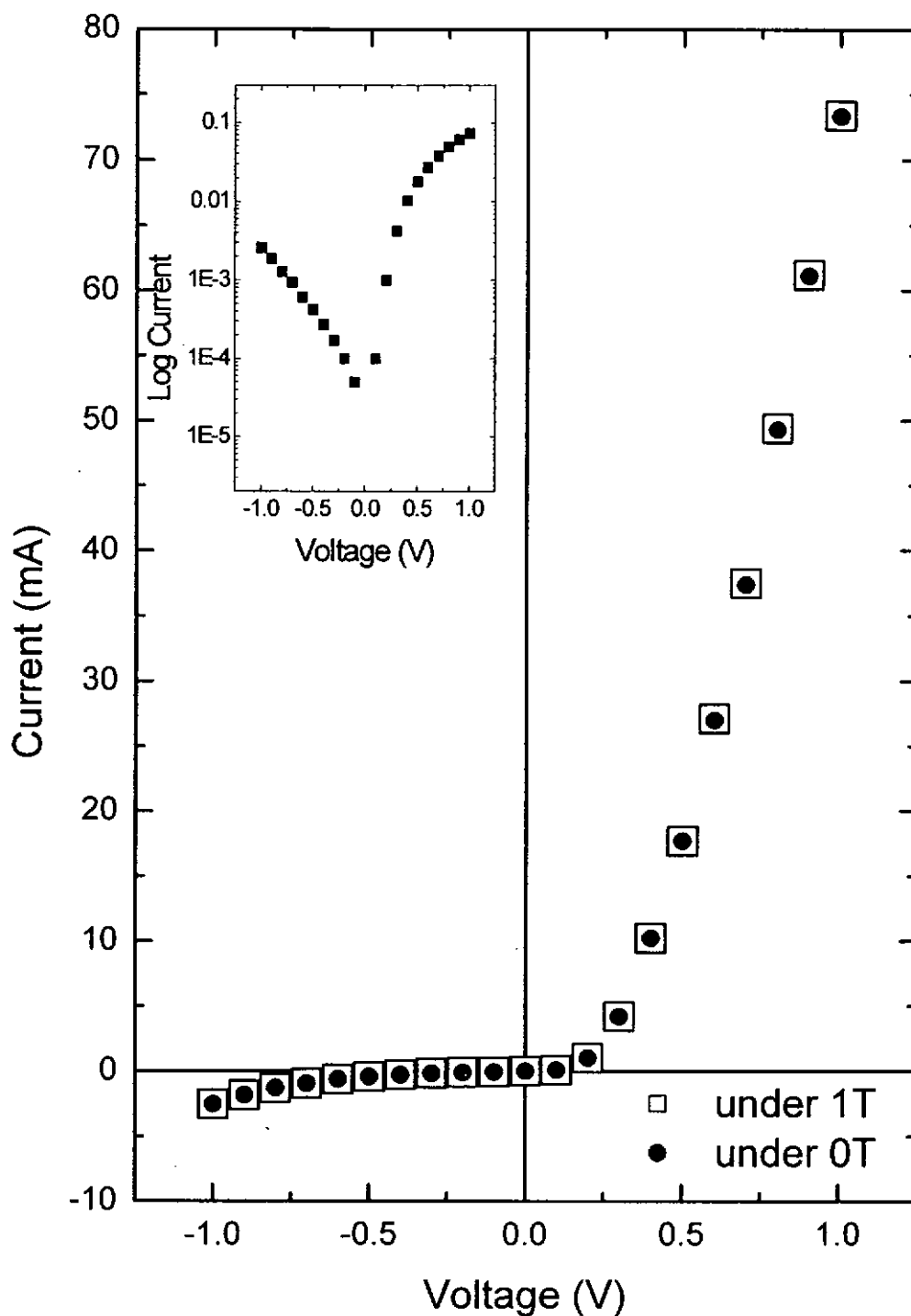


Fig. 5.13 Current-voltage characteristic curves of $\text{La}_{0.7}\text{Sr}_{0.3}\text{MnO}_3/\text{NSTO}$ with and without the application of 1T field



In conclusion, $\text{La}_{0.7}\text{Sr}_{0.3}\text{MnO}_3/\text{NSTO}$ junctions have been fabricated by simply growing a single layer of $\text{La}_{0.7}\text{Sr}_{0.3}\text{MnO}_3$ on NSTO substrate using PLD technique. The junction shows an ideality factor of 1.4 and it maintains a fair rectifying property at temperature up to 380K. The phase transition of LSMO at around 290K seems to bring about no apparent effect on the I-V characteristic. The reverse bias is large at high temperatures. A remedial measure by introducing an insulating STO layer to form a p-i-n junction has been attempted. A substantial reduction of the reverse biased current has been achieved. The p-i-n exhibits the rectifying property at 500K operation. The forward biased current is, however, greatly reduced by the STO. Although $\text{La}_{0.7}\text{Sr}_{0.3}\text{MnO}_3$ is a MR material, the junction shows no apparent different I-V characteristic at magnetic field of 1 Tesla.



Chapter 6

Fabrication and characterization of $\text{Li}_{0.15}\text{Ni}_{0.85}\text{O}/$ $\text{La}_{0.05}\text{Sr}_{0.95}\text{TiO}_3$ junction

6.1 Introduction

Transparent conducting oxides (TCO) are widely used in optoelectronic devices, such as flat panel displays, organic light emitting diodes [Kim et. al. 2001, 2003, Ohta et. al. 2000, 2002], solar cells, photodiodes [Choi et. al. 2002] and UV photodetectors [Yang et. al. 2001]. The use of transparent oxide to fabricate electronic devices is one of the sought-after researches in recent years. Indeed, an optical transparent p-n junction will be very interesting and useful. Transparent oxides have a wide band gap $> 3\text{eV}$. They normally have good optical transmittance at the visible and near-UV wavelengths. In fact, transparent oxides are themselves potential UV photo-detector materials. By choosing the appropriate oxides and tuning their bandgap energies via doping concentration, deep UV photo-detector for selected wavelength could be fabricated [Sharma et. al. 2003]. The wide band gap feature [Sawatzky et. al. 1984, 1992, Powell et. al. 1970] of transparent oxide also provides a higher thermal stability. It is expected the p-n junction formed by TCO could operate under high temperature. In this chapter, we will describe an all-transparent oxide p-n junction fabricated for UV photodetection. The junction could operate steadily at temperatures up to 500K.



We have fabricated an all-transparent-oxide p-n junction [Ohta et. al. 2003, Kudo et. al. 1999, Lee et. al. 1998] based on p-type Li-doped NiO and n-type La-doped SrTiO₃. NiO is a p-type conducting transition-metal oxide [Tachiki et. al. 2000]. Undoped NiO has a very high resistivity. Doping of divalent elements, however, introduces extra positive charge carriers and hence increases the conductivity substantially. Lithium is chosen as the dopant in this study [Shin et. al. 1999, Bosman et. al. 1966, Adler et. al. 1970]. With a 15wt% doping level of lithium, the insulating NiO film transforms to a conducting oxide film with a resistivity of 0.15 Ω-cm. Similar to NiO, the stoichiometric SrTiO₃ film is insulating. The replacement of strontium by lanthanum induces an extra amount of electron/negative charge carriers [Liu et. al. 2002, Tokura et. al. 1993]. Interestingly both the Li_{0.15}Ni_{0.85}O and La_{0.05}Sr_{0.95}TiO₃ films are transparent to the visible and near-UV wavelengths, having optical band gaps of ~3.7eV [Ohta et. al. 2003] and ~3.2eV [Sugiura et. al. 1999, Cardona 1963] respectively.

The structural characteristic of this junction have been inspected and described in latter sections of this chapter. It is estimated that a ~7% lattice mismatching occurs between the Li_{0.15}Ni_{0.85}O (LNO) and La_{0.05}Sr_{0.95}TiO₃ (LSTO) films. Following with the measurement on the electrical properties of single layer film, the R-T relations of LNO and LSTO have been studied. The temperature dependence on the I-V characteristic of the LNO/LSTO junction has also been investigated. Owing to the fact that the effect of bottom layer resistance may affect the junction characteristic measurement, two distinct junction configurations have been attempted.



The optical band gap energies of single layers of LNO and LSTO were deduced via the transmission measurement. Photo-responses on the single layer film as well as on the junction have been measured at different wavelengths. Temporal response characterization was accomplished by using an excimer laser pulse ($\lambda = 248nm$) of duration of 25ns.



6.2 Fabrication and characterization of the fabricated target and thin films

6.2.1 Fabrication and structural analysis of LNO target

Standard solid state reaction was used to fabricate both the Li-doped NiO and La-doped STO targets. The condition for preparing the LSTO target was discussed in chapter 4. The LNO target was fabricated as described in the followings. Li_2CO_3 and NiO are the starting materials. The weight amount of Li_2CO_3 and NiO are 1.14g and 14.9g respectively for making a 0.1 mole LNO. After the desired amount of powders were mixed with ethanol and then ball milled for 10 hours, the mixture was dried and ground to fine powder by mortar. Calcinations at 1100°C was carried out in order to get rid of the carbon component from the mixed powder and to initiate the chemical reaction. The calcinated powder was compressed by an oil-compressor at a pressure of 3.5 Ton into circular pellets of 2.5 cm in diameter and 3 mm thick. Final sintering at 1300°C was then carried out to obtain the desired ceramic target. Both the calcinations and sintering were done in air and lasted for 10 hours each at the desired temperature.

Structural characteristics of all as-prepared laser ablation targets were studied by XRD. Fig. 6.1 is the θ - 2θ scan of the LNO target. All the reflection peaks match well to the data defined by the data base (ICDD International Centre for Diffraction Data). EDX was carried out for composition investigation.

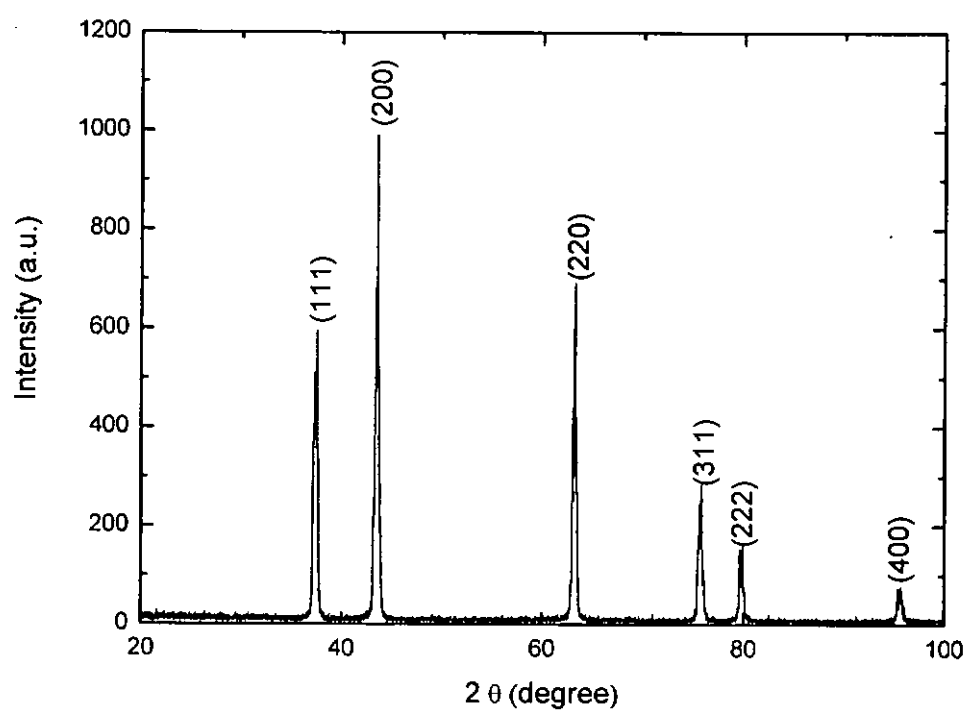


Fig 6.1 θ - 2θ scan of the bulk LNO target



6.2.2 Surface morphology of the single layer LNO film

The surface morphology of the LNO film was imaged by SEM. Generation of particulates is one of the major problems in PLD fabrication process. The presence of particulates on the deposited films leads to serious degradation on the junction performance. A clean interface between LNO and LSTO could give a sharp and abrupt depletion region. Any particulates at the interface, however, degrade the abrupt depletion boundary. Furthermore the particulates create additional paths for leakage current and hence destroy the junction performance. For a typical PLD of LNO films, SEM micrograph show the presence of a large amount of particulates on the film surface. It contributed to our unsuccessful first attempt on making LNO/LSTO junction, which exhibited ohmic I-V relation only.

Elimination of the particulates seems to be a must for obtaining workable p-n junctions. In this respect we have adopted the shadow mask PLD method for all subsequent film growth processes. As shown in Fig. 6.2, a square stainless steel mask of 1 cm^2 is placed in between the substrate and target. The macroparticles ejected from the target are blocked by the mask. Small clusters and atomic/molecular species on the other hand, will drift and bend around the mask in accordance to the hydrodynamic flow of the plasma stream. The amount of particulates on the film is substantially reduced. The price to pay in this shadow mask PLD technique is a reduced deposition rate ($\sim 1/3$ of the original) and perhaps a slight degradation of the crystallinity of the as-grown films. In the present case a relatively long deposition time of 30 minutes is

needed for the growth of 120nm thick film. SEM images of the surface of the LNO film with and without the use of shadow mask are shown in Fig. 6.3 for comparison.

Due to the above reason, all the LNO films are fabricated by the eclipsed pulsed laser deposition method. Although it is not shown here, the problem of particulate in the LSTO films is not as serious as in LNO films. This may due to the target quality and different desorption mechanisms. After considering the deposition time, particulate generation complexity of the setup, an ordinary pulsed laser deposition was used for LSTO films growth. Therefore two PLD setups were employed for the LNO and LSTO film fabrication. The structural characterization of these films will be discussed in the next section.

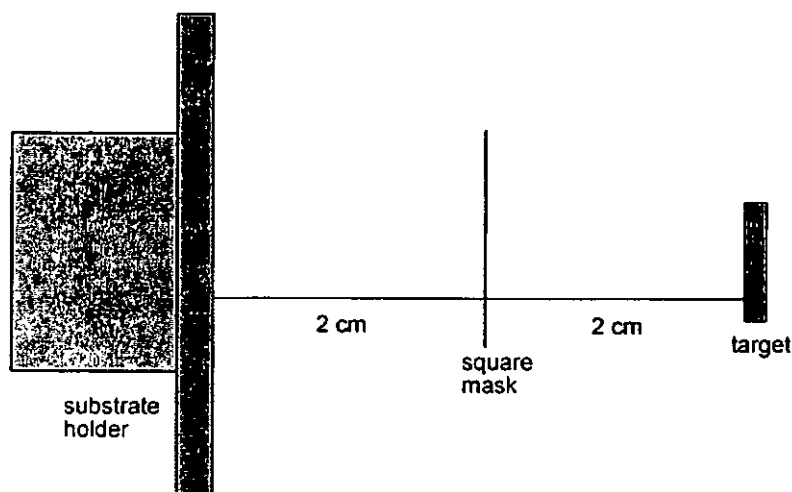
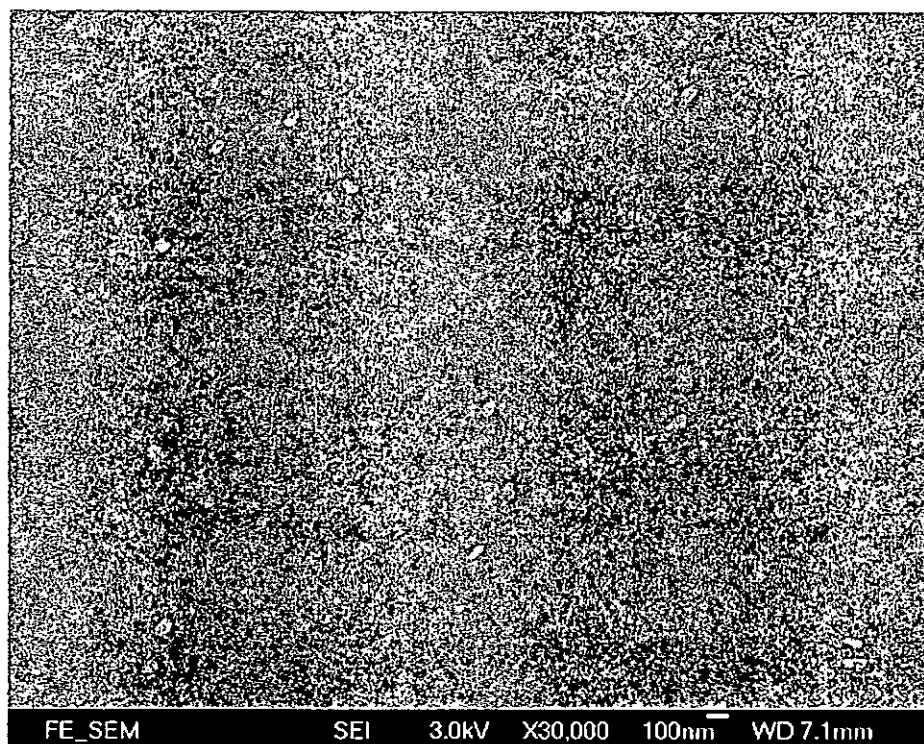


Fig. 6.2 The schematic diagram of the eclipse pulsed laser deposition setup.

i)



ii)

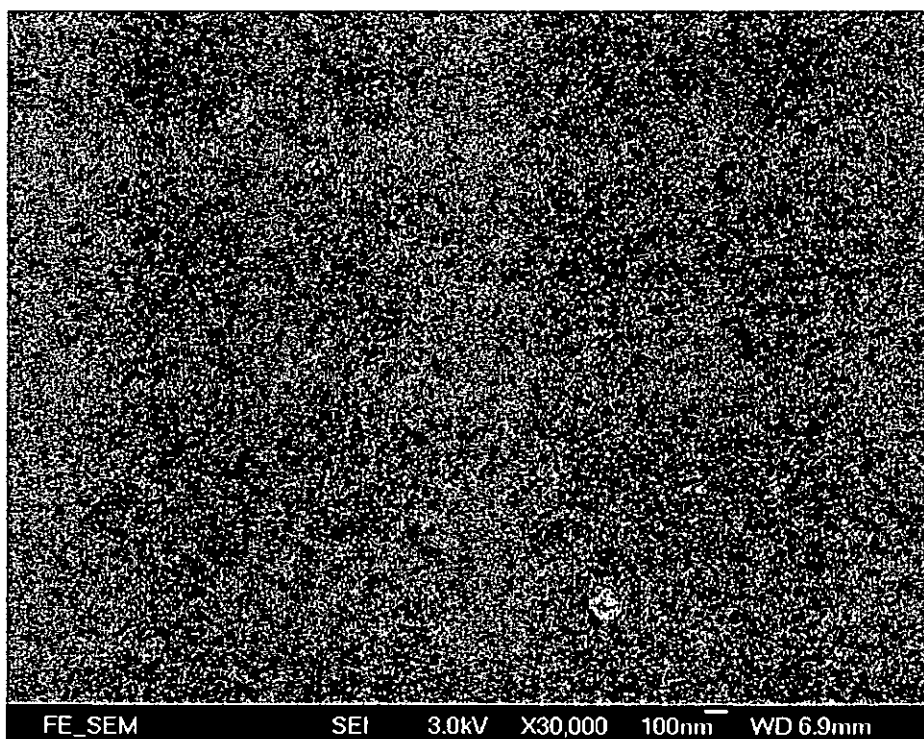


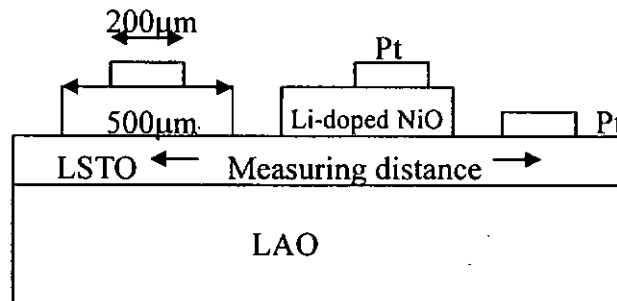
Fig. 6.3 SEM diagram of LNO films grown by i) Pulsed Laser Deposition method and ii) Eclipse Pulsed Laser Deposition method (the two large particulates are deliberately selected for focusing purpose)



6.2.3 Fabrication and structural analysis of LNO/LSTO junction

(100) LAO single crystal substrate (3.78\AA) was selected as the junction template owing to its closely matched crystal structure and lattice constant to those of LSTO (3.9\AA). A 200nm thick LSTO film was grown on the LAO substrate with deposition temperature of 500°C and ambient oxygen pressure of 100mTorr. It was followed by growing a 120nm thick LNO film, at the same deposition temperature and oxygen pressure. The selection of a relatively low deposition temperature is to avoid excessive lithium evaporation under high temperature. During the growth of LNO, eclipsed pulsed laser deposition was applied. In addition, the LNO was deposited through a patterned mask to form arrays of $0.5\text{mm} \times 0.5\text{mm}$ square patches. Finally spots of platinum electrode were grown on top of the LSTO/LNO heterostructure. Fig. 6.4 displays the schematic diagram and the top view image of such a LSTO/LNO junction.

i)



ii)

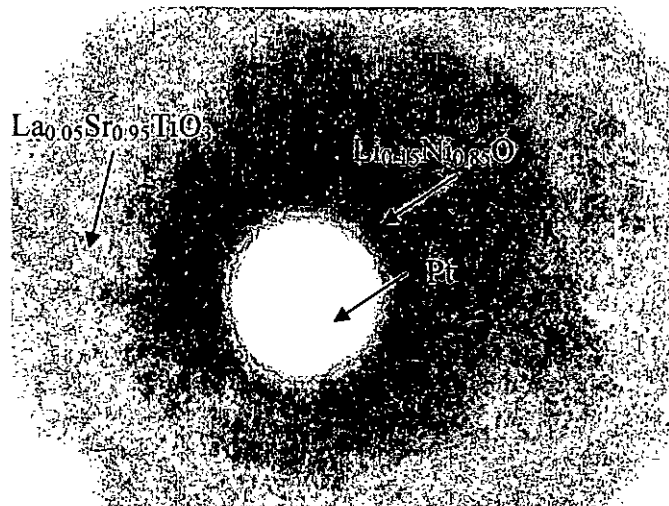


Fig. 6.4 The picture shows i) the schematic diagram of the p-n junction, ii) the top view image of the p-n junction.



6.2.4 Structural characterization of LNO/LSTO junction

The structural properties of the bi-layer heterojunction LNO/LSTO was characterized by XRD. Fig. 6.5 presents the θ - 2θ scan showing strong peaks of the (h00) family planes of LNO, LSTO and LAO. This is an indication of a single phase and oriented $\langle 100 \rangle$ LNO and $\langle 100 \rangle$ LSTO growth. The diffraction from the (200) planes of LNO and LSTO are represented by two sharp peaks at 43.52° and 46.67° respectively. Although the (200) LNO phase diffraction is fortuitously occurred at the same angle of the (200) LAO λ_p reflection, the strong (400) LNO reflection peak ensures the existence of the (200) LNO reflection peak. The out-of-plane lattice constants of LNO and LSTO are found to be 4.15\AA and 3.89\AA respectively, suggesting a 6.7% lattice mismatch.

Even though there is a relatively large lattice mismatch between these two films, the orientations of the two films remain good. Fig. 6.6 shows the rocking curves of LNO and LSTO with FWHM of 0.735° and 0.185° respectively.

Fig. 6.7 shows the $\langle 202 \rangle$ ϕ -scan profiles of the top LNO layer, the middle LSTO layer and finally the bottom LAO substrate. The four-fold symmetric diffractions in the 360° - ϕ scans confirm the cubic structure of the films and substrate. The cube-on-cube epitaxial growth is verified by the matched ϕ angle reflections among the three scans.

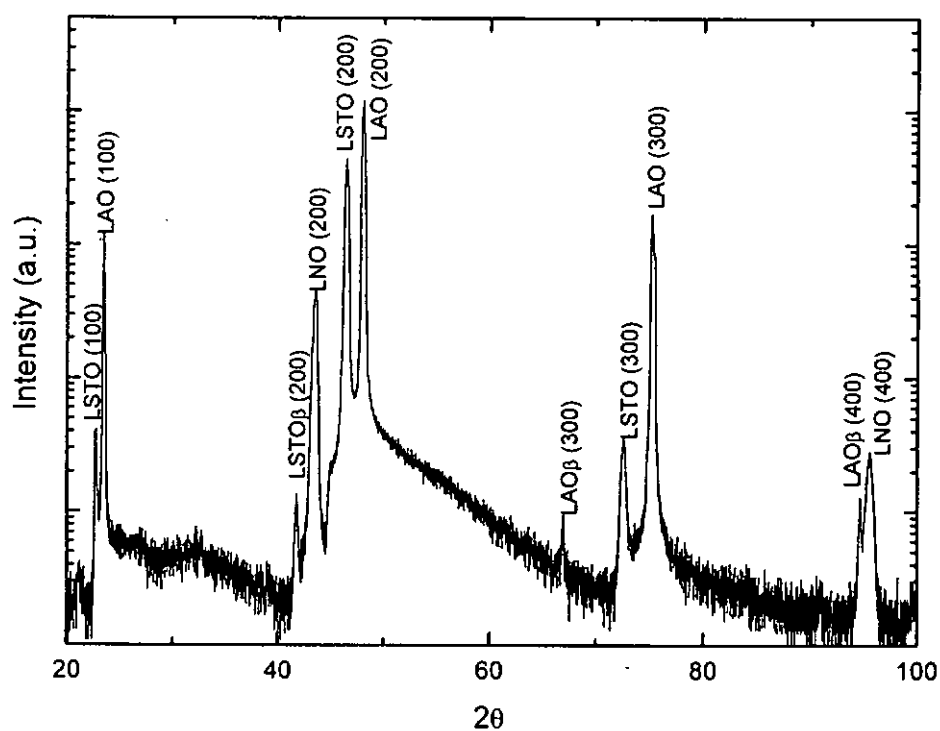


Fig. 6.5 X-ray θ - 2θ diffraction pattern of the LNO/LSTO junction

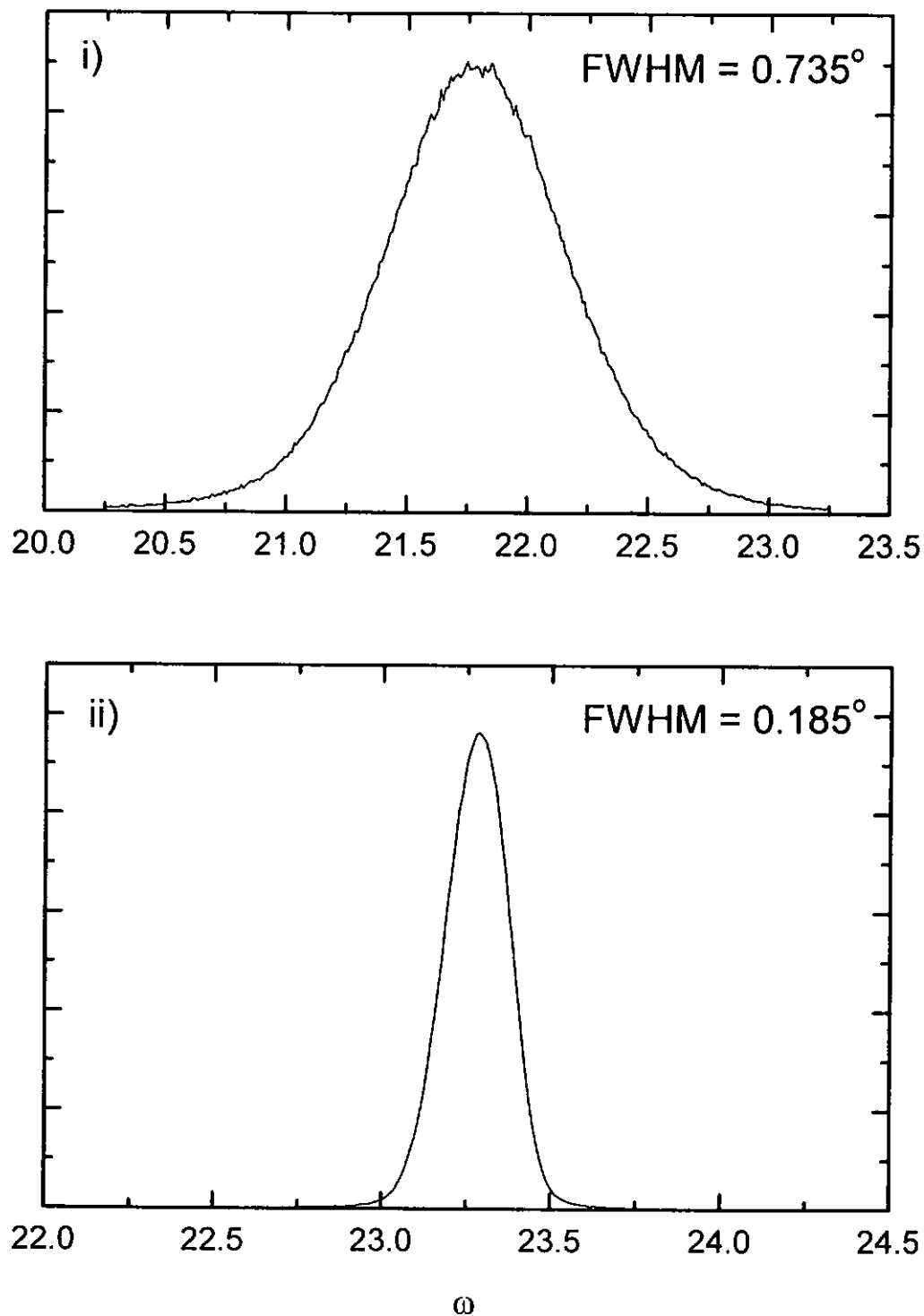


Fig. 6.6 The rocking curves of i) LNO and ii) LSTO of the junction

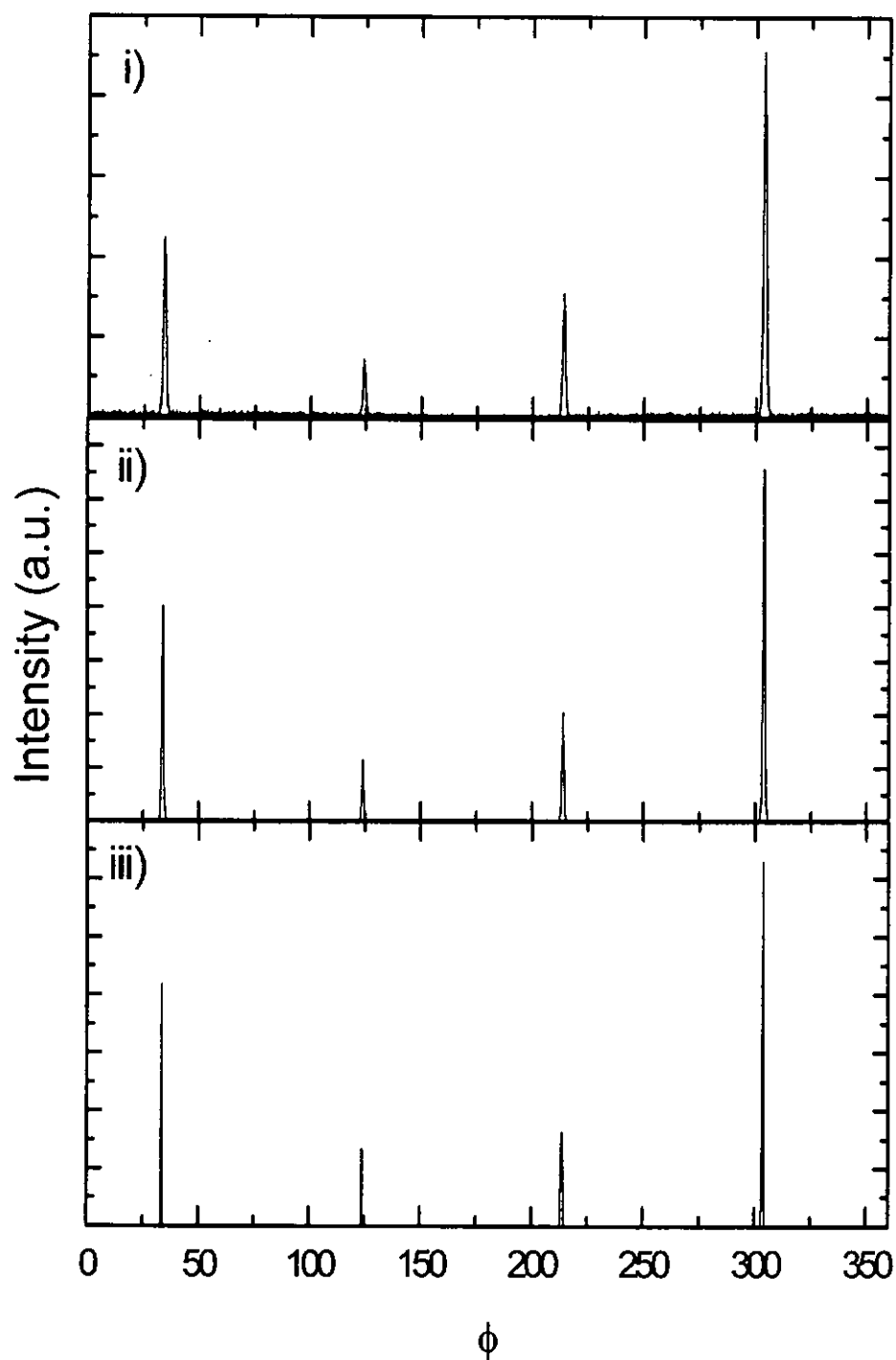


Fig. 6.7 The XRD ϕ -scans of the i) $\langle 202 \rangle$ LNO, ii) $\langle 202 \rangle$ LSTO and iii) $\langle 202 \rangle$ LAO of the LNO/LSTO junction



6.3 Electrical characterization of the single layer films and junction

6.3.1 R-T relation of single layer LNO and LSTO films

It is mentioned that LNO and LSTO are conducting oxides. Their conduction mechanisms are examined in details in the present work. The deposition temperature may alter the crystallinity and hence the conductivity of the film. Fig. 6.8 i) shows the resistivity of LSTO film from 300K to 500K. It is seen that the resistivity of the LSTO film (deposited at 500°C) is one order of magnitude larger than that of film grown under 650°C (Fig. 4.16). Charge carrier creation in LSTO is the result of oxygen deficient. High substrate temperature deposition promotes, in addition to crystallinity, the deficiency of oxygen species. This leads to better electrical conduction. In this study we did not attempt to grow LSTO films at lower deposition temperature than 500°C. The positive slope of the R-T profile suggests a metallic-like conduction. Although it is reported that the bulk LSTO has a R-T relation of $\rho \propto aT^2$ [Tokura et. al. 1993], our film exhibits a R-T relation of $\rho \propto aT^4$. Fig. 6.8 ii) depicts the resistivity of LNO film grown at 500°C. The absolute resistivity is a few Ω -cm, which is one order of magnitude higher than those of LSTO. It is also seen that the resistivity of LNO decreases exponentially with temperature, suggesting a semiconducting like film. Therefore a p-n⁺ junction can be created from mating the p-LNO and n⁺-LSTO together. The influence of the conduction mechanism of the oxide films on the junction performance will be examined in later sections.

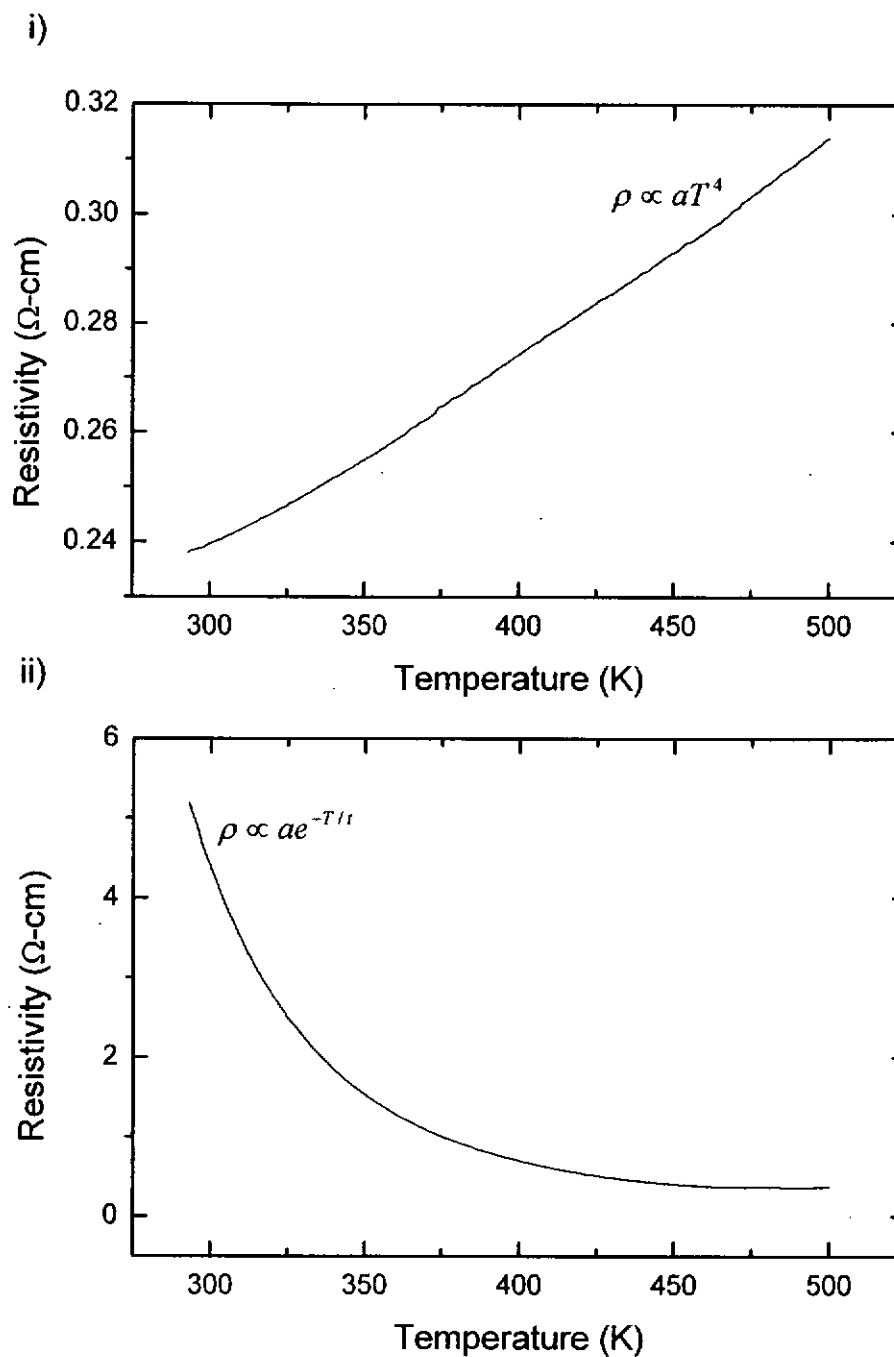


Fig. 6.8 Resistivity against temperature relations of i) LSTO and ii) LNO films deposited at 500°C

6.3.2 I-V characterization of the LNO/LSTO junction

6.3.2.1 I-V relations between the electrode layer and the oxide films

In order to study the rectifying properties of the junction and to eliminate the contributions from the metal electrode contacts, I-V characteristics of the Pt/LNO and Pt/LSTO junctions were examined first. Fig. 6.9 shows the linear I-V relationships traversing the origin. This corresponds to the ohmic I-V relation between the electrode and the films. After the ohmic contacts between the electrodes and films have been confirmed, the I-V characteristics of the junction formed by the two oxide layers are examined.

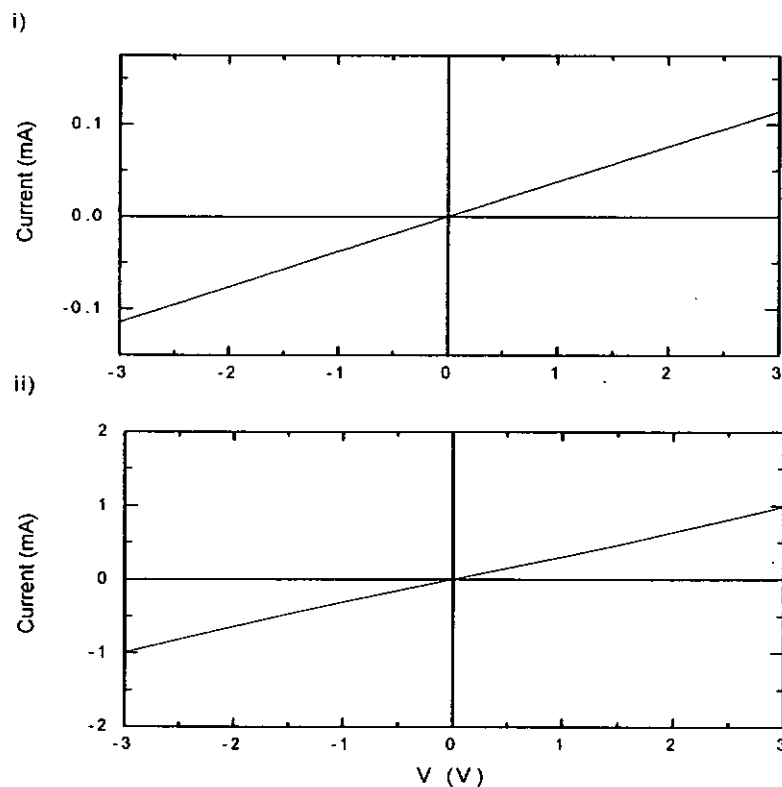


Fig. 6.9 I-V relations of junctions between Pt and i) LNO, ii) LSTO



6.3.2.2 Comparison between LNO/LSTO/LAO and LSTO/LNO/LAO junctions

As mention before, the R-T characteristics of LNO and LSTO differ substantially. This may lead to unexpected changes in the junction performance. As reported in chapter 4, the resistivity of the LSTO bottom layer affects the slope of the I-V curve at forward biased condition. Accordingly the LNO/LSTO/LAO and LSTO/LNO/LAO junctions are fabricated and their I-V characteristics are studied. Fig. 6.10 illustrates the I-V profiles of these two junctions at 295K. It is reasonable to anticipate that the two configurations would give the same I-V characteristics. In fact, the energy band structure is the same for both configurations. They have the same turn-on voltage of 0.3V, meaning that there is no change in diffusion barrier. However, the absolute currents for these two junctions are not the same as shown in Fig. 6.10. It may be the results of the two different layers arrangements. The large series resistance contributed from the bottom layer limits the absolute circuit current. Accompanied with the large resistance difference (one order of magnitude) between LNO and LSTO, these two junctions exhibit dissimilar slope. However the difference in leakage current is not so clear at the moment. The tunneling effect is the major cause for such a leakage current to occur. However the configuration should induce no characteristic change and further experiments are necessary.

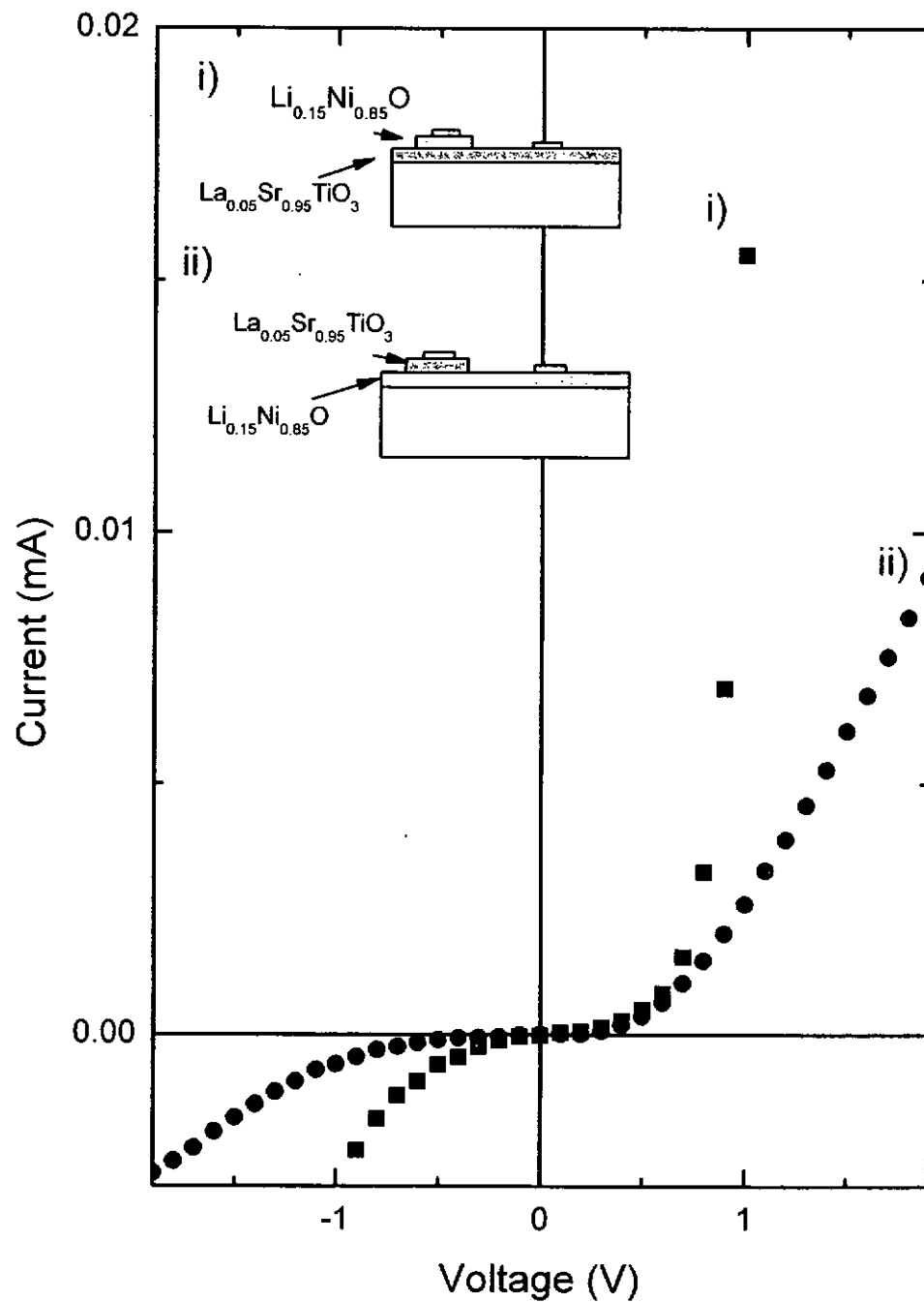


Fig. 6.10 I-V characteristics of the two differently configured junctions: i) LNO/LSTO/LAO and ii) LSTO/LNO/LAO



6.3.2.3 The temperature dependence of LNO/LSTO/LAO and LSTO/LNO/LAO junctions

In the last section, the difference in junction characteristics between LNO/LSTO/LAO and LSTO/LNO/LAO are highlighted. In this section we present the temperature dependence I-V characteristic of these junctions. Their dissimilarities are emphasized. The possible causes of such varied features are also discussed.

The I-V properties of these two junctions are measured with a ramp voltage from -2 to 2 Volts. The junctions, together with the substrates and electrodes are adhered to a temperature controlled hot-plate. The temperatures ranging from 295K to 493K are used. Fig. 6.11 and Fig. 6.14 display the corresponding I-V profiles. For both junctions, the turn-on voltage reduces with increasing temperature. It is believed that high temperature leads to the increase of thermal energy of the majority charge carrier, and hence the turn-on voltage is decreased.

Despite the similar changes of the turn-on voltage as function of temperature, the variation of the slope of the I-V profile in the forward biased regime and the leakage current in the reverse biased regime are totally different among these two junctions. Let us discuss the slope variation of the two junctions first. For a conventional semiconductor p-n junction, the slope just increases slightly upon the rising temperatures. In our case both the LNO/LSTO and LSTO/LNO show large temperature dependence. It may due to



the effect of a large series resistance contribution from the bottom layer according to the sample setup and electrical connection configuration as sketched in Fig. 6.4 i). For LNO/LSTO junction, the slope decreases as the temperature is increased. The result contradicts the normal tendency of a traditional p-n junction characteristic. We believe the observed feature in our sample is primarily the result of the positive R-T relation of the bottom LSTO layer. As concluded in chapter 4 that if the series resistance contributed from the oxide layer is comparable to the junction resistance, the change in resistivity on the single oxide layer acts as a loading resistor in the circuit and dominates the I-V profile. The resistance of LSTO ($3\text{k}\Omega$) is comparable to the junction resistance at about the turn-on voltage. Since the resistivity of LSTO increase with temperature, the series resistance of the circuit increases and hence the slope of the I-V curve reduces at increased temperatures. Fig. 6.12 compares the temperature dependent resistance of LSTO and LNO/LSTO junction. The two curves show more or less the same positive linear relation. The exponential increase of leakage current against temperature is confirmed in Fig. 6.13. It reflects how the thermal effect acts on the junction and behaves just the same to a conventional semiconductor junction. Our all-oxide p-n junction exhibits a fair rectifying property. It is also confirmed that the oxide junction could operate stably at temperatures up to 493K with no apparent degradation.

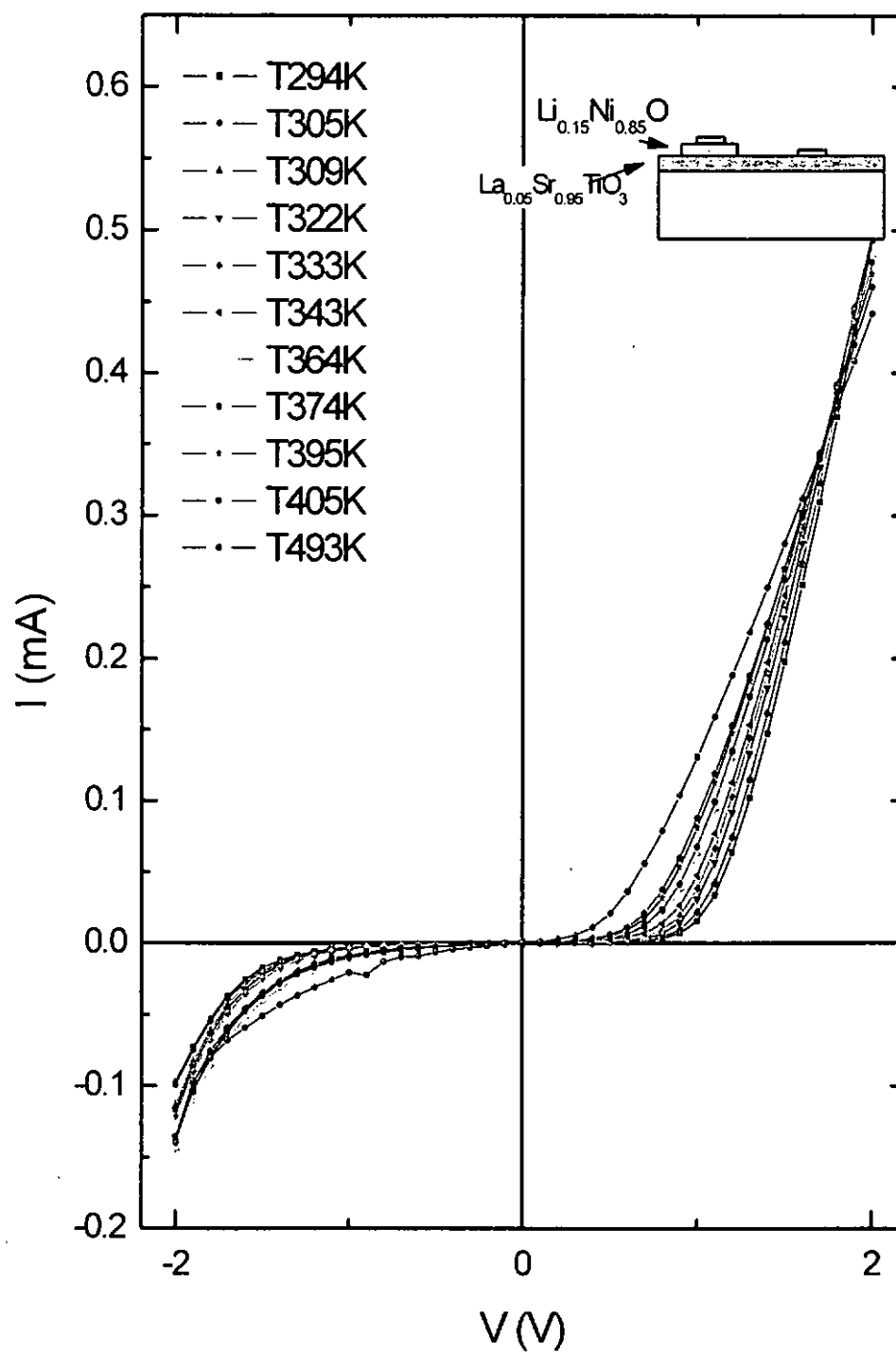


Fig. 6.11 Temperature dependence of the I-V characteristics of the LNO/LSTO junction. The inset shows the schematic diagram of the junction

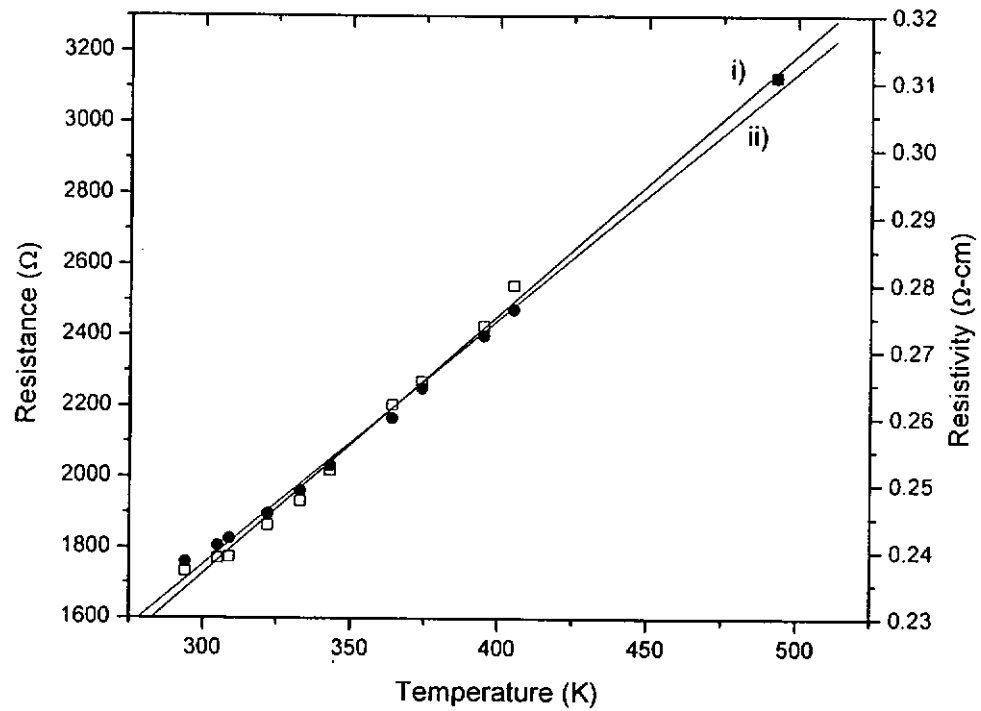


Fig. 6.12 Temperature dependence of i) resistivity of LSTO and ii) junction resistance of LNO/LSTO

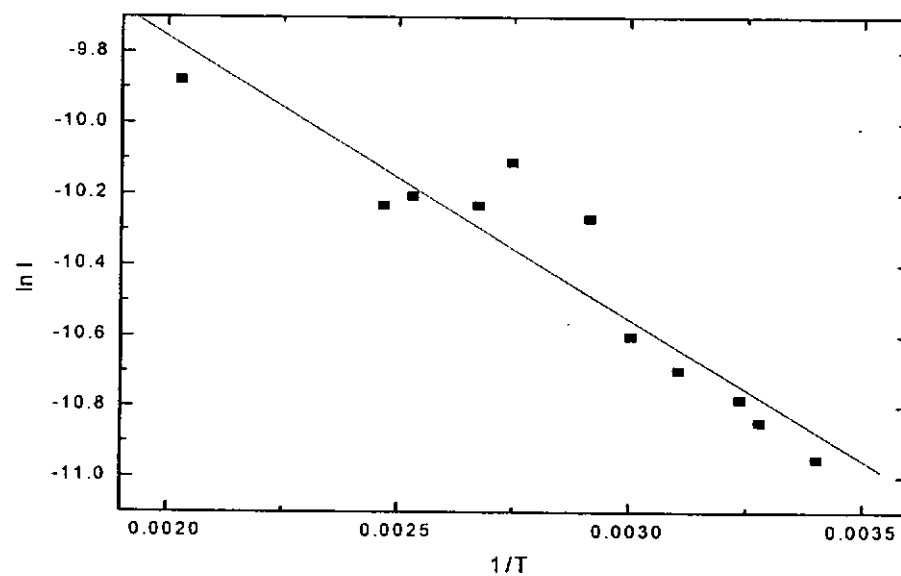


Fig. 6.13 Temperature dependence of the leakage current under a reverse bias of 0.5V for the LNO/LSTO junction



We now come to scrutinize the LSTO/LNO junction. Similar to the LNO/LSTO junction, the resistance of LNO is comparable to the junction resistance. The measured junction resistance from the I-V curves shows an exponential decay with temperature. This is clearly seen in Fig. 6.15. The R-T relation of LNO is also drawn side by side for comparison. Both curves show decay profiles with temperature. For a more accurate collation of the junction resistance with that of the LNO film, a logarithmic plot of resistivity against the inverse temperature is made and depicted in the inset of Fig 6.15. Both lines show a similar positive linear relation. The contribution and dominance of the LNO bottom layer to the I-V curve are evident. Once again thermal effect occurs in this junction, which leads to the exponential increase in leakage current against temperature. This is indicated in Fig. 6.16. However it is noted that the thermal degradation in the LSTO/LNO junction is more serious than that in the LNO/LSTO junction. In general, the LSTO/LNO junction retains a good rectifying property at temperatures up to 353K. At above 373K, asymmetry is still observed in the I-V profile but the leakage current increase rapidly. When the operation temperature reaches 423K, the I-V characteristic becomes a linear line traversing the origin. The possible cause of the large leakage current at low reverse biased voltage is again due to the bottom LNO layer, which contributes a series resistance to the measuring circuit loop. As the resistance of the LNO layer is one order of magnitude higher than that of LSTO, the series resistance of LNO assumes an earlier dominance over the p-n junction resistance. As a result the leakage current increases rapidly with temperature even at low reverse biased voltage.

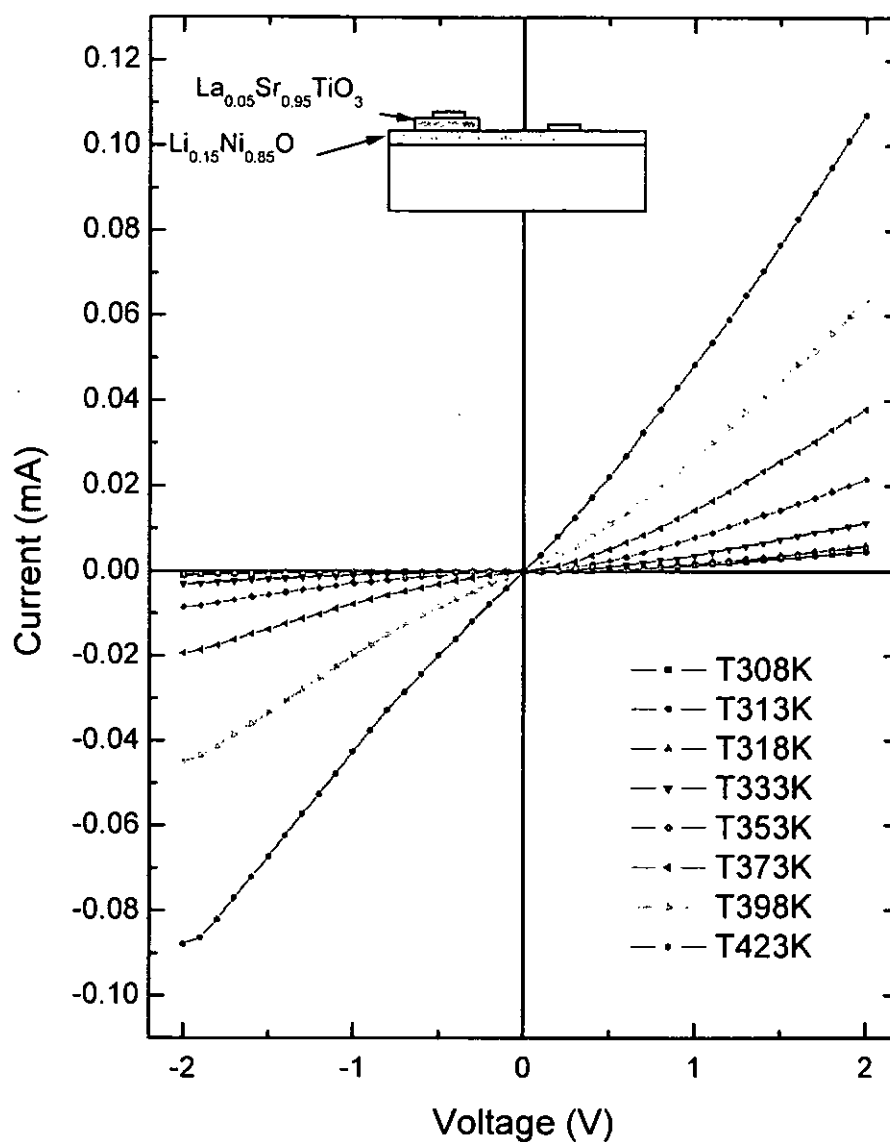


Fig. 6.14 Temperature dependence of the I-V characteristics of LSTO/LNO junction, the inset shows the schematic diagram of the junction

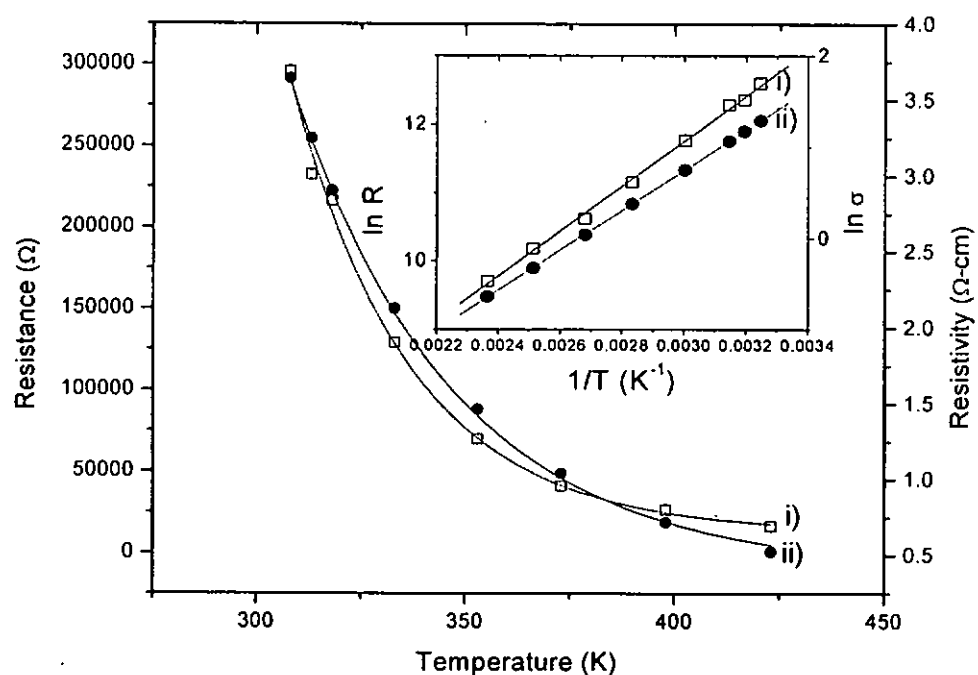


Fig. 6.15 Temperature dependence on the i) resistivity of LNO and ii) junction resistance of LNO/LSTO, the inset show the two re-plots of these data in logarithmic form

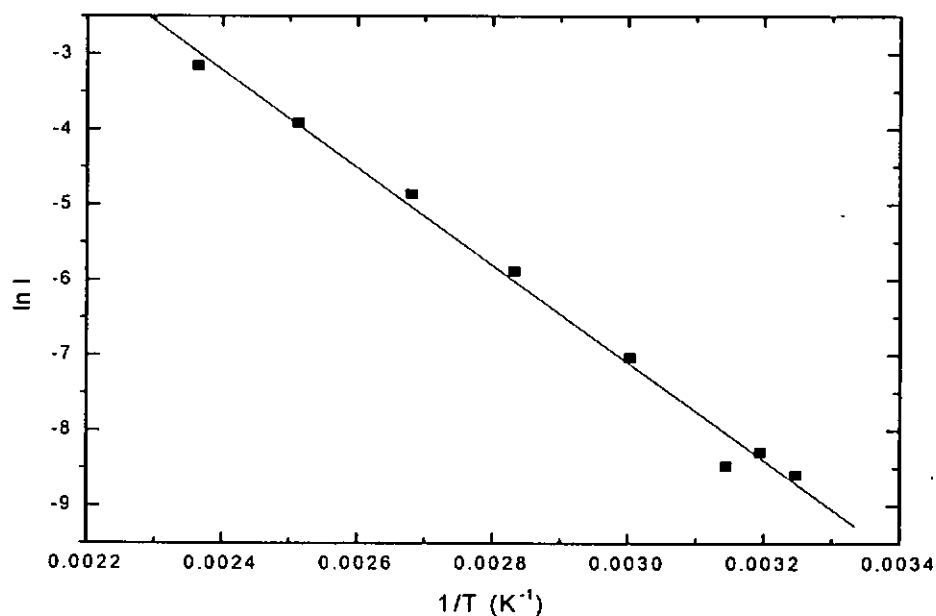


Fig. 6.16 Temperature dependence of the leakage current under a reverse biased of 0.5V on LSTO/LNO junction



6.3.2.4 SrTiO₃ thickness dependence of LNO/STO/LSTO/LAO junction

So far two different junctions have been investigated amid a slight disappointment on the relatively small breakdown voltage at around -1.5V for both junctions. In order to remedy the large tunneling current and the small breakdown voltage of these bi-layered all-oxide p-n junctions, an insulating SrTiO₃ (STO) layer is inserted in between the p-type and n-type oxides to broaden the transition region. The film growth condition of LNO and LSTO are remained unchanged. The additional STO layer is grown, in sequential order immediately after the LSTO layer, at deposition temperature of 500 °C and under an ambient pressure of 100 mTorr. With the STO insertion, the absolute current through the junction decreases due to the insertion of the high resistance of the insulating layer. Fig. 6.17 displays four I-V characteristics with different thickness of the STO insertions. A substantial reduction of the tunneling current is confirmed. The breakdown voltage has been increased and is a strong function of the insulating layer thickness. The inset reveals a positive proportionality of the turn-on voltage with the thickness of STO. STO layer of thickness of 160nm shows turn-on voltage (0.3V) and breakdown voltage (-0.9V) very close to that of the original bi-layer junction. It seems that STO with thickness of 160nm or less could not help to suppress the large tunneling current. With a further increase of the STO thickness, however, the tolerance to breakdown and charge carrier tunneling has improved. At STO thickness of 400nm, the reverse biased breakdown voltage is reduced to -4.6 V (not shown here). At the same time, a larger turn-on voltage of 1.4eV is obtained. Generally,

reduction of the leakage current in the LNO/LSTO junction can be achieved by insertion of a STO insulating layer. The thickness of such a layer, however, has a pivotal effect on the junction characteristics. Indeed, in using a particular STO layer thickness, one has to compromise the effects of leakage current, breakdown voltage, forward biased current and turn-on voltage.

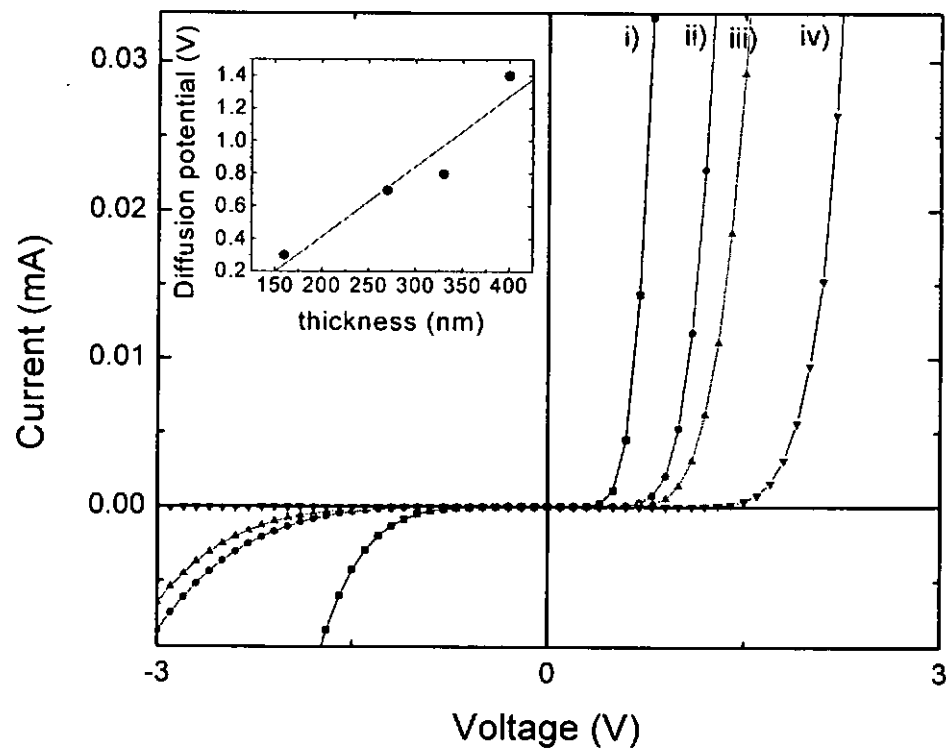


Fig. 6.17 I-V characteristics of LNO/STO/LSTO junction with different thickness of STO insertions: i) 160nm, ii) 270nm, iii) 330nm and iv) 400nm. Inset shows the thickness dependence of turn-on voltage on STO layer thickness



6.4 Optical characterization of LNO/LSTO junction

The high temperature operation of the LNO/LSTO junction has been corroborated. We now turn to examine its possibility use for UV detection. Here the photo-responses of the oxide thin films and junction will be explored. The LSTO films are visually transparent irrespective of the deposition conditions. The LNO films, on the other hand, are darkened slightly when grown at low deposition temperature. Its resistivity, however, increases with deposition temperature. Therefore a compromised temperature of 500°C is selected to grow all the LNO films, so that they remain transparent and keep a relatively low resistivity of $\sim 4 \Omega\text{-cm}$.

6.4.1 Transmission spectral of LSTO, LNO and the bi-layer LNO/LSTO junction

The light absorption experiment has been carried out first to evaluate the transmittance of these films in the visible and UV wavelength. Fig. 6.18 illustrates the transmission spectra of the single layers of LSTO and LNO, and the bi-layer LNO/LSTO junction. LSTO is highly transparent (up to 80%) in the visible to infrared wavelength range. In comparison LNO shows an inferior transmission. It has a transparency of about 60% in the infrared wavelength and a much worse transparency in the visible wavelength. The band gap energies of LSTO and LNO are 3.65eV and 3.57eV respectively. The bandgap energy is obtained by a plot of the spectral dependence of absorption coefficient $\alpha(\lambda)$ (Fig. 6.19). The Tauc relation is applied with:



$\alpha(\lambda)h\nu = \text{constant} \times (h\nu - E_{\text{gap}})^{1/r}$ and $\alpha(\lambda) = \frac{\ln(1/T)}{d}$, where $r = 2$ for direct allowed transition, T is the transmittance and d is the film thickness. The optical direct band gap energy is deduced from the extrapolation of the straight line to $(\alpha h\nu)^2 = 0$. [Tauc et. al. 1972]

For both films, absorption occurs in the UV region. Thus a junction form by these two materials can be used as UV detectors. Consequence we have studied further on different aspects of the photo-response of these films and junctions.

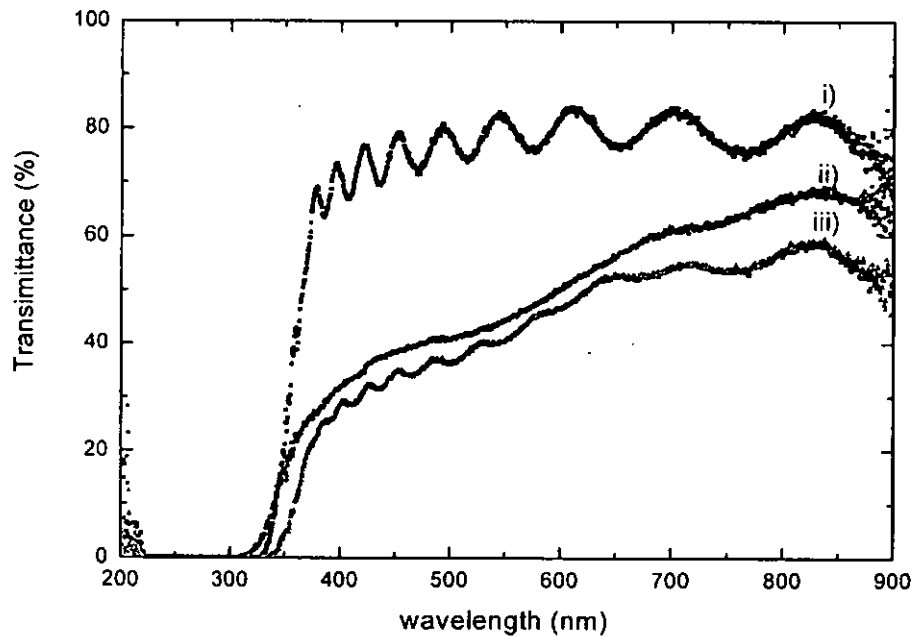


Fig. 6.18 Transmission spectra of i) LSTO, ii) LNO and iii) bi-layer LNO/LSTO

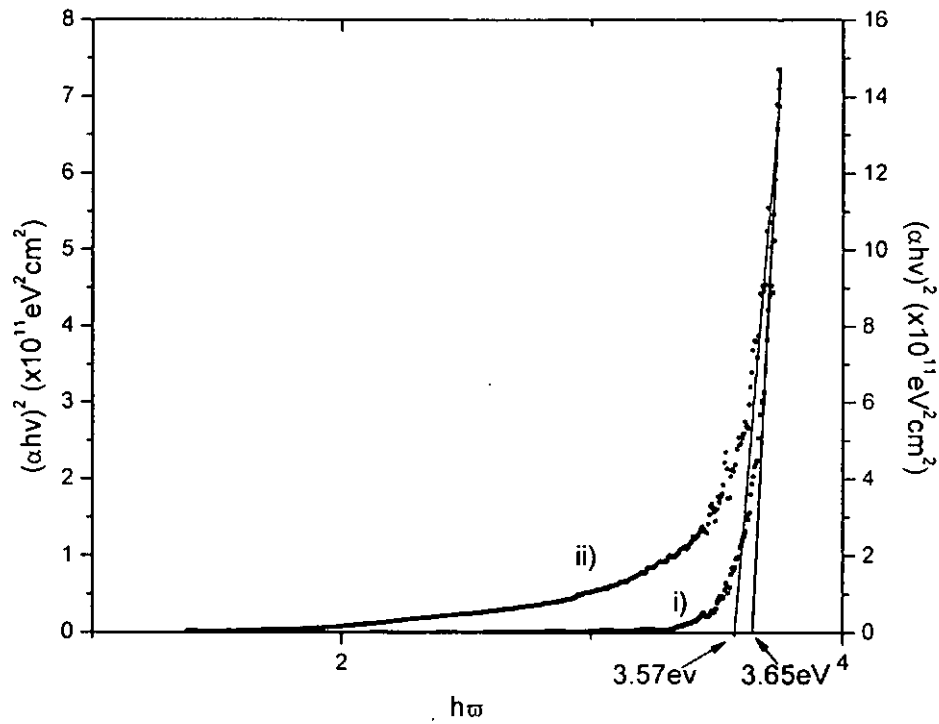


Fig. 6.19 Plot of $(\alpha h\nu)^2$ vs. $h\nu$ for the i) LSTO, and ii) LNO films. The direct optical band gap energy is deduced from the extrapolation of the straight line to $(\alpha h\nu)^2=0$

6.4.2 Photocurrent in single layer LSTO film

The change of resistivity in single layer LSTO under UV exposure was investigated. The LSTO film was grown on (100) LAO substrate. Two rectangular shaped platinum pats were coated on to the film with a separation of 3mm. The LSTO film was illuminated with a Xenon light source, which covers a wavelength range from 250nm to 480nm. Wavelength selection was achieved via transmission through a low dispersion spectrometer. Resistivity of the film dropped upon exposure to the light source. From Fig. 6.20, it is seen that the photo-response of the film gradually increases with the decreased



wavelength. A peak of ~6% change is recorded at $\lambda = 350\text{nm}$, the vicinity of the absorption edge of the film. This is expected that the highest absorption always occurs at around the absorption edge. Data at λ below 300 nm are erroneous due to the normalization of very low light intensity from the source at the wavelength range. Fig. 6.21 presents the time dependence response of the LSTO film when exposed to a continuous wave UV sources under a biased voltage. An obvious increase of current with the exposure of UV source under a short time is revealed. It also provides the information that the LSTO is very sensitive to the UV light exposure. After the removal of UV light, the current exponentially decay with time. At the present stage we have not attempt to quantity the temporal response of the LSTO films. Such an analysis can be done in the future using pulsed laser to obtain the necessary temporal resolution. Similar experiments as described above were carried out on LNO as well. No measurable photo-current, however, was observed.

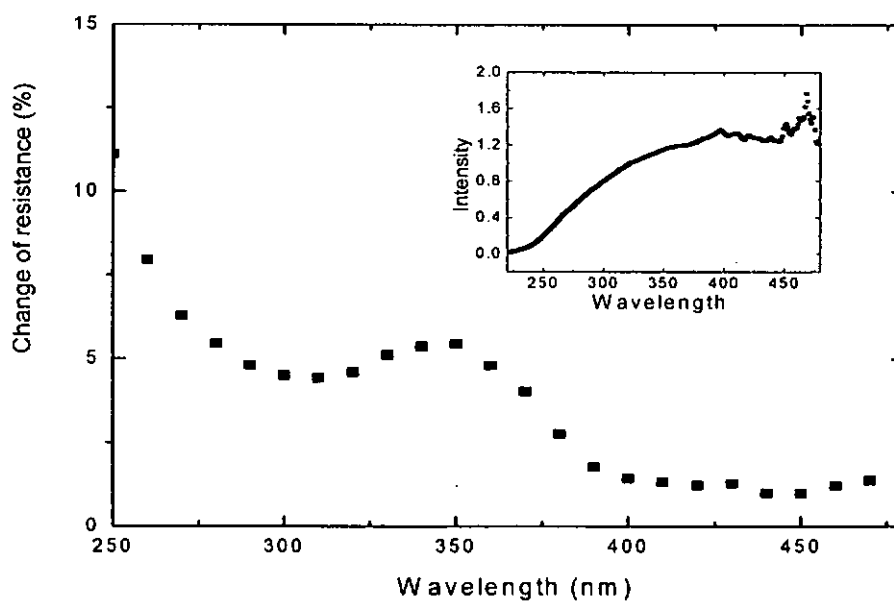


Fig. 6.20 Spectral dependence of the photo-response (resistivity change) on LSTO (The rise at wavelength below 300nm is due to errors from normalization of low light intensity at that spectral region). Inset is the light spectrum

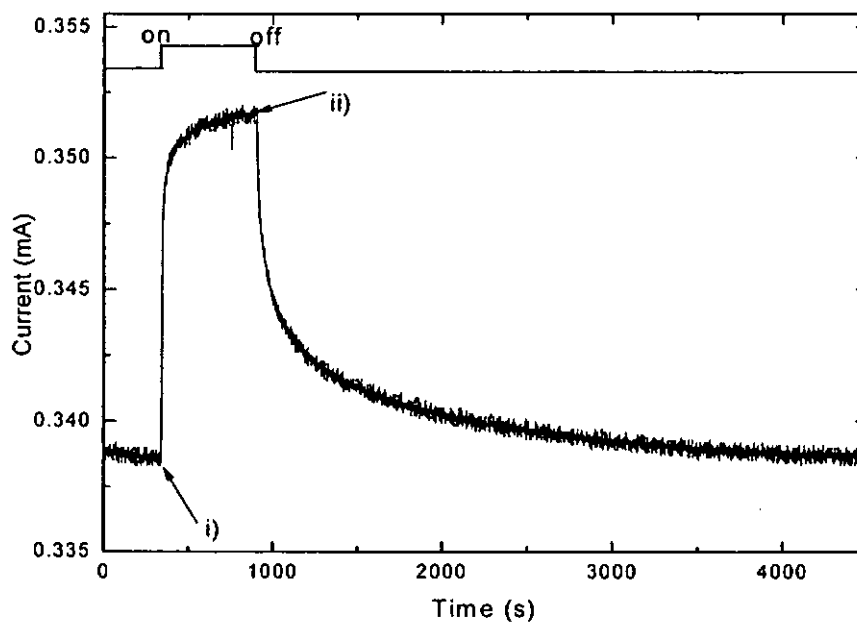


Fig. 6.21 Time dependences of 290nm wavelength UV exposure on single layer LSTO, i) under UV irradiation and ii) with UV source removal



6.4.3 UV photo-response on LSTO/LNO/LAO junction

6.4.3.1 Variation of I-V characteristics under the UV light illumination

The inset of Fig. 6.22 shows the schematic diagram of the LSTO/LNO/LAO junction under light ($\lambda = 290nm$) exposure. For this setup, the UV light passes through the LSTO layer (partially blocked by Pt top electrode) and then fall into the depletion layer. Evidently change is observed in the I-V characteristic when the junction is illuminated by the UV light. A larger leakage current is induced with the exposure of UV. There is less change on the forward biased region. The increase in leakage current is the result of photo-induction. The change in the forward biased condition is relatively small. It is understood that the photo-induced current is dwarf by the high original forward biased current.

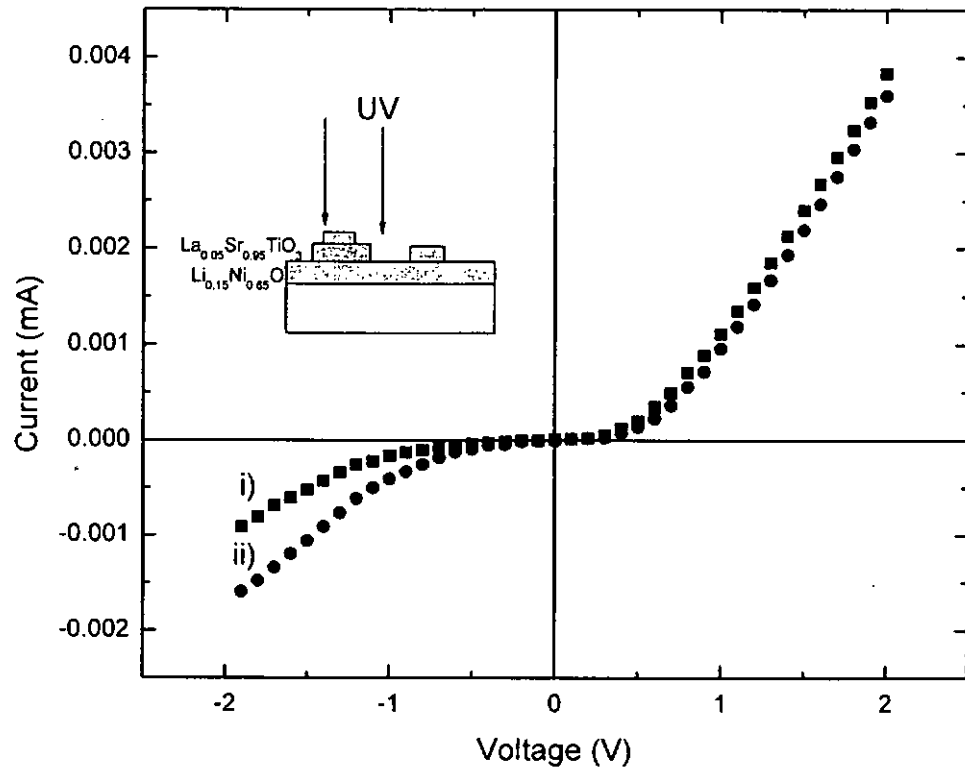


Fig. 6.22 Influences of UV exposure on the LSTO/LNO/LAO junctions; i) without the UV exposure and ii) with 290nm UV exposure.

6.4.3.2 Real time response of the junction under pulsed laser illumination

So far the photocurrent induction has been discussed. For a photo-detector, a fast response detector is appreciated. It is therefore important to examine the temporal response of this junction. For this purpose, the junction was illuminated with a pulsed laser of 248nm wavelength and pulse width of 25ns. Fig. 6.23 shows the time response of the junction under the pulsed laser irradiation with +0.5V bias and 1.1M Ω load. The rising time of the profile is

$\sim 30\mu\text{s}$, suggesting a circuit stray capacitance of $\sim 10^{-12}\text{F}$. The profile decays back to the original value in 3ms. The decay portion of the temporal response fits with an exponential curve $V \propto \exp(-t/0.12\text{ms})$, i.e. a decay lifetime of 0.12ms. It is noted that the lifetime of the extra carriers is mainly determined by the imperfection of the material. The obtained lifetime is relatively large, comparable to that in Ge single crystal [Sun et. al., 2004]. It is believed that the signal become larger when the experiment is carried out at a reversed biased voltage. At present we do not know the origin of this long decay process. Many more detailed investigations are needed to unravel the unknown mechanism

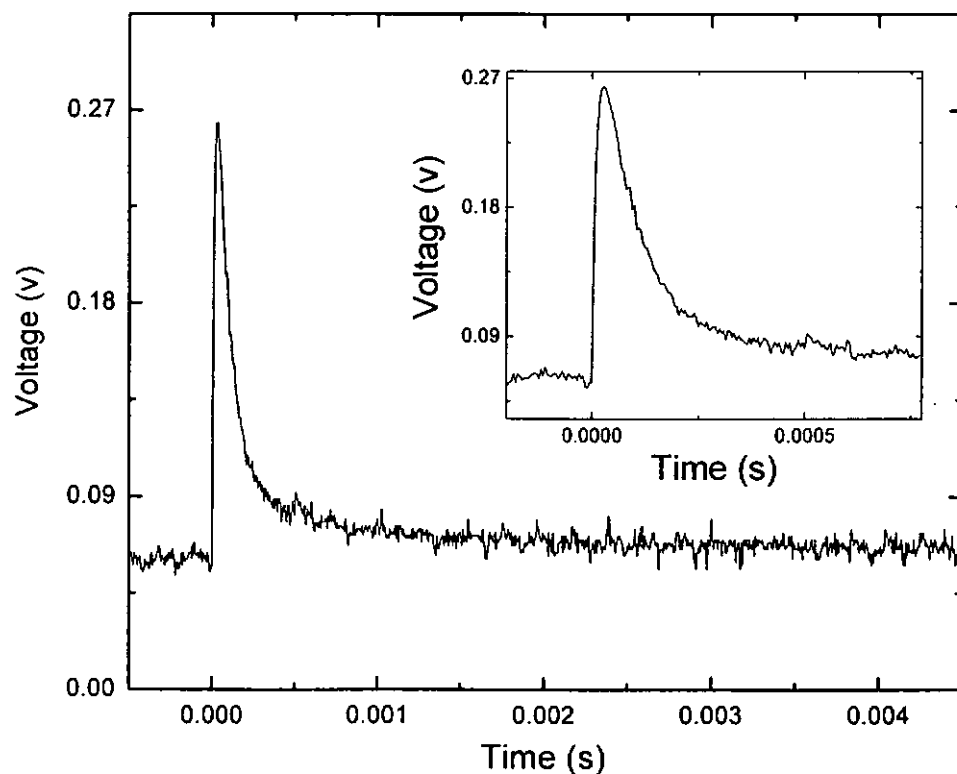


Fig. 6.23 Temporal response of the photo-induced current by a 248nm pulsed laser with the rectangle laser width of 25ns

We have shown a strong photo-induced current occurs under UV exposure. A question has been raised on whether the junction possesses photovoltaic effect. We have measured the photovoltage (open circuit voltage) of the junction by the pulsed laser irradiation. Fig. 6.24 shows the photovoltage variation with time. It shows a large voltage pulse immediately after the illumination. The pulse rise time is also around $3\mu\text{s}$. After the peak, the voltage drop off exponentially as that in Fig. 6.23, but overshoot into negative voltages. Once again, we have not investigated the phenomena further. Nevertheless, we have demonstrated that these all oxide p-n junction can be a very good photo-detector.

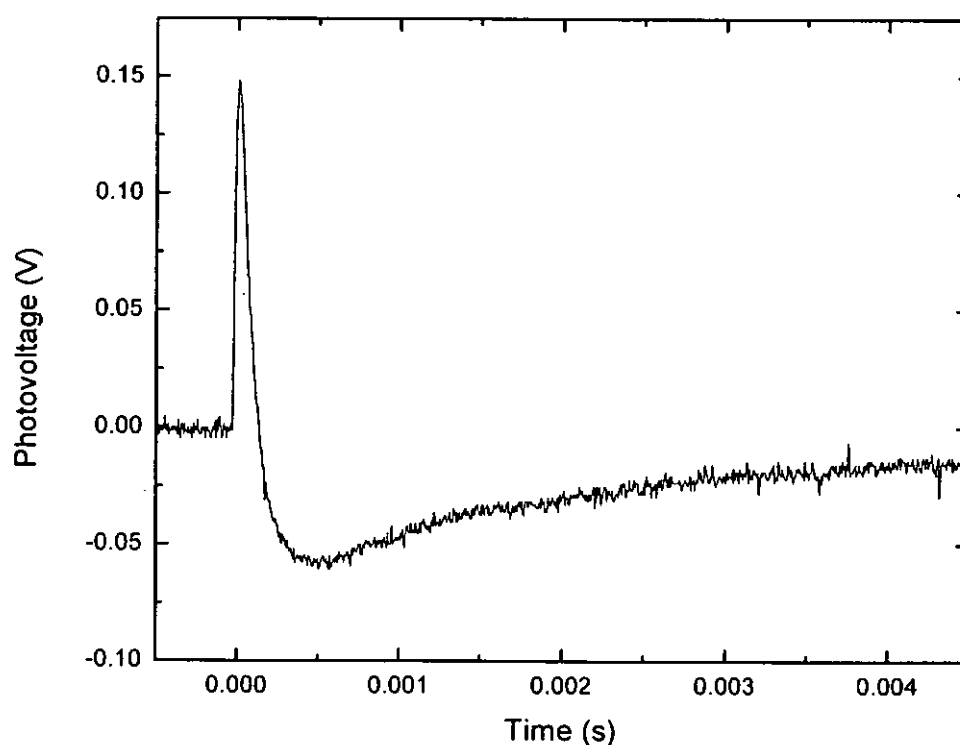


Fig. 6.24 Variation of photovoltage with time after the pulsed laser illumination



6.4.3.3 Spectral dependence on the photovoltage generation

The occurrence of photovoltage is confirmed under the UV exposure, it is interested to study the spectral dependence of the photovoltage generation. A continuous wave Xenon arc lamp emitting radiation of wavelengths from 250nm to 480nm was used. Wavelength selection was achieved by letting the Xenon lamp radiation to pass through a scanning spectrometer. The spectral spread of the radiation irradiated on the sample was estimated to be ~ 1 nm. Fig. 6.25 displays the spectral response of photovoltage. The induced voltage is the indication of photovoltaic effect occurs in the whole wavelength range from 250nm to 480nm. Values at below 300nm are dubious due to correction from small intensity irradiation. The highest photovoltage of 8mV is obtained at $\lambda = 340\text{nm}$ with irradiated power $P = 5 \mu\text{W}$. This wavelength is close to the transition band gap of LSTO and LNO (~ 3.65 and ~ 3.57 eV). From the inset, the temporal profile of the photovoltage under $\lambda = 350\text{nm}$ illumination is shown. Photovoltage abruptly increases just after the UV illumination and it also drops immediately just after the removal of the laser source. It is worthy to note that the signal-to-noise ratio is very high, the large response totally causes by the UV illumination. The actual irradiation power falls onto the p-n junction is difficult to estimate. The light spot size is much greater than the p-n junction sample size. Much of the radiation is blocked by the top Pt electrode. However we do can conclude at this point that this junction could be used for UV (320nm to 380nm) detection and its peak spectral response is at $\lambda = 340\text{nm}$.

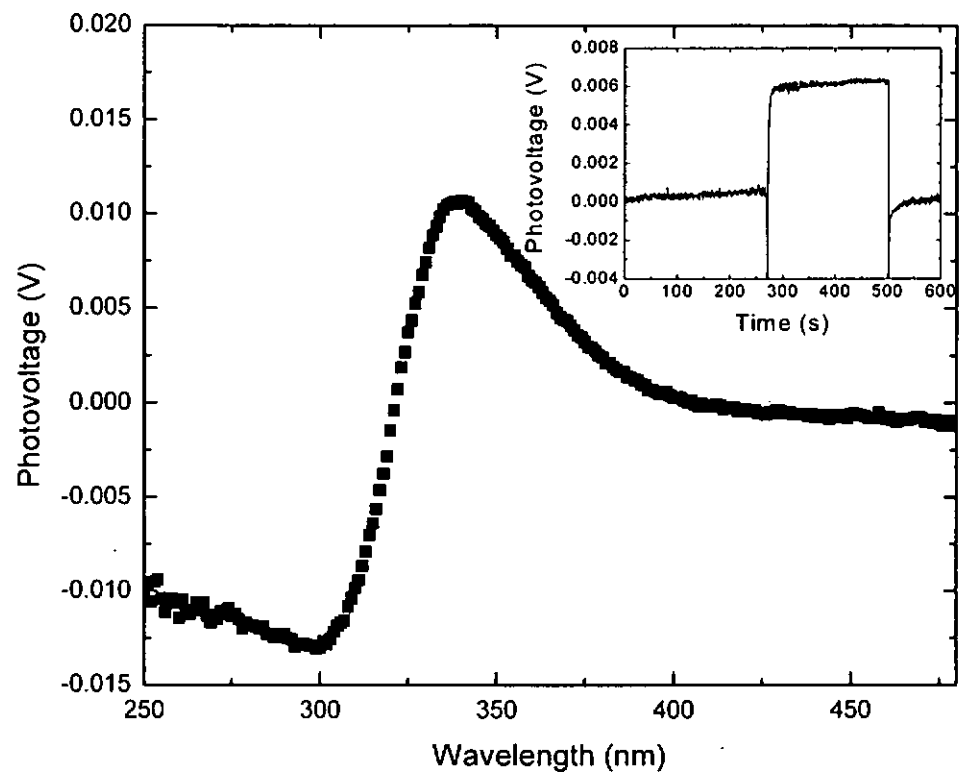


Fig. 6.25 Spectral response of the junction under the Xenon light illumination
Inset shows the temporal response of the junction under 350nm light illumination

6.4.4 UV response of the LNO/LSTO/LAO junction

6.4.4.1 Spectral dependence of the photovoltage generation

In addition to the LSTO/LNO/LAO junction, the photo-response of the LNO/LSTO/LAO junction was also investigated at room temperature. For this junction the UV was irradiated through the LAO substrate. Light passes through the LSTO layer and reaches the depletion region as illustrate in Fig. 6.26. The photovoltaic effect on the junction was examined with the Xenon



light source at a radiation power of $5\ \mu\text{W}$. The potential difference between the n-layer and p-layer was measured under different spectral irradiation. A drastic increase of the photovoltage is observed. As extra carriers are generated in the depletion layer under UV irradiation, they are drawn by the built-in electric field; positive charge carriers moved to the p-region while negative charge carriers drifted to the n-region. These charges accumulated in these two regions, therefore creating a photovoltage. Induction of photovoltage occurs over the whole wavelength range from 250nm to 480nm. As before, the values at wavelength less than 300nm are dubious. Photovoltage peaks at 340nm with a value of 377 mV. The largest photovoltage at around 340nm is due to the highest absorption around the band edges of LNO and LSTO (~ 3.65 and ~ 3.57 eV), respectively. The photo-response to light illumination is illustrated by the responsivity (defined as V_{oc}/power). The responsivity of this junction for wavelength of 340nm at an incident power of $5\ \mu\text{W}$ is $7.54 \times 10^4\ \text{V/W}$. This figure is obtained without correction for the absorption by the LAO substrate. Sun and co-worker reported a $\text{La}_{0.7}\text{Ce}_{0.3}\text{MnO}_{3-\delta}/\text{SrTiO}_3\text{-Nb}$ junction [Sun et. al. 2004], which exhibits a responsivity of $\sim 8000\ \text{V/W}$ when illuminated by $6.5\ \mu\text{W}$ of $\lambda = 460\text{nm}$ radiation. Our junction possesses a larger responsivity than Sun's junction and it peaks in the UV. It is therefore a good UV detector with reasonable spectral selectivity.

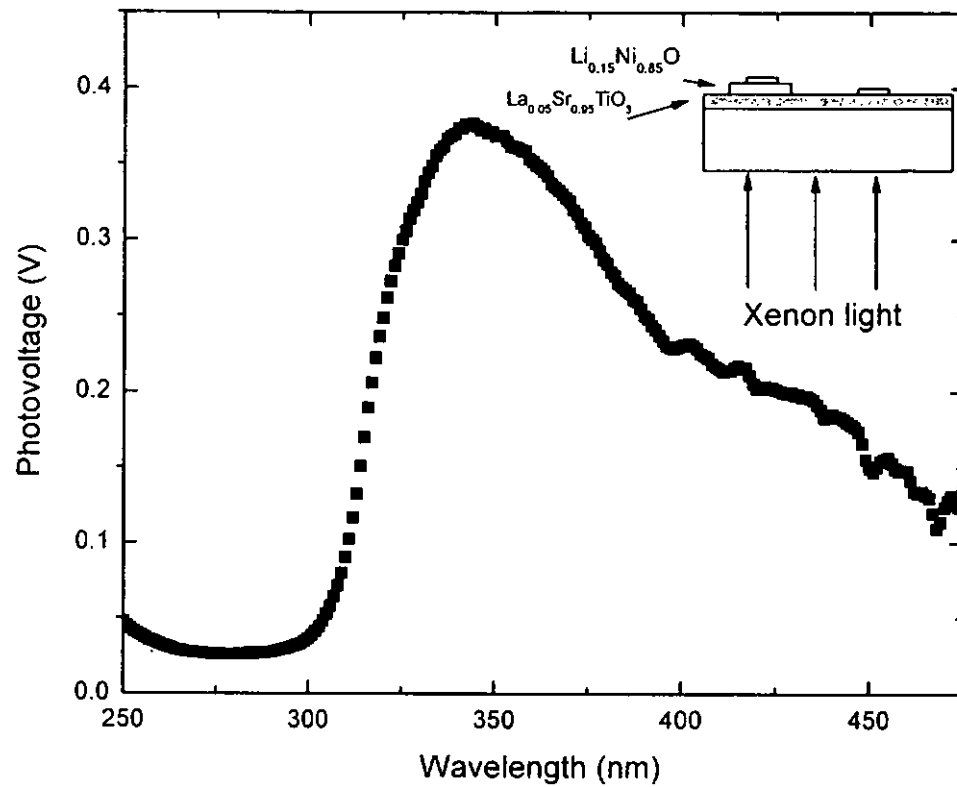


Fig. 6.26 Spectral dependence on the photovoltage under $5 \mu\text{W}$ illumination in the LNO/LSTO/LAO junction

Apart from the Xenon light source, a UV LED ($\lambda = 397\text{nm}$) was employed for the photo-response measurement at different irradiation power. The output power of the LED light was controlled by the adjustable bias voltage. Fig. 6.27 suggests the increase of photovoltage with the incident power. Photovoltage increases from 39 mV to 240 mV under the illumination power of $0.35\text{ }\mu\text{W}$ and $5.38\text{ }\mu\text{W}$ respectively. The photovoltage-power relation shows signs of saturation of the photovoltage at incident power $> 3\text{ }\mu\text{W}$. The responsivity of our junction shows a maximum of $12 \times 10^4\text{ V/W}$ under the illumination power of $0.79\text{ }\mu\text{W}$. Again, this figure has not been corrected for the absorption of LAO. The actual junction responsivity should be much better than quoted here.

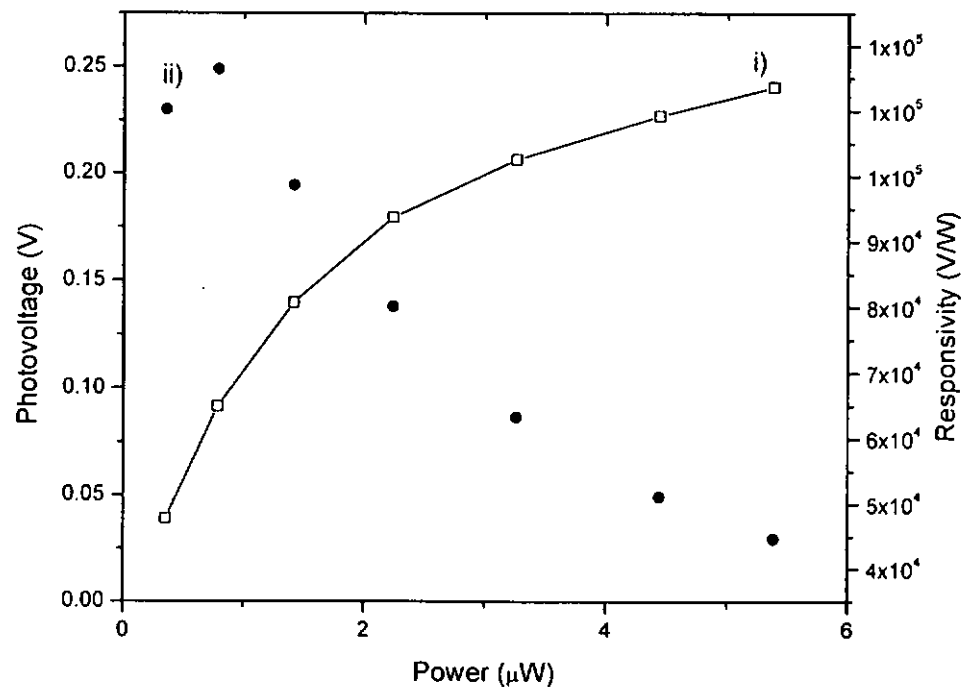


Fig. 6.27 Plots of i) photovoltage as a function of light power ($\lambda = 397\text{nm}$) and ii) junction responsivity against the function of light power measured under room temperature (295K)



In conclusion, all-oxide p-n junctions have been fabricated using of n-LSTO and p-LNO. Heteroepitaxial growth of LNO/LSTO on LAO single crystal substrate was achieved by PLD method. Two p-n junctions of different configurations have been produced. They exhibit good rectifying effect under room temperature operation. In both cases, the turn-on voltages are 0.3V. The LNO/LSTO/LAO junction maintains a good rectifying property at temperature up to 493K. Unfortunately both junctions show a small reverse breakdown voltage and a large leakage current. It is demonstrated a thin STO layer ($t > 160\text{nm}$) inserted between the LNO and LSTO layers helps to reduce the tunneling current at the reverse biased condition. With the increase of the STO layer thickness, the breakdown hold off of the junction improves but the turn-on voltage increases.

Photo-responses of both LSTO/LNO/LAO and LNO/LSTO/LAO junctions have been examined. High photovoltage are obtained by UV irradiation. An efficient all-oxide p-n junction for selective UV detection has been demonstrated.



Chapter 7

Conclusion and future work

Our $\text{La}_{1-x}\text{Sr}_x\text{MnO}_3/\text{SrTiO}_3/\text{La}_{1-y}\text{Sr}_y\text{TiO}_3$, $\text{La}_{0.7}\text{Sr}_{0.3}\text{MnO}_3/\text{Nb-1wt\% doped SrTiO}_3$ and $\text{Li}_{0.15}\text{Ni}_{0.85}\text{O}/\text{La}_{0.05}\text{Sr}_{0.95}\text{TiO}_3$ junctions show a clear rectifying property under room temperature operation. Their heteroepitaxial relationship is confirmed by the XRD measurement.

We have fabricated the $\text{La}_{1-x}\text{Sr}_x\text{MnO}_3/\text{SrTiO}_3/\text{La}_{1-y}\text{Sr}_y\text{TiO}_3$ junctions with different composition of LSMO and LSTO. It is intended to produce a p-n junction with good rectifying property. $\text{La}_{1-y}\text{Sr}_y\text{TiO}_3$ is n-type conducting oxide with a positive temperature coefficient under a temperature range from 300K to 500K. $\text{La}_{1-x}\text{Sr}_x\text{MnO}_3$, on the other hand, is p-type conducting oxide with a negative temperature coefficient under room temperature. The resistivity of $\text{La}_{0.85}\text{Sr}_{0.15}\text{MnO}_3$ is six orders of magnitude larger than that of $\text{La}_{0.7}\text{Sr}_{0.3}\text{MnO}_3$. The low resistivity of $\text{La}_{0.7}\text{Sr}_{0.3}\text{MnO}_3$ leads to the larger diffusion current in the $\text{La}_{0.7}\text{Sr}_{0.3}\text{MnO}_3/\text{SrTiO}_3/\text{La}_{0.05}\text{Sr}_{0.95}\text{TiO}_3$ junctions. We fabricated $\text{La}_{0.7}\text{Sr}_{0.3}\text{MnO}_3/\text{SrTiO}_3/\text{La}_{1-y}\text{Sr}_y\text{TiO}_3$ junctions with three different composition of LSTO: $\text{La}_{0.05}\text{Sr}_{0.95}\text{TiO}_3$, $\text{La}_{0.1}\text{Sr}_{0.9}\text{TiO}_3$ and $\text{La}_{0.15}\text{Sr}_{0.85}\text{TiO}_3$. The increase of lanthanum doping promotes the electrical conduction. At room temperature, we obtained the lowest resistivity of $6.5\text{m}\Omega - \text{cm}$ from the $\text{La}_{0.15}\text{Sr}_{0.85}\text{TiO}_3$ film. $\text{La}_{0.7}\text{Sr}_{0.3}\text{MnO}_3/\text{SrTiO}_3/\text{La}_{0.05}\text{Sr}_{0.95}\text{TiO}_3$ and $\text{La}_{0.85}\text{Sr}_{0.15}\text{MnO}_3/\text{SrTiO}_3/\text{La}_{0.05}\text{Sr}_{0.95}\text{TiO}_3$ junctions showed similar turn-on voltage of $\sim 1\text{V}$. High temperature operation is obtained in these $\text{La}_{1-x}\text{Sr}_x\text{MnO}_3/\text{SrTiO}_3/\text{La}_{1-y}\text{Sr}_y\text{TiO}_3$



junctions. Although the turn-on voltage decreases and the leakage current increases with temperature, the junctions retain a fair rectifying profile at temperature up to $\sim 500\text{K}$. The slope of the I-V curve at forward biased condition changes with temperature. It is the result of the combined effect of space-charge limitation current and large series resistance contribution from the bottom oxide layer. General speaking, $\text{La}_{0.7}\text{Sr}_{0.3}\text{MnO}_3/\text{SrTiO}_3/\text{La}_{0.15}\text{Sr}_{0.85}\text{TiO}_3$ exhibits the highest diffusion current among the two junctions ($\text{La}_{0.7}\text{Sr}_{0.3}\text{MnO}_3/\text{SrTiO}_3/\text{La}_{0.05}\text{Sr}_{0.95}\text{TiO}_3$ and $\text{La}_{0.7}\text{Sr}_{0.3}\text{MnO}_3/\text{SrTiO}_3/\text{La}_{0.05}\text{Sr}_{0.95}\text{TiO}_3$ junctions).

The current rectifying property of $\text{La}_{0.7}\text{Sr}_{0.3}\text{MnO}_3/\text{Nb-SrTiO}_3$ was shown in Chapter 5. $\text{La}_{0.7}\text{Sr}_{0.3}\text{MnO}_3$, which has been fabricated under a deposition pressure of 100 mTorr and substrate temperature of 650°C , has a Curie temperature of 290K. The junction possesses a turn-on voltage of 0.2V and an ideality factor of 1.4. Unfortunately the junction cannot retain the current rectifying characteristic at temperatures above 380K. At above 380K, the minority charge carriers acquire adequate energy for traversing the depletion layer. An efficient way to suppress the leakage current is by insertion of a thin SrTiO_3 layer of $\sim 160\text{nm}$ thick in between the $\text{La}_{0.7}\text{Sr}_{0.3}\text{MnO}_3$ and Nb-SrTiO_3 . The insertion of the SrTiO_3 layer has raised the turn-on voltage of the junction to 0.9V. In addition the space-charge-limited current effect is observed in the $\text{La}_{0.7}\text{Sr}_{0.3}\text{MnO}_3/\text{SrTiO}_3/\text{Nb-SrTiO}_3$ junction but not in the $\text{La}_{0.7}\text{Sr}_{0.3}\text{MnO}_3/\text{Nb-SrTiO}_3$ junction. Consequently the forward biased current is seen to increase exponentially with temperature. Furthermore we have also shown that this p-i-n junction can retain good rectifying property at 500K.



We have fabricated transparent-oxide $p\text{-Li}_{0.15}\text{Ni}_{0.85}\text{O}/n\text{-La}_{0.05}\text{Sr}_{0.95}\text{TiO}_3$ junctions. They exhibit clear current rectifying characteristics and a sharp turn-on voltage of 0.6V. It is observed that the $\text{Li}_{0.15}\text{Ni}_{0.85}\text{O}/\text{La}_{0.05}\text{Sr}_{0.95}\text{TiO}_3$ junctions retain a I-V curve asymmetry at temperatures up to 493K. We have fabricated and appraised the $\text{La}_{0.05}\text{Sr}_{0.95}\text{TiO}_3/\text{Li}_{0.15}\text{Ni}_{0.85}\text{O}$ junction grown with a reversed order of depositing the $\text{La}_{0.05}\text{Sr}_{0.95}\text{TiO}_3$ and $\text{Li}_{0.15}\text{Ni}_{0.85}\text{O}$ layers. It is seen that the high conducting $\text{La}_{0.05}\text{Sr}_{0.95}\text{TiO}_3$ as the bottom layer in the p-n junction promotes a low series resistance. The low series resistance helps to reveal the junction rectifying property more clearly. Generally speaking, the $\text{Li}_{0.15}\text{Ni}_{0.85}\text{O}/\text{La}_{0.05}\text{Sr}_{0.95}\text{TiO}_3$ junction is highly recommended. In addition to the high temperature operation, we are also interested in the development of an Ultra-Violet radiation detector. Both the $\text{Li}_{0.15}\text{Ni}_{0.85}\text{O}/\text{La}_{0.05}\text{Sr}_{0.95}\text{TiO}_3$ and $\text{La}_{0.05}\text{Sr}_{0.95}\text{TiO}_3/\text{Li}_{0.15}\text{Ni}_{0.85}\text{O}$ junctions exhibit good UV photovoltaic effects. They both exhibit the largest photovoltage when illuminated with radiation of $\lambda = 340\text{nm}$. It is noted that $\lambda = 340\text{nm}$ is very close to the absorption edges of $\text{Li}_{0.15}\text{Ni}_{0.85}\text{O}$ ($\lambda = 348\text{nm}$) and $\text{La}_{0.05}\text{Sr}_{0.95}\text{TiO}_3$ ($\lambda = 340\text{nm}$). In the case of the $\text{Li}_{0.15}\text{Ni}_{0.85}\text{O}/\text{La}_{0.05}\text{Sr}_{0.95}\text{TiO}_3$ junction, we have registered the highest photovoltage of 377 mV and responsivity of $7.54 \times 10^4 \text{ V/W}$ under the illumination of $\lambda = 340\text{nm}$ at $P = 5\mu\text{W}$.

In conclusion, high temperature operations in all our p-n/p-i-n oxide junctions have been demonstrated. We have also revealed the possibility of UV detection using the $\text{Li}_{0.15}\text{Ni}_{0.85}\text{O}$ and $\text{La}_{0.05}\text{Sr}_{0.95}\text{TiO}_3$ bi-layer junction. The sudden rise of the photo-response of this junction at illumination wavelength $\lambda = 340\text{nm}$ suggests a UV detector with good wavelength selecting.



In comparison to the conventional semiconductor p-n junction, our oxide junction could operate under temperature as high as the large bandgap semiconductor junction. Although the maximum operation temperature is not examined yet, it is believed that it must be higher than 500K. As our oxide junction could retain a good rectifying property under temperature of 500K, further increase in operation temperature is still possible. The photovoltaic response of our $\text{Li}_{0.15}\text{Ni}_{0.85}\text{O}/\text{La}_{0.05}\text{Sr}_{0.95}\text{TiO}_3$ junction is very large. However our junction photoresponse measurement is still in the primary investigation, it is better to carry out more investigation on photoresponse properties in the future work. Apart from the high temperature dependence and the photoresponse, our oxide junction is potentially used in multifunctional purpose. As it is claimed that oxides always have some special and diverse properties, to combine with these properties the junction performance might get over the conventional semiconductor junction.

The success fabrication of all-oxide p-n junction is the first step of conducting/semiconducting oxide utilization in the electronic world. Although an intermediately high temperature operation of all-oxide p-n junction is confirmed, the ultimate performance at very high temperature is still uncertain. In the future, we should target to examine the maximum operation temperature in oxide junctions. On the other hand, high current density p-n junction may be achieved by use of the thermally and chemically stable oxides. So it is worthy to look into developing high current density all-oxide p-n junction. Apart from the p-n diode, tri-layer transistor is another major semiconductor component in the electronic technology. Fabrication of all-oxide transistor is therefore another future interest.



By blending the multitudinous functionalities of oxide, such as ferroic properties, thermoelectricity, superconductivity, magnetism and photoelectricity, etc, together with diode junction or transistor provides an immense opportunity for development of various exotic sensors and spintronic devices. We believe the present research can serve as a good foundation and a starting foothold for many future R&D in this new avenue.



References

- 1) D. Adler, and J. Feinleib, "Electrical and optical properties of narrow-band materials", *Phys. Rev. B.*, **2**, 3112 (1970)
- 2) A. J. Bosman, and C. Crevecoeur, "Mechanism of the electrical conduction in Li-Doped NiO", *Phys. Rev.*, **144**, 763 (1966)
- 3) M. Cardona, "Optical Properties and band structure of SrTiO₃ and BaTiO₃", *Phys Rev.*, **140**, A651 (1963)
- 4) J. T. Cheung, and T. Magee, "Recent progress on LADA growth of HgCdTe and CdTe epitaxial layers", *J. Vac. Sci. A1*, 1604 (1983)
- 5) Y. S. Choi, J. Y. Lee, S. Im, and S. J. Lee, "Photoresponse characteristics of n-ZnO/p-Si heterojunction photodiodes", *J. Vac. Sci. Technol. B*, **20**, 2384 (2002)
- 6) P. A Cox, "Transition metal oxides: an introduction to their electronic structure and properties", Oxford Clarendon Press New York Oxford University Press, 1992
- 7) D. B. Chrisey, and Hubler, G. K. "Pulsed laser deposition of thin films", John Wiley & Sons, 1994
- 8) J. Dho, N. H. Hur, I. S. Kim, and Y. K. Park, "Oxygen pressure and thickness dependent lattice strain in La_{0.7}Sr_{0.3}MnO₃ films", *J. Appl. Phys.*, **94**, 7670 (2003)
- 9) J. van Elp, H. Eskes, P. Kuiper, and G. A. Sawatzky, "Electronic structure of Li-doped NiO", *Phys. Rev. B*, **45**, 1612 (1992)
- 10) H. Hiramatsu, K. Ueda, H. Ohta, M. Hirano, T. Kamiya, and H. Hosono, "Degenerated p-type conductivity in wide-gap LaCuOS_{1-x}Sex (x=0-1)



- epitaxial films", *Appl. Phys. Lett.*, **82**, 1048 (2003)
- 11) H. Hosono, H. Ohta, K. Hayashi, M. Orita, and M. Hirano, "Near-UV emitting diodes based on a transparent p-n junction composed of heteroepitaxially grown p-SrCu₂O₂ and n-ZnO", *J. Cryst. Growth*, 237-239, 496 (2002)
- 12) F. X. Hu, J. Gao, J. R. Sun and B. G. Shen, " Good rectifying characteristic in p-n junctions composed of La_{0.67}Ca_{0.33}MnO_{3-δ}/Nb-0.7wt%-doped SrTiO₃", *App. Phys. Lett.*, **83**, 1869 (2003)
- 13) M. Iwabuchi, and T. Kobayashi, "Growth and characterization of epitaxial SrTiO₃ thin films with prominent polarizability", *J. Appl. Phys.*, **75**, 5295 (1994)
- 14) H. Kim, J. S. Horwitz, G. P. Kushto, S. B. Qadri, Z. H. Kafafi, and D. B. Chrisey, "Transparent conducting Zr-doped In₂O₃ thin films for organic light-emitting diodes", *Appl. Phys. Lett.*, **78**, 1050 (2001)
- 15) H. Kim, J. S. Horwitz, W. H. Kim, S. B. Qadri, and Z. H. Kafafi, "Anode material based on Zr-doped ZnO thin films for organic light-emitting diodes", *Appl. Phys. Lett.*, **83**, 3809 (2003)
- 16) K. Kinoshita, H. Ishibashi, T. Kobayashi, 54th Fall Meeting of the Japan Society of Applied Physics, Sapporo, Japan, September 27-30, Extended abstracts I, 1993
- 17) T. Kudo, M. Tachiki, T. Kashiwai, and T. Kobayashi, "Band diagram of metal-insulator-magnetic semiconductor (La_{0.85}Sr_{0.15}MnO₃) structure at room temperature", *Jpn. J. Appl. Phys.*, **37**, L999 (1998)
- 18) A. Kudo, H. Yanagi, K. Ueda, H. Hosono, H. Kawazoe, and Y. Yano, "Fabrication of transparent p-n heterojunction thin film diodes based



- entirely on oxide semiconductors”, *Appl. Phys. Lett.*, **75**, 2851 (1999)
- 19) W. Y. Lee, D. Mauri, and C. Hwang, “High-current-density $\text{ITO}_x/\text{NiO}_x$ thin-film diodes”, *Appl. Phys. Lett.*, **72**, 1584 (1998)
- 20) B. T. Liu, K. Maki, Y. So, V. Nagarajan, R. Ramesh, J. Lettieri, J. H. Haeni, D. G. Schlom, W. Tian, X. Q. Pan, F. J. Walker, and R. A. McKee, “Epitaxial La-doped SrTiO_3 on silicon: A conductive template for epitaxial ferroelectrics on silicon”, *Appl. Phys. Lett.*, **80**, 4801 (2002)
- 21) X. B. Lu, Z. G. Liu, Y. P. Wang, Y. Yang, X. P. Wang, H. W. Zhou, B. Y. Nguyen, “Structure and dielectric properties of amorphous LaAlO_3 and LaAlO_xN_y films as alternative gate dielectric materials”, *J. Appl. Phys.*, **94**, 1229 (2003)
- 22) C. Mitra, P. Raychaudhuri, G. Kobernik, K. Dorr, K. H. Muller, L. Schultz, and R. Pinto, “p-n diode with hole- and electron-doped lanthanum manganites”, *Appl. Phys. Lett.*, **79**, 2408 (2001)
- 23) T. Nakasaka, K. Urago, M. Sugiura, and T. Kobayashi, “Hysteretic current-voltage characteristics of all-oxide $(\text{LaSr})\text{MnO}_3/\text{BaTiO}_3/(\text{LaSr})\text{TiO}_3$ p-i-n diode”, *Jpn. J. Appl. Phys.*, **40**, L518 (2001)
- 24) S. Ohmi, M. Takeda, H. Ishiwara, and H. Iwai, “Electrical characteristics for Lu_2O_3 thin films fabricated by E-beam deposition method”, *J. Elect. Soc.*, **151**, G279 (2004)
- 25) H. Ohta, K. Kawamura, M. Orita, M. Hirano, No. Sarukura, and H. Hosono, “Current injection emission from the transparent p-n junction composed of p- SrCu_2O_2 /n- ZnO ”, *Appl. Phys. Lett.*, **77**, 475 (2000)
- 26) H. Ohta, M. Hirano, K. Nakahara, H. Maruta, T. Tanabe, M. Kamiya, T. Kamiya, and H. Hosono, “Fabrication and photoresponse of a



- pn-heterojunction diode composed of transparent oxide semiconductors, p-NiO and n-ZnO", *Appl. Phys. Lett.*, **83**, 1029 (2003)
- 27) R. J. Powell, and W. E. Spicer, "Optical properties of NiO and CoO", *Phys. Rev. B*, **2**, 2182 (1970)
- 28) G. A. Sawatzky, and J. W. Allen, "Magnitude and origin of the band gap in NiO", *Phys. Rev. Lett.*, **53**, 2339 (1984)
- 29) A. Schmehl, F. Lichtenberg, H. Bielefeldt, J. Mannhart, and D. G. Schlom, "Transport properties of LaTiO_{3+x} films and heterostructures", *Appl. Phys. Lett.*, **82**, 3077 (2003)
- 30) P. Sharma, and K. Sreenivas, "Highly sensitive ultraviolet detector based on $\text{ZnO}/\text{LiNbO}_3$ hybrid surface acoustic wave filter", *Appl. Phys. Lett.*, **83**, 3617 (2003)
- 31) W. Shin, N. Murayama, "Li-doped nickel oxide as a thermoelectric material", *Jpn. J. Appl. Phys.*, **38**, L1336 (1999)
- 32) J. J. Sparkes, "Semiconductor devices", Chapman & Hall, 1994
- 33) M. Sugiura, K. Uragou, M. Noda, M. Takeshi, and T. Kobayashi, "First demonstration of rectifying property of p-i-n heterojunctions fabricated by tri-layered semiconducting oxides", *Jpn. J. Appl. Phys.* **38**, 2675 (1999)
- 34) M. Sugiura, K. Uragou, M. Tachiki, and Takeshi Kobayashi, "Estimation of trap levels in SrTiO_3 epitaxial films from measurement of $(\text{LaSr})\text{MnO}_3/\text{SrTiO}_3/(\text{LaSr})\text{TiO}_3$ p-i-n diode characteristics", *Jpn. Appl. Phys.*, **90**, 187 (2001)
- 35) J. R. Sun, C. M. Xiong, B. G. Shen, P. Y. Wang, and Y. X. Weng, "Manganite-based heterojunction and its photovoltaic effects", *App. Phys. Lett.*, **84**, 2611 (2004)



- 36) J. R. Sun, C. H. Lai, and H. K. Wong, "Photovoltaic effect in $\text{La}_{0.7}\text{Ce}_{0.3}\text{MnO}_{3-\delta}/\text{SrTiO}_3\text{-Nb}$ heterojunction and its oxygen content dependence", *App. Phys. Lett.*, **85**, 37 (2004)
- 37) J. R. Sun, C. M. Xiong, T. Y. Zhao, S. Y. Zhang, Y. F. Chen, and B. G. Shen, "Effects of magnetic field on the manganite-based bilayer junction", *Appl. Phys. Lett.*, **84**, 1528 (2004)
- 38) S. Suzuki, T. Miyata, and T. Minami, "p-type semiconducting $\text{Cu}_2\text{O-CoO}$ thin films prepared by magnetron sputtering", *J. vac. Sci. Technol. A*, **21**, 1336 (2003)
- 39) S. M. Sze, "Semiconductor devices: physics and technology", New York Wiley, 1985
- 40) S. M. Sze, "Physics of semiconductor devices", New York Wiley, 1981
- 41) M. Tachiki, M. Noda, K. Yamada, and T. Kobayashi, " SrTiO_3 films epitaxially grown by eclipse pulsed laser deposition and their electrical characterization", *J. Appl. Phys.*, **83**, 5351 (1998)
- 42) M. Tachiki, T. Hosomi, and T. Kobayashi, "Room-temperature heteroepitaxial growth of NiO thin films using pulsed laser deposition", *Jpn. J. Appl. Phys.*, **39**, 1817 (2000)
- 43) H. Tanaka, J. Zhang, and T. Kawai, "Giant electric field modulation of double exchange ferromagnetism at room temperature in the perovskite manganite/ Titanate p-n junction", *Phys. Rev. Lett.*, **88**, 027204 (2002)
- 44) S. P. Tang, N. G. Utterback, and J. F. Friichtenicht, "Measurement of chemiluminescent reaction cross sections for $B + \text{N}_2\text{O} \rightarrow \text{BO}^* + \text{N}_2$ and $\text{H}_0 + \text{N}_2\text{O} \rightarrow \text{H}_0\text{O}^* + \text{N}_2$ ", *J. Chem. Phys.*, **64**, 3833 (1976)
- 45) J. C. Tauc, *Optical Properties of Solids*, North-Holland, Amsterdam, 1972



- 46) A. Tiwari, C. Jin, D. Kumar, and J. Narayan, "Rectifying electrical characteristics of $\text{La}_{0.7}\text{Sr}_{0.3}\text{MnO}_3/\text{ZnO}$ heterostructure", *Appl. Phys. Lett.*, **83**, 1773 (2003)
- 47) Y. Tokura, Y. Taguchi, Y. Okada, Y. Fujishima, T. Arima, K. Kumagai, and Y. Iye, "Filling dependence of electronic properties on the Verge of Metal-Mott-Insulator transitions in $\text{Sr}_{1-x}\text{La}_x\text{TiO}_3$ ", *Phys. Rev. Lett.*, **70**, 2126 (1993)
- 48) A. Urushibara, Y. Moritomo, T. Arima, A. Asamitsu, G. Kido, and Y. Tokura, "Insulator-metal transition and giant magnetoresistance in $\text{La}_{1-x}\text{Sr}_x\text{MnO}_3$ ", *Phys. Rev. B*, **51**, 14103 (1995)
- 49) C. F. Windisch, Jr., K. F. Ferris, and G. J. Exarhos, "Synthesis and characterization of transparent conducting oxide cobalt-nickel spinel films", *J. Vac. Sci. Technol. A*, **19**, 1647 (2001)
- 50) W. B. Wu, K. H. Wong, X. G. Li, C. L. Choy, and Y. H. Zhang, "Effect of annealing in reduced oxygen pressure on the electrical transport properties of epitaxial thin film and bulk $(\text{La}_{1-x}\text{Nd}_x)_{0.7}\text{Sr}_{0.3}\text{MnO}_3$ ", *J. Appl. Phys.*, **87**, 3006 (2000)
- 51) W. B. Wu, F. Lu, K. H. Wong, G. Pang, C. L. Choy, and Y. Zhang, "Epitaxial and highly electrical conductive $\text{La}_{0.5}\text{Sr}_{0.5}\text{TiO}_3$ films grown by pulsed laser deposition in vacuum", *J. Appl. Phys.*, **88**, 700 (2000)
- 52) W. B. Wu, K. H. Wong, C. L. Choy, and Y. H. Zhang, "In situ oxygen control and high thermal stability of epitaxial $(\text{La}_{1-x}\text{Nd}_x)_{0.7}\text{Sr}_{0.3}\text{MnO}_3$ films fabricated by pulsed laser deposition", *Thin Solid Films*, **289**, 56 (2001)
- 53) W. Yang, R. D. Vispute, S. Choopun, R. P. Sharman, T. Venkatesan, and H. Shen, "Ultraviolet photoconductive detector based on epitaxial



Mg_{0.34}Zn_{0.66}O thin films”, *Appl. Phys. Lett.*, **78**, 2787 (2001)

- 54) M. Youm, H. S. Sim, H. Jeon, S. Kim, and Y. T. Kim, “Metal oxide semiconductor field effect transistor characteristics with iridium gate electrode on atomic layer deposited ZrO₂ high-*k* dielectric”, *Jpn. J. Appl. Phys.*, **42**, 5010 (2003)
- 55) J. Zhang, H. Tanaka, and T. Kawai, “ Rectifying characteristic in all-perovskite oxide film p-n junction with room temperature ferromagnetism”, *App. Phys. Lett.*, **80**, 4378 (2002)